Modifying germanium nanowires for future devices: an in situ TEM study

Róisín Ann Kelly, B.Sc. (Hons)

Department of Chemistry

University College Cork

Ireland

Presented for the degree of Doctor of Philosophy to the National University of Ireland

Supervisor: Dr Nikolay Petkov

Co-supervisor: Prof. Justin D. Holmes

Head of Department: Prof. Martyn Pemble

Declaration

I, Róisín Ann Kelly, certify that this thesis is my own work and I have not obtained a degree in this University, or elsewhere, on the basis of this thesis.

_____

Róisín Ann Kelly

Abstract

Germanium was of great interest in the 1950's when it was used for the first transistor device. However, due to the water soluble and unstable oxide it was surpassed by silicon. Today, as device dimensions are shrinking the silicon oxide is no longer suitable due to gate leakage and other low-κ dielectrics such as Al_2O_3 and HfO_2 are being used. Germanium (Ge) is a promising material to replace or integrate with silicon (Si) to continue the trend of Moore's law. Germanium has better intrinsic mobilities than silicon and is also silicon fab compatible so it would be an ideal material choice to integrate into silicon-based technologies. The progression towards nanoelectronics requires a lot of in depth studies. Dynamic TEM studies allow observations of reactions to allow a better understanding of mechanisms and how an external stimulus may affect a material/structure. This thesis details in situ TEM experiments to investigate some essential processes for germanium nanowire (NW) integration into nanoelectronic devices; i.e. doping and Ohmic contact formation.

Chapter 1 reviews recent advances in dynamic TEM studies on semiconductor (namely silicon and germanium) nanostructures. The areas included are nanowire/crystal growth, germanide/silicide formation, irradiation, electrical biasing, batteries and strain.

Chapter 2 details the study of ion irradiation and the damage incurred in germanium nanowires. An experimental set-up is described to allow for concurrent observation in the TEM of a nanowire following sequential ion implantation steps. Grown nanowires were deposited on a FIB labelled SiN membrane grid which facilitated

HRTEM imaging and facile navigation to a specific nanowire. Cross sections of irradiated nanowires were also performed to evaluate the damage across the nanowire diameter. Experiments were conducted at 30 kV and 5 kV ion energies to study the effect of beam energy on nanowires of varied diameters. The results on nanowires were also compared to the damage profile in bulk germanium with both 30 kV and 5 kV ion beam energies.

Chapter 3 extends the work from chapter 2 whereby nanowires are annealed post ion irradiation. In situ thermal annealing experiments were conducted to observe the recrystallization of the nanowires. A method to promote solid phase epitaxial growth is investigated by irradiating only small areas of a nanowire to maintain a seed from which the epitaxial growth can initiate. It was also found that strain in the nanowire greatly effects defect formation and random nucleation and growth. To obtain full recovery of the crystal structure of a nanowire, a stable support which reduces strain in the nanowire is essential as well as containing a seed from which solid phase epitaxial growth can initiate.

Chapter 4 details the study of nickel germanide formation in germanium nanostructures. Rows of EBL (electron beam lithography) defined Ni-capped germanium nanopillars were extracted in FIB cross sections and annealed in situ to observe the germanide formation.

Chapter 5 summarizes the key conclusions of each chapter and discusses an outlook on the future of germanium nanowire studies to facilitate their future incorporation into nanodevices.

Acknowledgements

I would like to thank my supervisor Dr Nikolay Petkov for giving me this great opportunity and introducing me to the fascinating world of electron microscopy. As was stated by a past PhD student, "He is a very talented scientist and future generations of students could do well to pay attention to 50% of his ideas (the 50% that stand a chance of working)." He has some outrageously fantastic ideas, just figuring out how to implement them was the biggest challenge. I would also like to thank my co-supervisor Prof Justin Holmes for his help and guidance. I thank Dr Richard Farrell for giving me the initial push and helping me settle when I started the PhD. He was a great inspiration and his enthusiasm and drive are attributes I admire greatly. I thank Subhajit, Olan and Colm for keeping me supplied with grown Ge NWs. Thank you Anushka for all your work and help with the EBL. I thank Michael and Pat who I must have driven demented in EMAF. To my fellow MCAG members both past and present and the rest of the guys in 115 and 343, I thank you for making the time that bit easier and more enjoyable. I would also like to thank my collaborators Dr Bartosz Liedke, Dr Matthias Posselt and Mr Stefan Baldauf of Helmholtz Zentrum Dresden Rossendorf, Institute of Ion Beam Physics and Materials Research in Dresden.

I sincerely thank my family for their amazing support throughout my whole time in college. I thank Cian for being such a huge help and keeping me sane. Finally, I thank my son, Colm, for his incredible patience and understanding. He has endured 8 years of college with me and I think he deserves an honorary doctorate for that alone.

Dedicated to my little goose, Colm. His inspirational quotes (taken out of context) helped keep me going.

“Focus!”

“Hey, back to writing!”

Published Articles

Included in this thesis:

Kelly, R. A.; Holmes, J. D.; Petkov, N., Visualising discrete structural transformations in germanium nanowires during ion beam irradiation and subsequent annealing. Nanoscale 6, 12890-12897, doi:10.1039/c4nr04513k (2014). **Chapter 2**

Kelly, R. A.; Liedke, B.; Baldauf, S.; Gangnaik, A.; Biswas, S.; Georgiev, Y. M.; Holmes, J. D.; Posselt, M.; Petkov, N., Epitaxial Post-Implant Recrystallization in Germanium Nanowires. *Crystal Growth & Design* **15**, 4581-4590, doi:10.1021/acs.cgd.5b00836 (2015). **Chapter 3**

Other contributions:

Hobbs, R. G.; Farrell, R. A.; Bolger, C. T.; **Kelly, R. A.**; Morris, M. A.; Petkov, N.; Holmes, J. D., Selective Sidewall Wetting of Polymer Blocks in Hydrogen Silsesquioxane Directed Self-Assembly of PS-b-PDMS. *ACS Applied Materials & Interfaces* **4**, 4637-4642, doi:10.1021/am301012p (2012).

O'Driscoll, B. M. D.; **Kelly, R. A**.; Shaw, M.; Mokarian-Tobari, P.; Liontos, G.; Ntetsikas, K.; Avgeropoulos, A.; Petkov, N.; Morris, M. A., Achieving structural control with thin polystyrene-b-polydimethylsiloxane block copolymer films: The complex relationship of interface chemistry, annealing methodology and process conditions. *European Polymer Journal*, doi:http://dx.doi.org/10.1016/j.eurpolymj.2013.07.022.

Cummins, C.; Gangnaik, A.; **Kelly, R. A.**; Borah, D.; O'Connell, J.; Petkov, N.; Georgiev, Y. M.; Holmes, J. D.; Morris, M. A., Aligned silicon nanofins via the directed self-assembly of PS-b-P4VP block copolymer and metal oxide enhanced pattern transfer. *Nanoscale* **7**, 6712-6721 (2015).

Cummins, C.; **Kelly, R. A.**; Gangnaik, A.; Georgiev, Y. M.; Petkov, N.; Holmes, J. D.; Morris, M. A., Solvent Vapor Annealing of Block Copolymers in Confined Topographies: Commensurability Considerations for Nanolithography. *Macromolecular rapid communications* **36**, 762-767 (2015).

Cummins, C. Gangnaik, A.; **Kelly, R. A.**; Hydes, A. J.; O'Connell, J.; Petkov, N.; Georgiev, Y. M.; Borah, D.; Holmes, J. D.; Morris, M. A., Parallel Arrays of Sub-10 nm Aligned Germanium Nanofins from an In Situ Metal Oxide Hardmask using Directed Self-Assembly of Block Copolymers. *Chemistry of Materials* **27**, 6091-6096, doi:10.1021/acs.chemmater.5b02608 (2015).

Common abbreviations and acronyms

c/a: crystalline-amorphous

EBID: Electron beam induced deposition

EBL: Electron beam lithography

FEG: Field emission gun

FIB: Focused ion beam

Ge: Germanium

GeOI: Germanium-on-insulator

HRTEM: High resolution transmission electron microscopy

HSQ: Hydrogen silsesquioxane

IBID: Ion beam induced deposition

IPA: isopropyl alcohol

LMIS: Liquid metal ion source

NP: nanoparticle

NW: nanowire

RNG: Random nucleation and growth

sccm: Square cubic centimetres per minute

SEM: Scanning electron microscope

Si: Silicon

SiN: Silicon nitride

SPEG or **SPER:** Solid phase epitaxial (re)growth

SRIM: Stopping and range of ions in matter

STEM: Scanning transmission electron microscope

TEM: Transmission electron microscope

Contents

Declaration i
Abstract iii
Acknowledgements v
Published Articles vii
Common abbreviations and acronyms viii
Chapter 1. Introduction 1
1.1. Abstract 2
1.2. Motivation and Background 2
1.3. Nanowire/Crystal growth 4
1.4. Germanide/Silicide Formation 10
1.5. Irradiation 15
1.6. Electrical Biasing 17
1.7. Batteries 21
1.8. Strain 24
1.9. Conclusions 28
1.10. References 29
Chapter 2. Experimental Methods 36
2.1. Instrumentation 37
2.2. Nanowire Fabrication 37
2.2.1. Grown Nanowires 38
2.2.2. Lithography defined fabricated nanowires 38
2.3. Nanowire Irradiation via FIB 39
2.3.1. Concurrent imaging platform for grown nanowires 39
2.3.2. Irradiation of grown nanowires 40
2.3.3. Irradiation of EBL defined GeOI Nanowires 42
2.4. HRTEM of irradiated nanowires 45
2.4.1. HRTEM of irradiated grown nanowires 45
2.4.2. HRTEM of irradiated lithography defined GeOI nanowires 45
2.5. In situ annealing of irradiated nanowires 46
2.6 Iradina (ion range and damage in nanowires) 46
2.7 Nickel-capped germanium nanopillar fabrication 47

2.8. TEM characterisation of Ni-capped Ge nanopillars 50
2.8.1. HRTEM of Ni-capped Ge nanopillars 50
2.8.2. In situ annealing of Ni-capped Ge nanopillars 50
2.9 References 51
Chapter 3. Investigating crystal damage in germanium nanowires due to ion beam irradiation 53
3.1. Abstract 54
3.2. Introduction 54
3.3. Experimental Procedure 56
3.3.1 Instrumentation 56
3.3.2 Nanowires 56
3.3.3. Concurrent imaging platform 57
3.3.4. Iradina (ion range and damage in nanostructures) 59
3.4. Results and Discussion 59
3.4.1. 30 kV single exposure irradiation 59
3.4.2. Concurrent stepwise 30 kV irradiation 64
3.4.3. 5 kV irradiation 70
3.5. Conclusions 74
3.6. References 75
Chapter 4. Epitaxial post-implant recrystallization in germanium nanowires 78
4.1. Abstract 79
4.2. Introduction 79
4.3. Experimental Procedure 83
4.3.1. Concurrent imaging platform and irradiation 83
4.3.2. Irradiated EBL defined GeOI Nanowires 83
4.3.3. In situ anneal 86
4.4. Results and Discussion 86
4.4.1. Recrystallization of nanowire with extensive amorphisation 86
4.4.2. Recrystallization of nanowire with partial amorphisation 89
4.5 Conclusions 102
4.6 References 103
4.7. Appendix 109
Chapter 5. Investigating the formation of nickel germanides in germanium nanostructures 113

5.1. Abstract 114
5.2. Introduction 114
5.3. Experimental 117
5.3.1. Ni-capped Ge nanopillar preparation. 117
5.3.2. TEM Characterization 121
5.4 Results and Discussion 121
5.4.1 Sample 1 121
5.4.2. Sample 2 129
5.4.3. HRTEM of Ni seeded Ge NW growth 136
5.5. Conclusions 138
5.6. References 138
5.7 Appendix 142
Chapter 6. Conclusions and Outlook 143
References 148

Chapter 1

Introduction

1.1. Abstract

This chapter covers the theme of dynamic transmission electron microscopy (TEM) addressing the challenges associated with germanium (Ge) and silicon (Si) nanowire incorporation for future nanoelectronics. A vast array of in situ TEM experiments delving into the unique properties of group IV semiconductor nanowires have been published in recent years. This chapter presents a brief overview of the in situ work for NW growth, crystallisation, irradiation, stress, electrical biasing and batteries. Dynamic TEM provides an insight into a process and can help to understand mechanisms of crystal growth, defect formation, fractures and chemical reactions such as lithiation. Although in situ TEM is an excellent tool to observe processes as they occur, limitations of the technique need to be taken into account and this is also discussed in this chapter.

1.2. Motivation and Background

Germanium was used for the first transistor device but due to processing issues, i.e. primarily its water soluble and thermally unstable native oxide,[1,2] it had been set aside to make way for the boom of the silicon era. In contrast, Si possesses a thermally stable oxide which is not soluble in water. As the dimensions of silicon devices have scaled down, failure of the gate oxide became problematic and hence SiO_2 was no longer suitable. The introduction of higher mobility materials such as Ge has become more attractive for "Beyond Si" technologies to increase electronic device performance. A possible integration or introduction of Ge in current processes would complement high-κ material use for gate oxide use function.[3,4]

With the ever increasing demand for faster and smaller transistor devices, the outcome of a nanowire device has become inevitable. Nanowires are appealing as a device channel due to ballistic transport.[5] Nanowires are one-dimensional crystals of an element or compound materials with diameters in the sub-100 nm range and high aspect ratios, with lengths up to hundreds of microns long. The excellent electrical, optical and mechanical properties of semiconductor nanowires (in comparison to their bulk counterparts) have been the driving force for their research.[6,7]

Si and Ge nanowires are typically produced either via top-down or bottom-up techniques.[8-11] Bottom-up refers to nanowire growth from precursors and top-down refers to using a larger substrate as the starting material from which smaller structures are defined. The bottom-up growth methods produce near-perfect crystals with well-defined facets, which is crucial as surface energies are important due to the large surface-area/volume ratio. For the top-down NW fabrication approach, a lithography (EBL or UV-lithography followed by a trimming etch step) system is used to define lines or dots to produce either vertical or horizontal nanowires. This method allows accurate control over diameter and orientation of the nanowires produced. EBL defined nanowires have a long process time, including requiring an etch recipe with a high etch selectivity over the hard mask, and achieving nanowires with a low line edge roughness anywhere near comparable to grown nanowires is challenging. The roughness of a lithography defined nanowire depends on both the roughness of the mask as well as the etch process. The applicability of grown nanowires for high volume manufacturing practices is still doubtful, and this is mainly due to alignment into a practical device and the need for precise control of diameter distribution and growth directions. The advantages grown nanowires have

over lithography defined nanowires include direct access to smaller diameter wires, larger productivity, relatively inexpensive equipment and atomically flat facets.

The resolution of electron microscopy has been pushed to the limit to allow single atom imaging on monolayer samples such as graphene and other 2-D materials. This has been achieved with the instrumental advance of monochromators and aberration correctors on the imaging and probe-forming lenses.[12] New avenues have been explored by utilising (S)TEM for dynamic observations. In-situ TEM allows for a direct observation upon the application of an external stimulus to the sample. An array of in-situ TEM holders have been developed over the past decade which allow a vast range of properties to be explored within the TEM ranging from the classical heating and cooling to nanoindentation,[13] environmental liquid/gas,[14] electrical biasing, magnetizing,[15] and combinations of these. Nanosecond in situ TEM has also been developed to capture processes which occur much faster than is capable with traditional in situ TEM.[16-19] Nanosecond resolution in the TEM is achieved using laser stimulation of a photoemission source with achievable resolutions times as short as 15 ns. Standard modern TEMs require a sufficient exposure, usually 1 s, to achieve a high resolution image using conventional CCD camera systems. Many important steps in a process which happen within a ns are missed.

1.3. Nanowire/Crystal growth

Environmental holders for (S)TEM present a route to understand the mechanism of nanowire growth by direct observation in situ.[20] Hammar et al studied the epitaxial growth of Ge on Si(001) with a double tilt heating stage in a modified TEM with a gas injection into the chamber.[21] Now, commercially available environmental

holders are capable of injection of precursor gases at precise pressures and thermal control of the cell which provides suitable conditions for NW growth. Hannon et al. demonstrated that Au diffusion affects the length, shape and sidewall properties, during Au-seeded Si NW growth.[22] Ostwald ripening of Au droplets during the growth was observed to form larger ones and hence variation of diameter occurs. The authors deduced that the Si NW growth is limited by Au diffusion. In a separate report, Kodambaka et al. investigated the effect of oxygen on the VLS growth mechanism through in situ TEM observations.[23] It was shown that the oxygen suppresses the diffusion of the Au catalyst used for growth. As the oxygen pressure was decreased as shown in Figure 1.1 (a), the diffusion of the Au seed into the Si NW was observed. However, as the oxygen pressure was increased, as displayed in Figure 1.1 (b), retention of the Au seed at the top of the NW is clear.

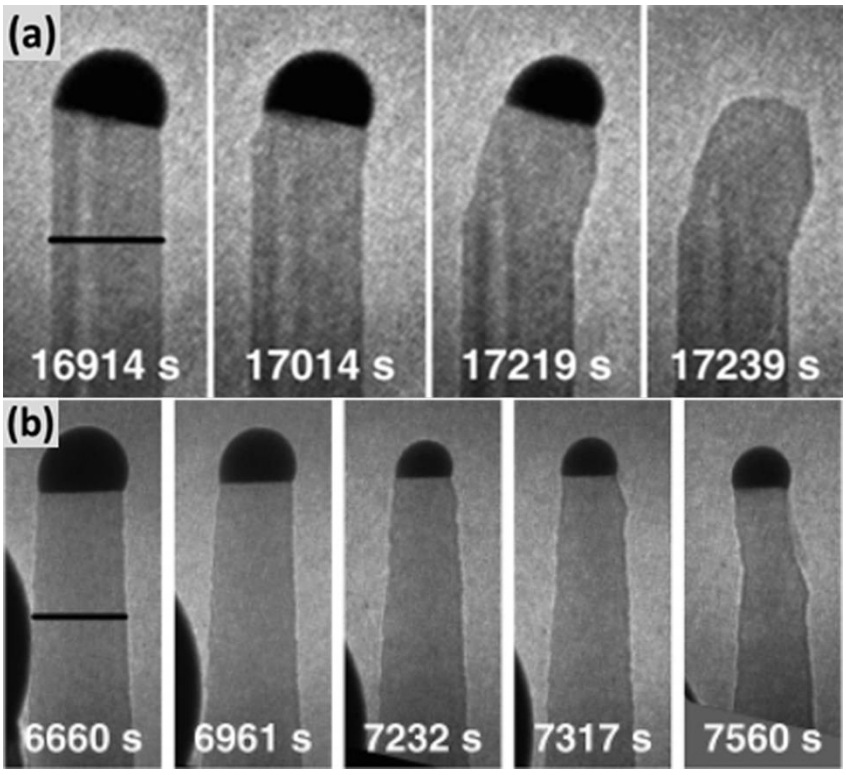

Figure 1.1. (a) Images from a video of Si NW in an environmental TEM holder with a decrease in oxygen pressure in the presence of disilane. Scale bar is 40 nm. (b) Images from a video of Si NW with the increase of oxygen. The migration of the Au droplet causes tapering of the nanowire. Scale bar is 50 nm. Reproduced from Kodambaka et al. (2006).[23]

An interesting report by Hillerich et al. utilised in situ and ex situ TEM to study the formation of hybrid group III-V/group IV heterostructure NWs.[24] Growth of Si NWs was also performed and it was found that kink formation can be controlled by changing the droplet volume due to migration of Au from the seed droplet to other droplets via Ostwald ripening.

Other researchers have shown evidence for Ge NW volume changes of Ge NW encapsulated in a carbon (C) shell. Holmberg et al. carried out a systematic study on the migration of the Au seed of a Ge NW encapsulated within a C shell.[25] The C shell restricted the volume of the NW and seed during in situ thermal annealing. The encapsulated NW was annealed with an increasing temperature up to 900 °C. From approximately 350 °C the Au seed melted and migrated down the NW leaving crystalline Ge in its place. The migration of the Au from the position of the seed into the nanowire volume is shown in Figure 1.2.

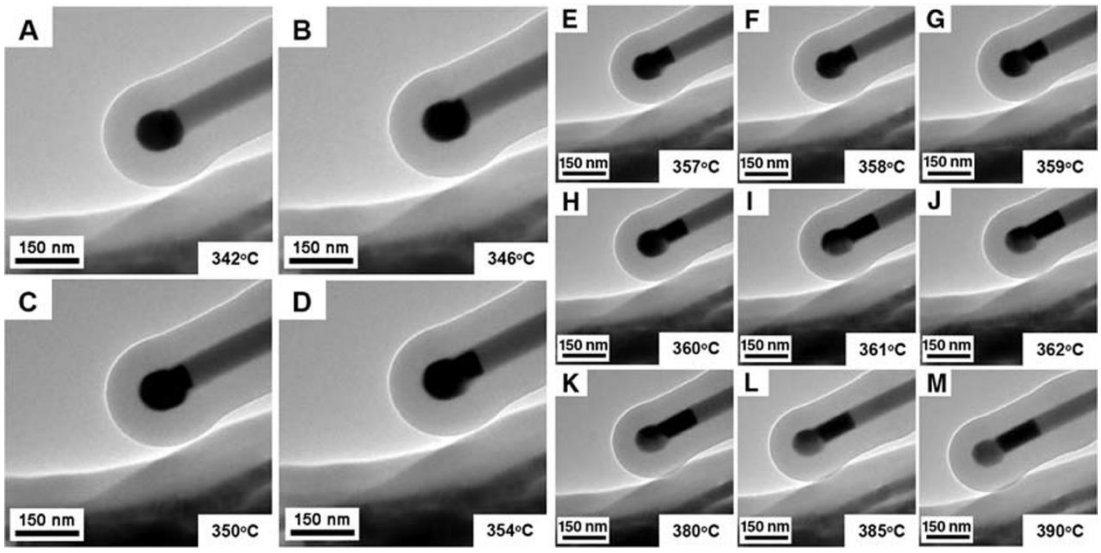

Figure 1.2. Images from in situ anneal of C-encapsulated Au-seeded Ge NW up to 390 °C. Reproduced from Holmberg et al. (2009).[25]

Sharma demonstrated Au particle deposition in an environmental holder.[26] The cell was used as a CVD (chemical vapour deposition) chamber relying on the decomposition due to heat or electron beam radiation of adsorbed precursors on the substrate for the deposition of Au particles. The effect of the electron beam on the CVD of Au particles was investigated and it was found that at elevated temperatures the energy from the electron beam radiation is negligible, however it was advised to quantify a reaction in the TEM both with and without exposure to the beam to ensure the effects seen are due to the external stimulus and not by the energy of the electron beam. Sharma also investigated Si NW growth using Au or Pd particles in the cell, leaking in undiluted disilane (which is the precursor used for Si NW growth), and observed growth via a vapour solid-solid (VSS) mechanism.[26] It was established that the diffusion of Si was not the rate determining step of Si NW growth with Pd seed but in fact Pd is the migrating species, i.e. Pd diffusion away from the silicide formed seed formed during nanowire growth. This is proposed by Sharma et al. due to the low activation energy calculated (0.02eV) for the Si NW growth and higher than expected growth rate.

Biswas et al. studied growth kinetics of Ge NWs with varied Au/Ag seeds by in situ observation of the eutectic alloy upon heating and its shape and geometry relative to the Ge NW.[27] It was found that the interface between the eutectic alloy and Ge NW depends on the composition of the eutectic alloy. The in situ studies carried out showed that Ag-rich eutectic alloys form nearly flat ($\theta = 80°$) interfaces with the Ge NW during growth and correlates well with the higher growth kinetics of Ag-rich eutectic alloys observed (Figure 1.3).

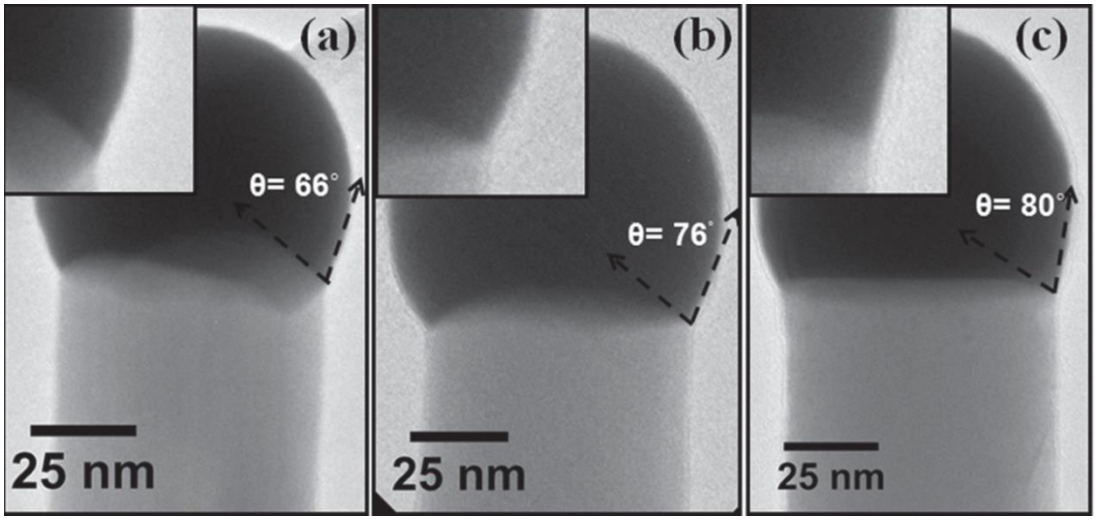

Figure 1.3. (a) Au-Ge, (b) $Au_{0.75}Ag_{0.25}$ and (c) $Au_{0.65}Ag_{0.35}$ eutectic alloys with varied contact angles with the NW facets, imaged in a TEM with an in situ heating stage at 460 °C. Reproduced from Biswas et al. (2015).[27]

In a similar work, O'Regan et al. investigated the supersaturation and growth kinetics of Ge NWs using Au/Ge bilayer films.[28] Binary films were annealed and observed in situ using dark field diffraction contrast to identify the melted and coalesced alloy NPs as a function of Au/Ge composition. It was determined that a higher concentration of Ge results in a faster formation of the liquid alloy, i.e. the particle "disappears" in the dark field contrast due to loss of diffracted beams.

An insightful new method to observe in situ synthesis of Si NWs in a TEM via pulsed laser ablation (PLA) has also been reported.[29] This method allows for a direct observation of a NW before, during, and after ablation and without the need of the introduction of a precursor. Instead a Si substrate with a 4 nm Au layer is introduced into the TEM where the sample is ablated. The authors also proposed a mechanism whereby the Au film is broken up into droplets after an initial laser pulse after which they form an alloy with the Si which then acts as the catalyst for the NW growth.

Other researchers have demonstrated self-seeded Ge NW growth.[30] The in situ experiments were conducted in a heating stage under vacuum of NWs grown ex situ but with remaining Ge particles surrounding the NWs. Diffusion via Ostwald ripening of the nanoparticles (NPs) surrounding the NWs was observed during thermal annealing resulting in larger diameters. Another issue included in the study by Lotty et al. is the effect of electron beam energy on the observed nucleation of Ge NPs from the precursor as shown in Figure 1.4. This experiment, as well as demonstrating how the Ge nanoparticles nucleate, also demonstrates the reorganisation of the crystalline particles due to high energy electron beam. The mechanism of similar processes for Au NPs has been studied by lattice resolution imaging and the mechanism of attachment and reorientation of crystals into extended structures was proposed.[31] Orientated attachment of initial seeds was suggested for metal-free growth of Ge NWs.[32]

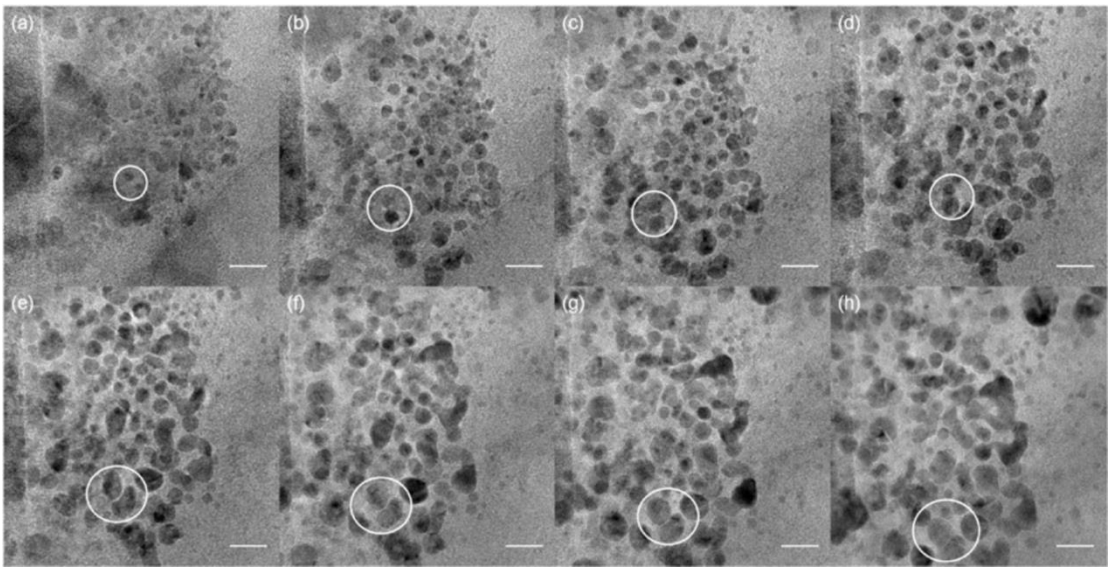

Figure 1.4. Sequence showing the nucleation, diameter broadening and coalescence of Ge nanoparticles from a Ge:Si precursor as imaged in a 200 kV TEM. All scale bars are 20 nm. Reproduced from Lotty et al. (2013).[30]

1.4. Germanide/Silicide Formation

A germanide is formed between Ge and a more electropositive metal such as Cu, Pt, Mg, Na, W, Ti and Ni, this is analogous with Si/silicides. A germanide/silicide facilitates a good contact to the semiconductor which would otherwise produce parasitic resistance with a metal contact. The ideal germanide formed would be single crystalline and form an atomically flat interface with Ge.[33] The main issue is controlling the phase of the germanide formed. This is exemplified by the complex phase diagram for the Ni-Ge system as shown in Figure 1.5.[34]

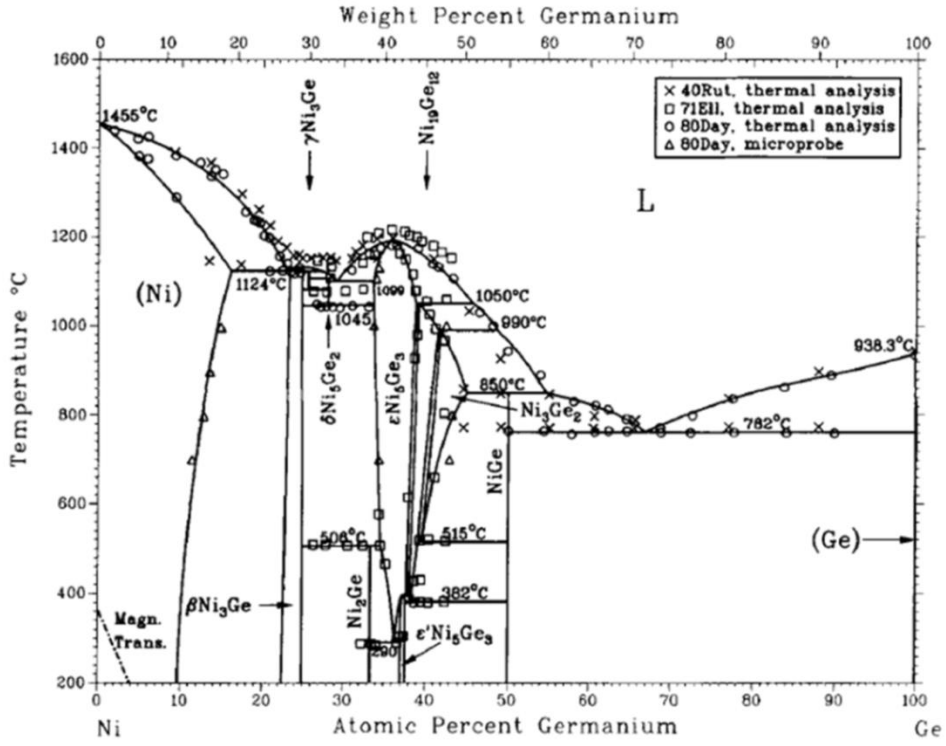

Figure 1.5. Phase diagram of the Ni-Ge system. Reproduced from Nash et al. (1987).[34]

Chou et al. observed the nucleation of epitaxial $NiSi_2$ in [110] grown Si nanowires in ultra-high vacuum (UHV) TEM at approximately 800 °C.[35] The defect free and

atomically flat silicide formation (Figure 1.6) was greatly attributed to the good lattice match of Si and $NiSi_2$. A mechanism is proposed where by the phase change occurs via hetero or homogeneous nucleation, based on the results from the in situ observations of epitaxial growth of $NiSi_2$ in Si NWs in the [110] direction. The lattice match between Si and $NiSi_2$ facilitates the epitaxial step to form the atomically flat interface between Si and the silicide.

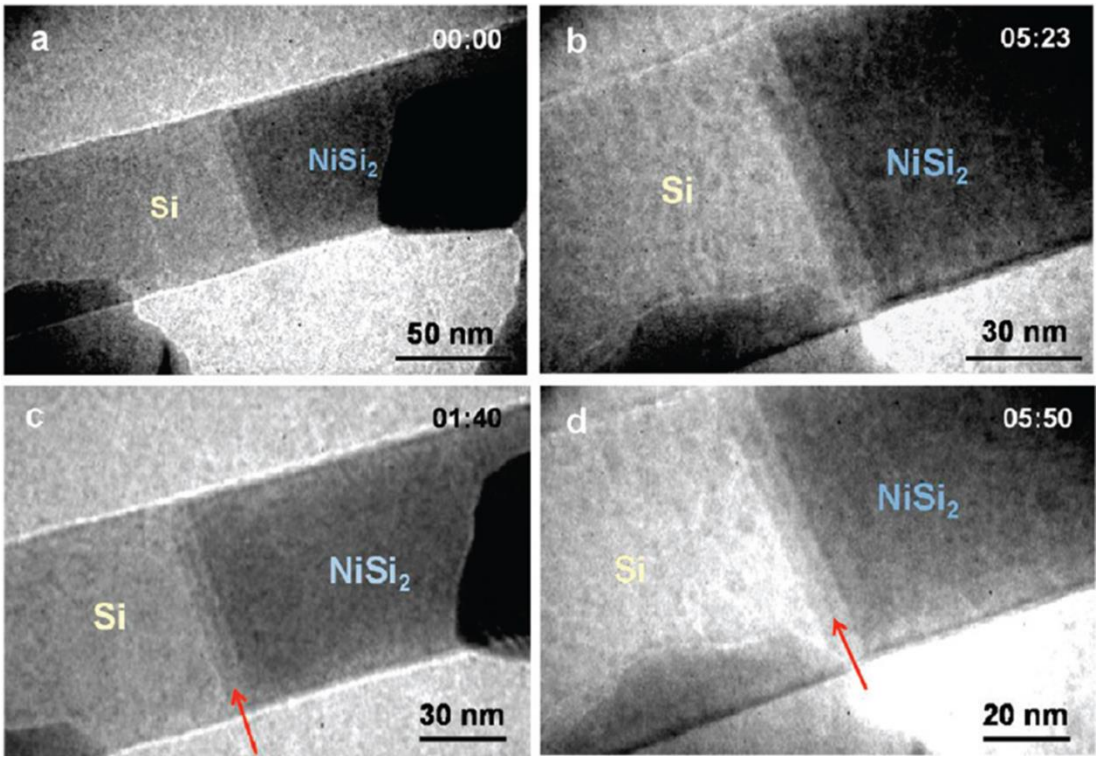

Figure 1.6. TEM images acquired during the in situ anneal (approx. 800 °C) of a $Si/NiSi_2$ interface of a NW. (a) and (b) show an initial displacement of the interfaces due to silicide growth. (c) and (d) show displacement of another interface between the Si and $NiSi_2$. Reproduced from Chou et al. (2010).[35]

It was predicted by Wittmer et al., using the rule proposed by Walser and Bené,[36] that the initial germanide phase to form is Ni_2Ge followed by NiGe.[37] Nath et al. investigated the formation of germanides in-situ in UHV TEM by reactive deposition epitaxy.[38] Ni was evaporated in-situ at 300 °C onto Ge(001) via electron beam evaporation. The Ni_2Ge phase is completely avoided using reactive deposition

epitaxy. Instead a NiGe phase formed with the relationship to the Ge given by NiGe($\bar{1}$01)//Ge(001) and NiGe[010] //Ge[110]. Similarly, Deng et al. investigated the formation of NiGe on Ge(001) via reactive deposition in situ at 350 °C in situ in an UHV TEM.[39] The relationship determined was NiGe(111)//Ge(001) and NiGe[0$\bar{1}$1]// Ge[110]. The different relationships observed were attributed to the variation of the Ge substrate thickness in the two studies.

Lee et al. deposited a Zr layer on a (100) Ge substrate prior to Ni layer deposition in a DC magnetron sputtering system.[40] The Zr layer was incorporated to reduce germanide agglomeration and it was found to have also improved the thermal stability of the germanide. The germanide formation was observed in situ and images from the anneal are shown in Figure 1.7. A previous similar study by the authors using a Ta interlayer was performed.[41]

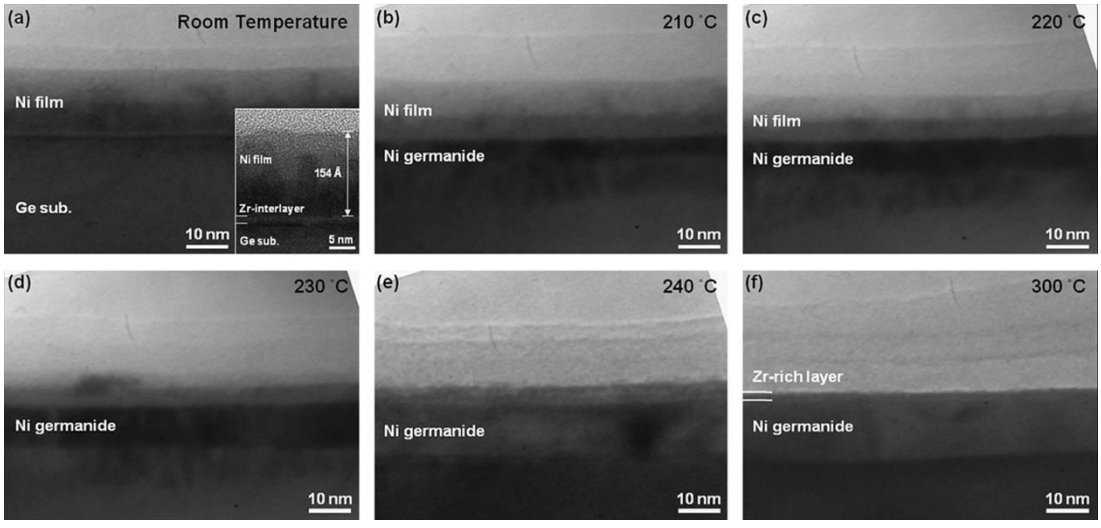

Figure 1.7. Images from video sequence of the anneal of a cross section of the Ni/Zr/Ge system up to 300 °C. Reproduced from Lee et al. (2012).[40]

Void formations in Ni-Ge core-shell NPs during the solid state reaction of germanide formation has been studied through dynamic TEM.[42] The voids are formed via the

Kirkendall effect which is a motion of the boundary between Ni and Ge due to the higher diffusion rate of Ni into Ge. A schematic depicting the sample set up and images acquired during the in situ anneal is presented in Figure 1.8. The final NP structures after diffusion varied from fully hollow, yolk-shell and porous NPs. The size of the original core-shell NPs dictates the final NP structure after diffusion. For the smallest NPs (approximately 50 nm core diameter), the small voids grow into larger voids until the hollow structures are formed. For medium sized NPs (approximately 80 nm core diameter), void formation occurs at the Ni/Ge interface and as the voids grow the core atoms are disconnected from the shell and hence cannot diffuse resulting in the yolk-shell structures. For the larger NPs (approximately 200 nm core diameter), there are sufficient core atoms to diffuse but as the shell reaches a fully reacted or saturated state the diffusion does not continue and hence porous NPs are produced.

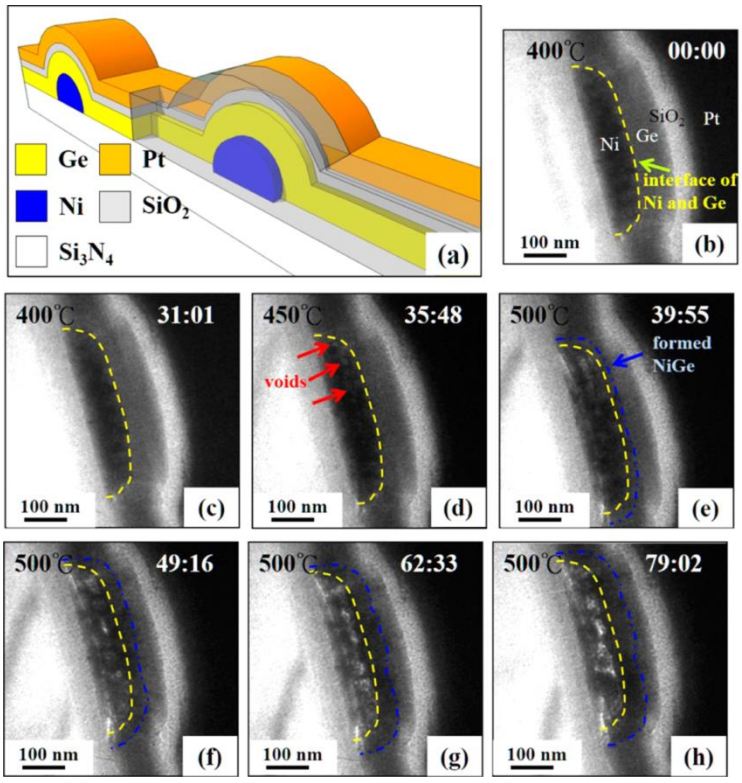

Figure 1.8. (a) Schematic of the Ni-Ge core-shell sample. (b-h) Images acquired during the in situ anneal at 450 °C. Reproduced from Lai et al. (2014).[42]

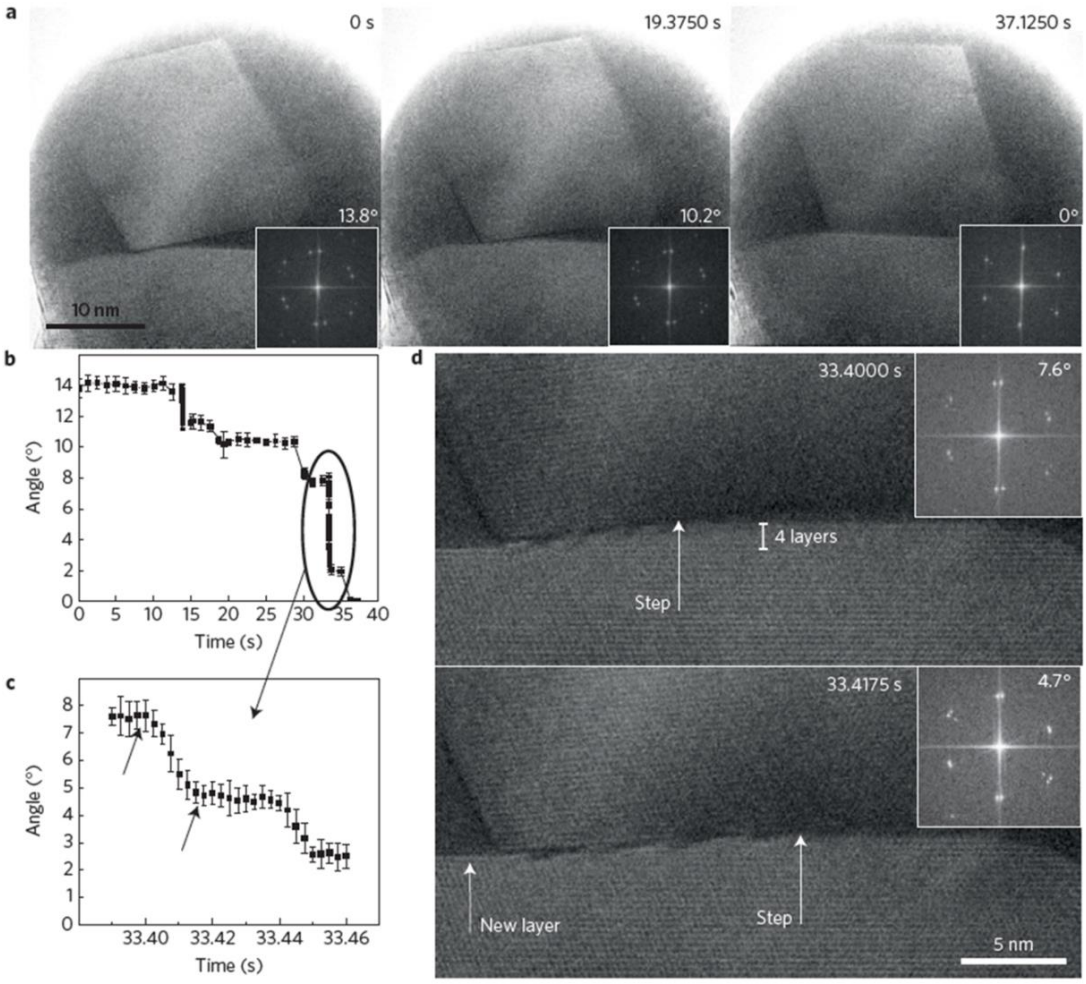

Figure 1.9. Images from the in situ anneal at 400 °C of the NW containing the NiSi crystal within the Au droplet showing the docking of the silicide particle with the NW. (a) A sequence of images were recorded at 400 fps. (b) The rotation angle measured from the FFTs of the image series in (a). (c) Larger rotation which occurred in two distinct increments; arrows indicate the data corresponding to the images in (d). (d) Rearrangement of the Si surface during silicide rotation. Reproduced from Paciera et al. (2015).[43]

Panciera et al. have presented lattice resolution dynamic TEM results of a Ni-silicide particle within the Au seed of a grown Si NW.[43] A 1 nm Ni layer, approximately, was deposited in situ by evaporation followed by an oxidation step to oxidise the NW sidewalls and promote Ni incorporation selectively into the Au seed. NW growth conditions were continued with a flow of silane (Si_2H_6) at 350 °C with an increase to 500 °C. Ni and Si reacted as the temperature passed the eutectic point

and the AuSi droplet reformed. The Ni-silicide particle was observed within the droplet (light contrast area in Figure 1.9a). The authors suggest that the solid inclusion may be a single octahedral nanocrystal or smaller nanocrystals that coalesced to form the large single octahedral $NiSi_2$ crystal. The images presented in Figure 1.9 show the rotation of the silicide particle within the Au droplet to align with the Si NW.

1.5. Irradiation

The understanding of ion beam damage on a substrate is a topic covered from many different perspectives. The ion beam can be used to define nanostructures,[44] introduce dopants atoms,[45] and manipulate nanostructures. Manipulation of nanostructures with the ion beam has been demonstrated for GaAs,[46] ZnO,[47] SiO_2,[48] Si[49,50] and Ge[51] nanowires by inducing bending in the nanowire with a dependence on energy and incidence angle of ion beam. There are varying reports on the precise mechanism(s) underpinning nanostructure manipulation under the ion beam and these have been attributed the bending to a combination of tensile and compressive strain due to the formation of vacancies and interstitials,[47] the possibility of densification due to irradiation as well as the possibility of tensile strain,[51] and the bending in Si nanowires to internal stresses due to the formation of a crystalline/amorphous interface.[49] A mixture of results occurred for the annealing of the irradiated bent nanowires with some retaining the bent structure and others recovering the straight nanowire. Pecora et al. present both in their study; the bent nanowires were polycrystalline and the straight nanowires were single crystalline.[49] This raises a question about the recrystallization of the nanowire, whether it occurred

via a predominantly SPER (solid phase epitaxial regrowth) or RNG (random nucleation and growth) mechanism. If SPER is the predominant recrystallization mechanism the remaining crystal seed should facilitate single crystal growth. However, if RNG is predominant a polycrystalline structure is probable. The competition between SPER and RNG is important to consider as it is favourable to promote SPER and hopefully single crystalline (ideally defect free) recovery post ion irradiation.[52] Hinks presents a thorough overview of the history of progression of ion irradiation studies and the prospects of dynamic TEM.[53] The author discussed important factors including the choice of ion beam and how the samples are prepared.

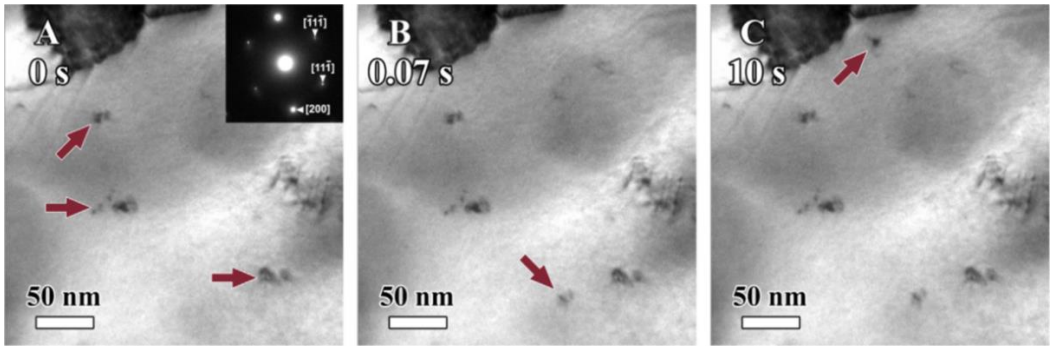

Figure 1.10. Frames from the in situ video of irradiation of Au foil with 48 MeV Si^{8+}. The red arrows in A indicate intrinsic defect clusters (which may be due to the FIB cross section preparation). After 1 frame (0.07 s) new a new defect cluster, marked with a red arrow in B, is observed. After several more seconds another defect cluster is observed in C. Reproduced from Hattar et al. (2014).[54]

Hattar et al. presented a modified TEM system which allows for in situ ion irradiation.[54] The system is also capable of observation of mechanical loading and corrosive environments. Results presented by Hattar et al. on Au foils, irradiated with 48 MeV Si^{8+} and a fluence of approximately 6.7×10^{9} cm^{-2} s^{-1} are shown in Figure 1.10. The TEM system is equipped with a TVIPS 4k × 4k camera (custom designed, CMOS technology with active pixel sensors) which allows the user to

acquire high quality single electron sensitive images as well as an additional retractable 1k × 1k camera for the video acquisition of up to 30 fps (frames per second).

Electron beam irradiation can also induce defect formation at high energies (>200 keV). Fedina et al. utilised a 400 keV TEM to induce point defect formation in Si.[55] The flux of electrons during the experiments was estimated to be approximately 10^{20} cm^{-2} s^{-1}. These point defects were initiated to study the evolution of {113} defects, which are attributed to the problem of transient enhanced diffusion of dopants during annealing in Si devices. From the in situ HRTEM results, combined with the modelling calculations, it was concluded that the {113} defect formation is due to the aggregation of self-interstitials and vacancies. The mechanism, which occurs via the formation of planar four fold coordinated point defects, was determined using the in situ TEM images during the defect propagation. Vanhellemont et al. investigated the irradiation of Si nanostructures with a 2 MeV electron beam.[56] It was found that high boron dopant concentrations suppress {113}-defect formation in larger (>100 nm diameter) nanostructures but actually promotes the defect formation in smaller (<100 nm diameter) nanostructures. A dependence on diameter was not observed for As doped structures and this is attributed to intrinsic point defect annihilation, out-diffusion and interaction with the dopant atoms.

1.6. Electrical Biasing

Observation of nanostructures during electrical biasing is of interest due to the occurrence of Joule heating and electromigration-induced mass transport and

external stresses which may alter the electrical properties of a NW. Gobulukoglu and Robertson proposed the investigation of electromigration of nanoscale interconnects on SiN membranes with in situ scanning transmission electron microscopy (STEM).[57] The applicability was initially demonstrated by Gobulukoglu and Robertson by observing the structural changes of sputtered Al during in situ thermal annealing.[57] Hummelgård et al. studied the Joule heating of $Mo_6S_3I_6$ NWs using an in situ TEM probe holder.[58] It was observed that during the electrical biasing, the NWs thermally degraded to Mo NWs and an increase in conductivity was observed throughout the annealing phases. To determine the temperature due to Joule heating, Au nanoparticles NPs were deposited on the NWs and observed during the probing (Figure 1.11). It was determined that due to the melting of the Au NPs, the temperature reaching above 1000 °C.

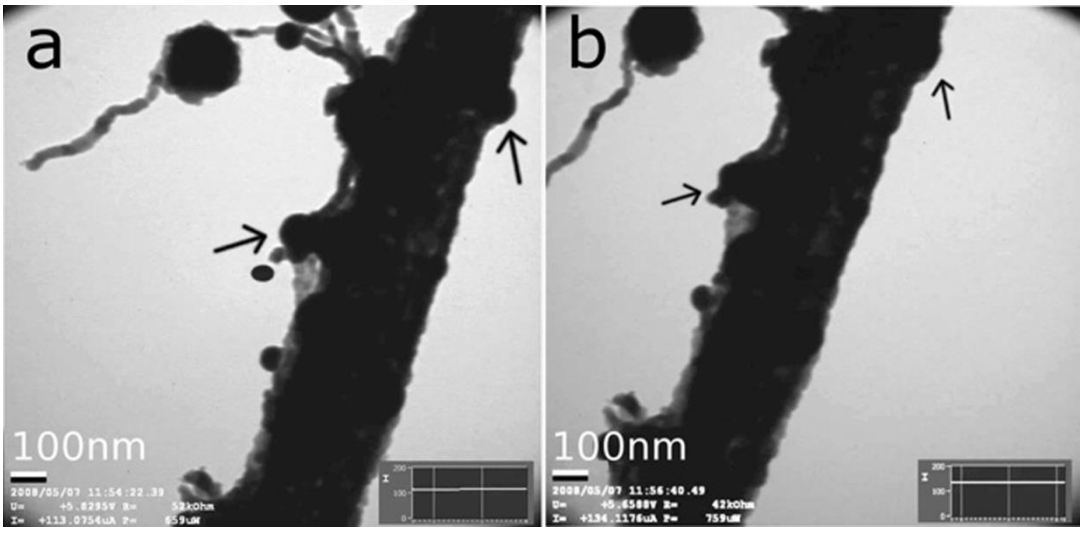

Figure 1.11. Au NPs (indicated with arrows) deposited on MoSI NWs during probing to estimate the temperature due to the Joule heating. The images show (a) before melting and (b) after melting of the Au NPs. Reproduced from Hummelgård et al. (2010).[58]

Lei et al. fabricated custom in situ TEM devices by focused ion beam (FIB) of Si membranes.[59] FIB preparation of the Si NWs caused amorphisation of the NWs. Four-point measurements on FIB-defined amorphous Si NWs showed a higher

resistance than bulk crystalline Si. In situ recrystallization of the NWs was observed due to resistive heating, as shown in Figure 1.12 where a NW crystallised at 54 μA to produce a polycrystalline NW. The mechanism of recrystallization is related to the degree of amorphisation of the NW. With recrystallization, recovery of resistivity (comparable to bulk properties) is observed.

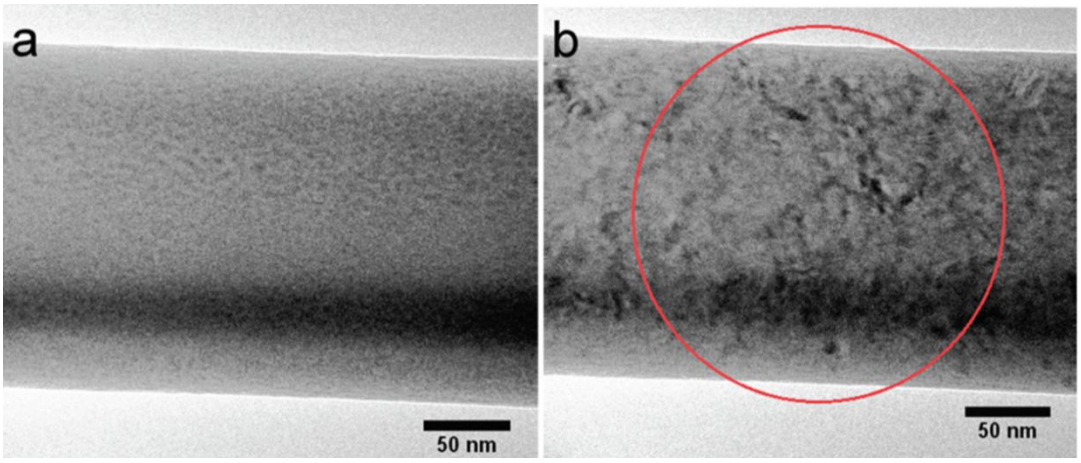

Figure 1.12. (a) TEM of a NW before current annealing and (b) after sudden change in crystal structure (polycrystalline) due to current annealing at 54 μA. Reproduced from Lei et al. (2010).[59]

Kallesøe et al. demonstrated Si NW devices by growing the NWs via VLS method on Si cantilevers.[60] The NWs were grown in situ to form bridges between two cantilevers. The experimental set up is shown in Figure 1.13 (a) and (b). The NW is grown from the heated cantilever to the unheated cantilever. A solidification of the AuSi seed is observed (Figure 1.13 c) and precipitation of Si (indicated with the white arrow). Kallesøe et al. demonstrated the controlling of the connection between the Si NW and the cantilever by adjusting the Au migration during growth. In situ electrical measurements of the NWs suggest p-type doping has an effect on the resistivity of the NW connection as well as Au deposits on the surface which form during growth.

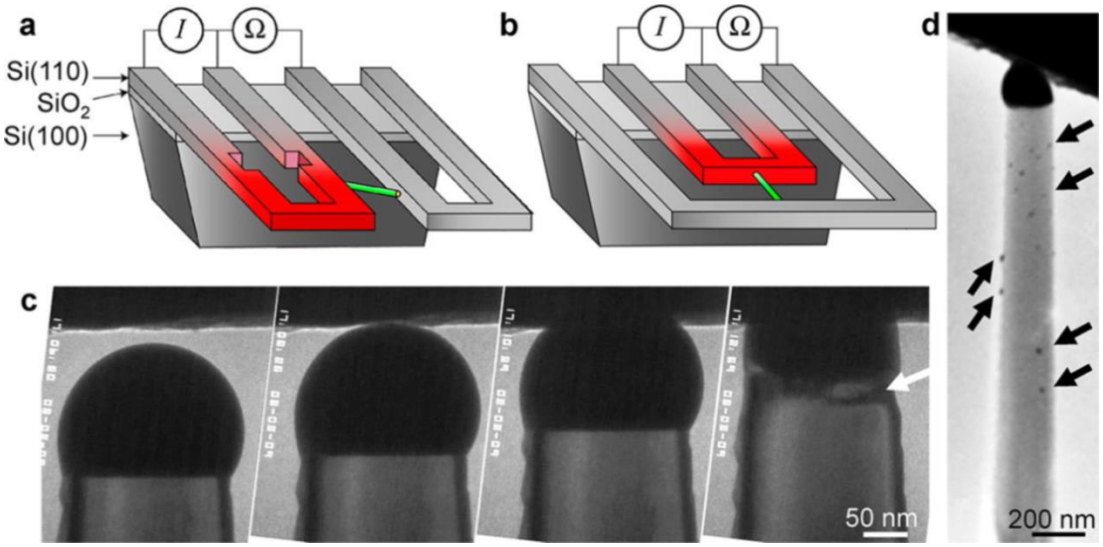

Figure 1.13. (a) and (b) Schematics of experimental set up for in situ NW connection formation between two cantilevers and in situ electrical testing. The NW (green) is grown form the heated cantilever (red) to the second (unheated) cantilever. (c) In situ growth is observed to form the connection between the cantilevers. (d) Au deposits on the surface due to Au migration are identified with black arrows. Reproduced from Kallesøe et al. (2012).[60]

As an alternative, Westenfelder et al. demonstrated the use of graphene based sample supports for in situ TEM electrical investigations.[61] Graphene was chosen as a support material due to its electrical conductivity which means a current can be passed through it while also being thin enough (up to only a few atomic layers) for TEM imaging. Westenfelder et al. utilised a suspended graphene layer to observe the change of Au NPs with a current applied and hence heating of the NPs as shown in Figure 1.14.

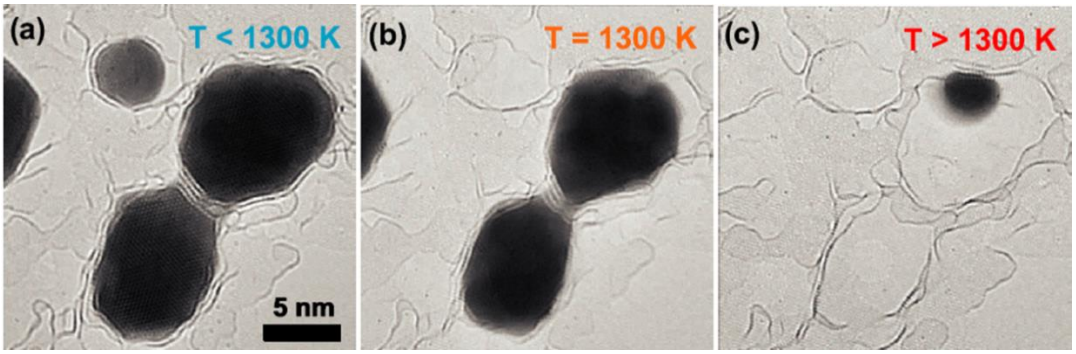

Figure 1.14. TEM images of Au NPs during (a) below 1300 K, (b) at 1300 K and (c) above 1300 K. Reproduced from Westenfelder et al. (2011).[61]

1.7. Batteries

Liu et al. fabricated the first "nanobattery" for in situ observation of battery charging and discharging.[62] A review of the work by the group is presented showcasing the range of results produced from the in situ TEM set ups shown in Figure 1.15. Si and Ge are among a range of materials which have a high energy storage capacity (1384 and 3579 mA h g^{-1}, respectively) and hence are attractive for use in lithium ion batteries.

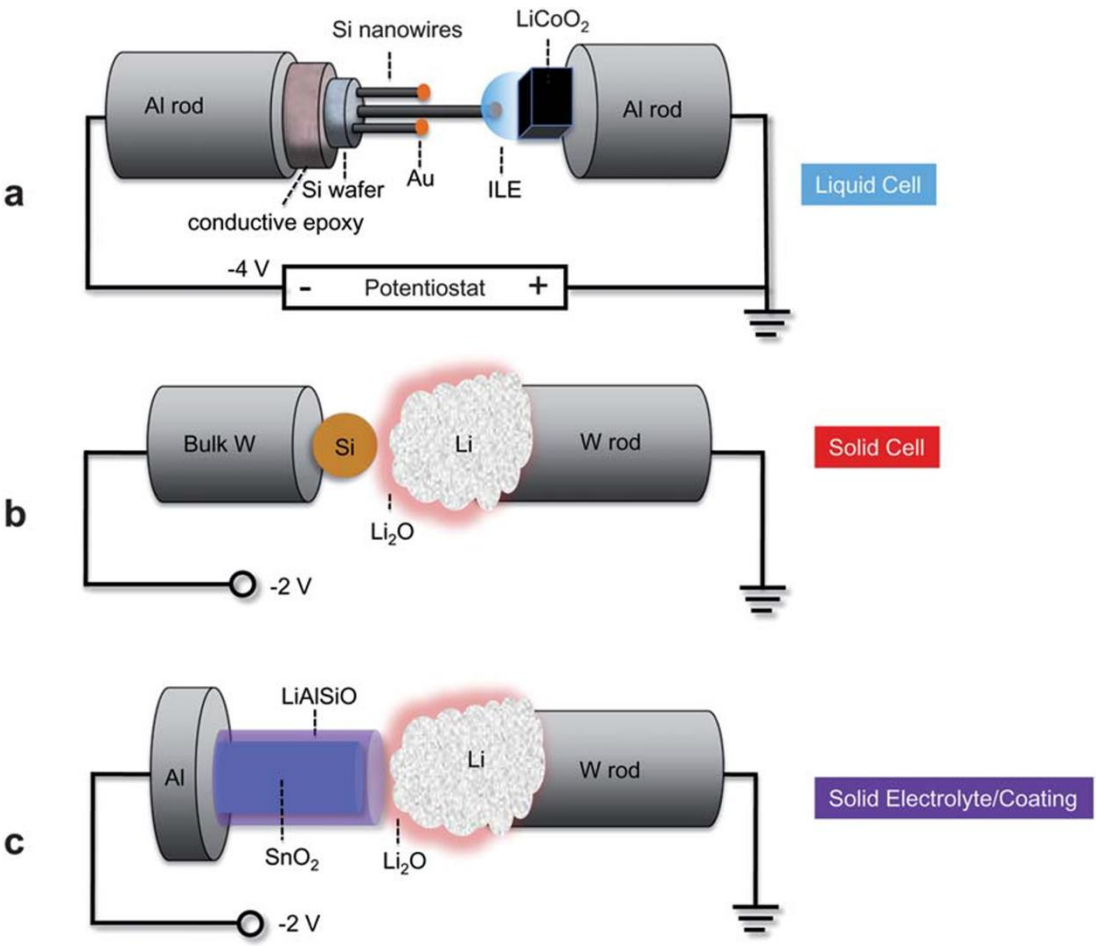

Figure 1.15. Schematics of in situ TEM set ups for electrochemical experiments. Reproduced from Liu et al. (2011).[62]

Liu et al. utilised the set-up from Figure 1.15 (a) to investigate the mechanism of lithiation of Si NWs.[63] It was found that the rate of lithiation in the growth direction

was negligible but radial lithiation was observed at a rate of approximately 3.9 nm min^{-1}. This resulted in a core-shell structure produced during lithiation (Figure 1.16). HRTEM images of the Si facets at an early stage of lithiation revealed a ledge mechanism which occurs due to reactivity differences in different crystal orientations. A noticeable change which occurs in the nanowire is the amorphisation due to lithiation and an increase in the diameter of the NW.

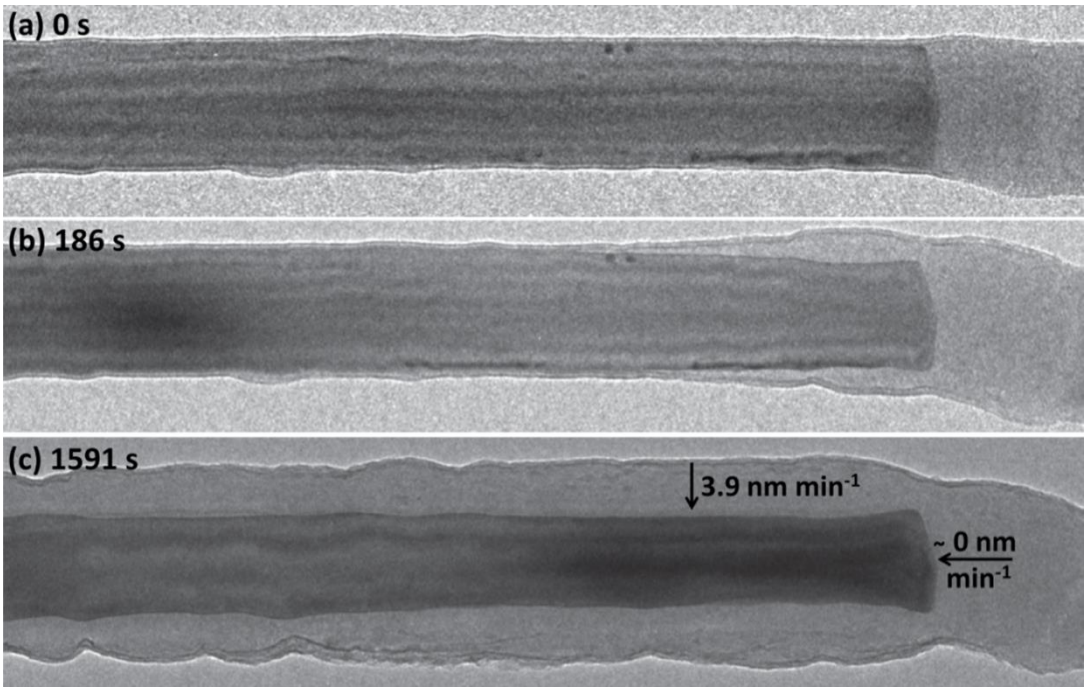

Figure 1.16. (a) Partially lithiated <111> orientated Si NW. (b) Same Si NW under conventional lithiation conditions at a potential of 22 V at 186 s. (c) Core-shell structure produced due to radial lithiation at 1591 s. Reproduced from Liu et al. (2011).[63]

Liu et al. extended the lithiation experiments to other materials such as Ge.[64] A similar observation was reported whereby amorphisation occurred during lithiation along with the increase in NW diameter. A further step was taken and multiple lithiation/delithiation steps were performed, which would mimic the performance of a NW based Li ion battery as it is charged and discharged. It was found that pore formation occurred in the NW after just the first delithiation. The pore formation resulted in sponge-like NWs consisting of amorphous Ge connections. Images of a

Ge NW which underwent four reversible lithiation/delithiation cycles is shown in Figure 1.17. After lithiation, the NW appears thicker and showed crystalline contrast. After delithiation, the NW became porous and amorphous.

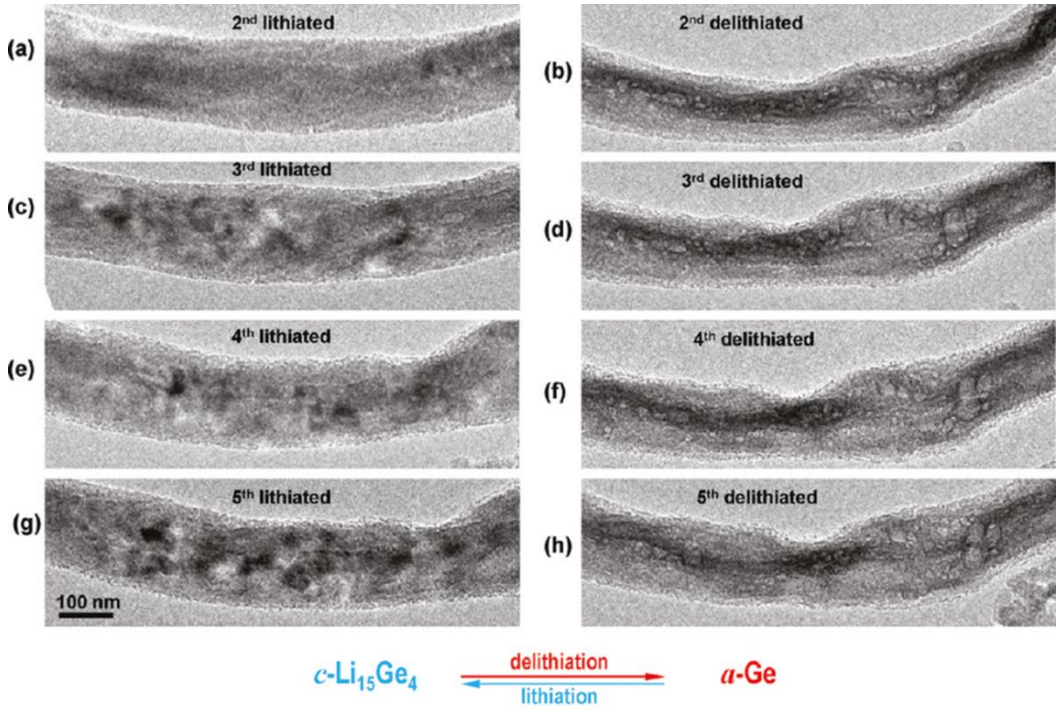

Figure 1.17. Evolution of a Ge NW during lithiation/delithiation cycles. (a-h) Four reversible sequential lithiation/delithiation cycles are shown. Reproduced from Liu et al. (2011).[64]

Gu et al. investigated the effect of bending a Ge NW during lithiation and found that a non-symmetric lithiation of the NW occurs.[65] At the tensile side an increase in lithiation rate was observed while at the compressed side there was a decrease in the lithiation rate (Figure 1.18). The results obtained from the in situ TEM experiments were coupled with 3D chemomechanical modelling which shows a strong agreement with experimental results of stress dependant Li diffusion and reaction rate during lithiation.

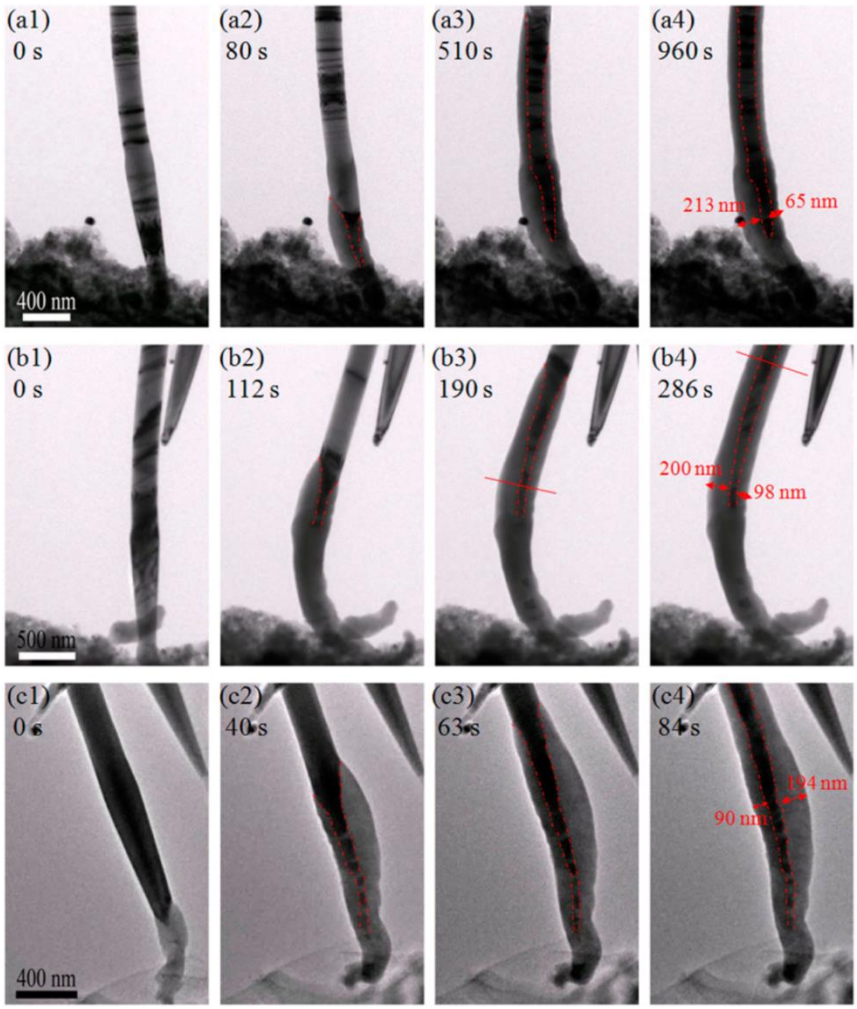

Figure 1.18. Images acquired during the lithiation of three different Ge NWs. The NWs were bent by pushing them against the Li metal. The remaining Ge core which did not undergo lithiation is identified with the red dashed outlines. Reproduced from Gu et al. (2014).[65]

1.8. Strain

An in depth review by Hÿtch and Minor presents an overview for more background on the in situ TEM technique for investigating strain in nanostructures.[66] The review presents summary of sample preparation, imaging methods and examples of strain experiments results. Wang et al. investigated the mechanical properties of lithiated Si in situ.[67] The results highlight the difference between crystalline Si and lithiated Si. The <111> grown Si nanowire is partially lithiated in an electrochemical cell

assembly so that the core remains unlithiated and hence pristine. After the electrochemical lithiation, the NW was compressed using the Li probe. Crystalline Si is brittle and lithiated Si is ductile and will undergo a large deformation, as shown in Figure 1.19. The fracture strength of the c-Si core was estimated to be 7.7 GPa. In contrast to the abrupt fracture of the crystalline core, the amorphous lithiated Si shell did not show any sign of cracking exhibiting a high damage tolerance.

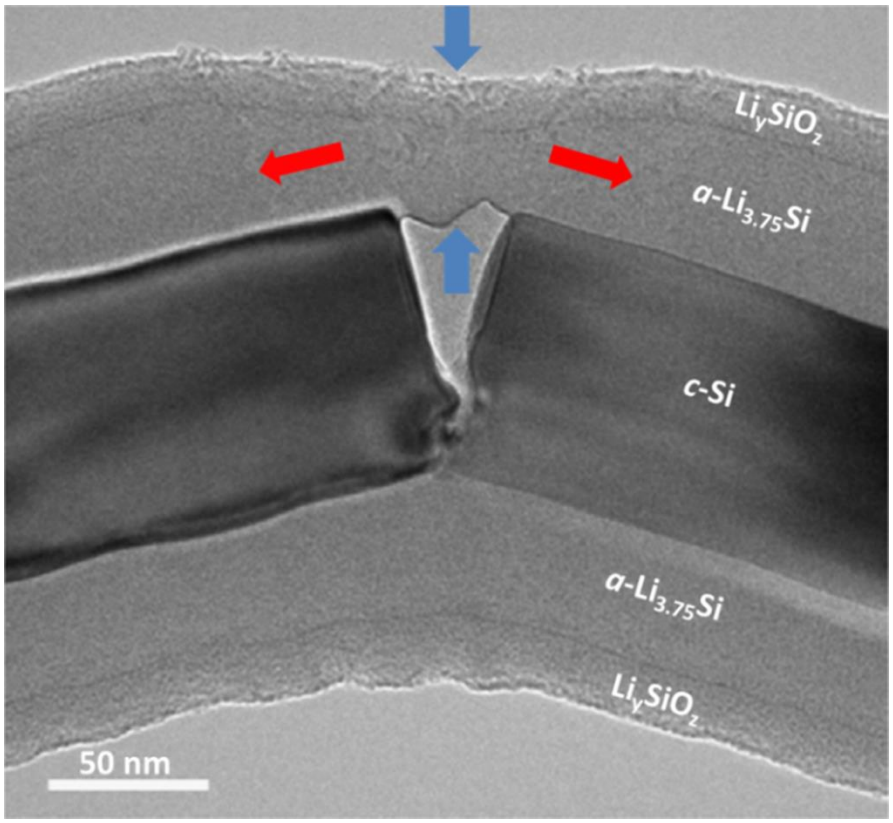

Figure 1.19. Brittle facture of the c-Si (unlithiated) core and the tensile deformation (red arrows) and lateral thinning (blue arrows) of the lithiated Si shell. Reproduced from Wang et al. (2015).[67]

As shown above by Gu et al.,[65] applied external stress can alter a process within a NW. Tang et al. studied the mechanical properties of Si NWs by in situ TEM.[68] NWs down to a diameter of approximately 9 nm were subjected to uniaxial tension and bending. It was found that the diameter of the NW greatly affects its mechanical

behaviour under stress. The Si NWs showed elastic deformation followed by abrupt fractures under tension. Nucleation of cracks was observed on areas of large strain on the tensed side of the NW. On the compressed side plastic deformation, due to dislocations and amorphisation, was observed, as shown in Figure 1.20.

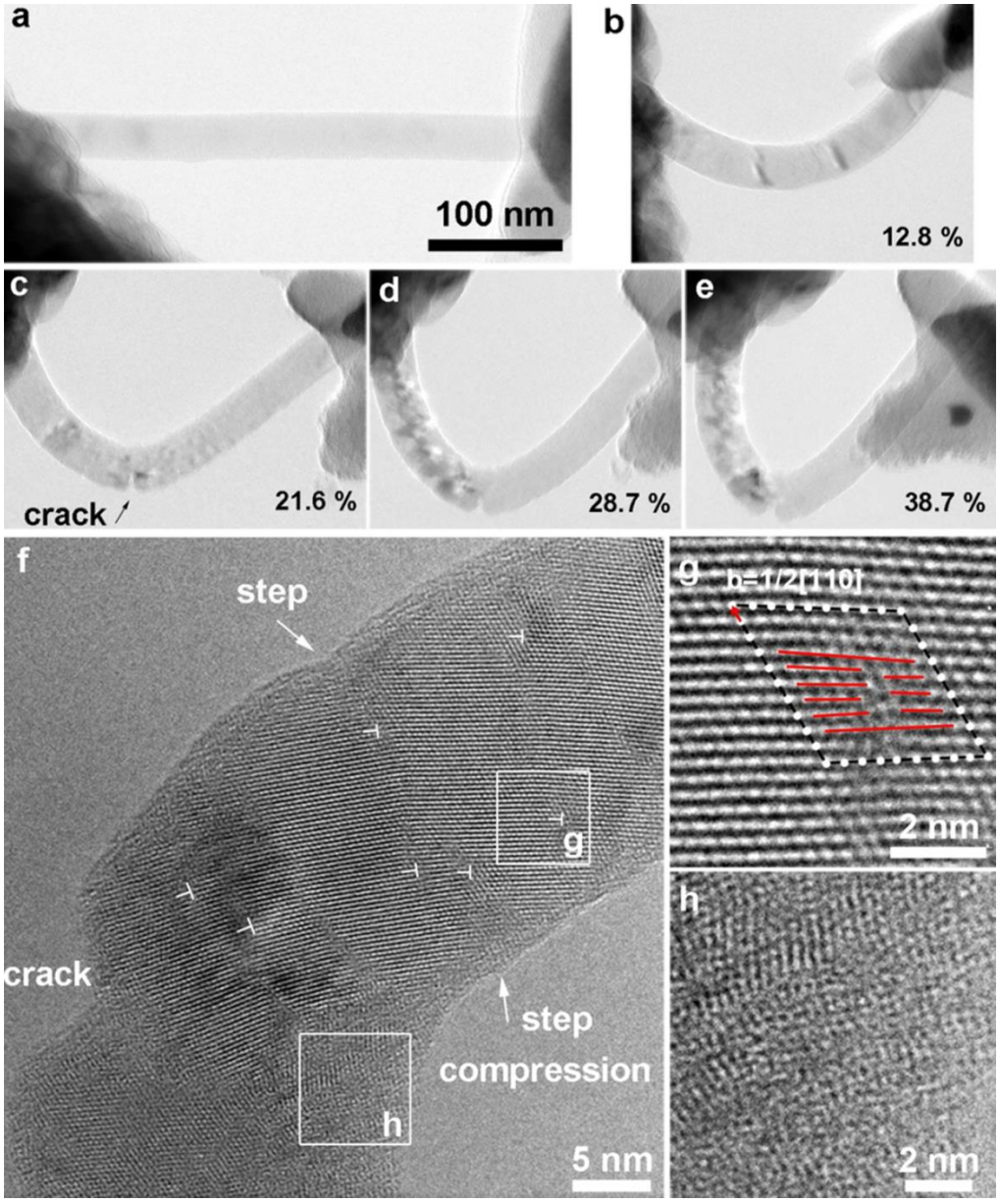

Figure 1.20. Images acquired from in situ bending of a Si NW (25.3 nm diameter). (a – e) Images from the bending show crack formation and propagation during bending. (f) HRTEM of the Si NW with highlighted areas (g) where dislocation and (h) amorphisation is observed. Reproduced from Tang et al. (2012).[68]

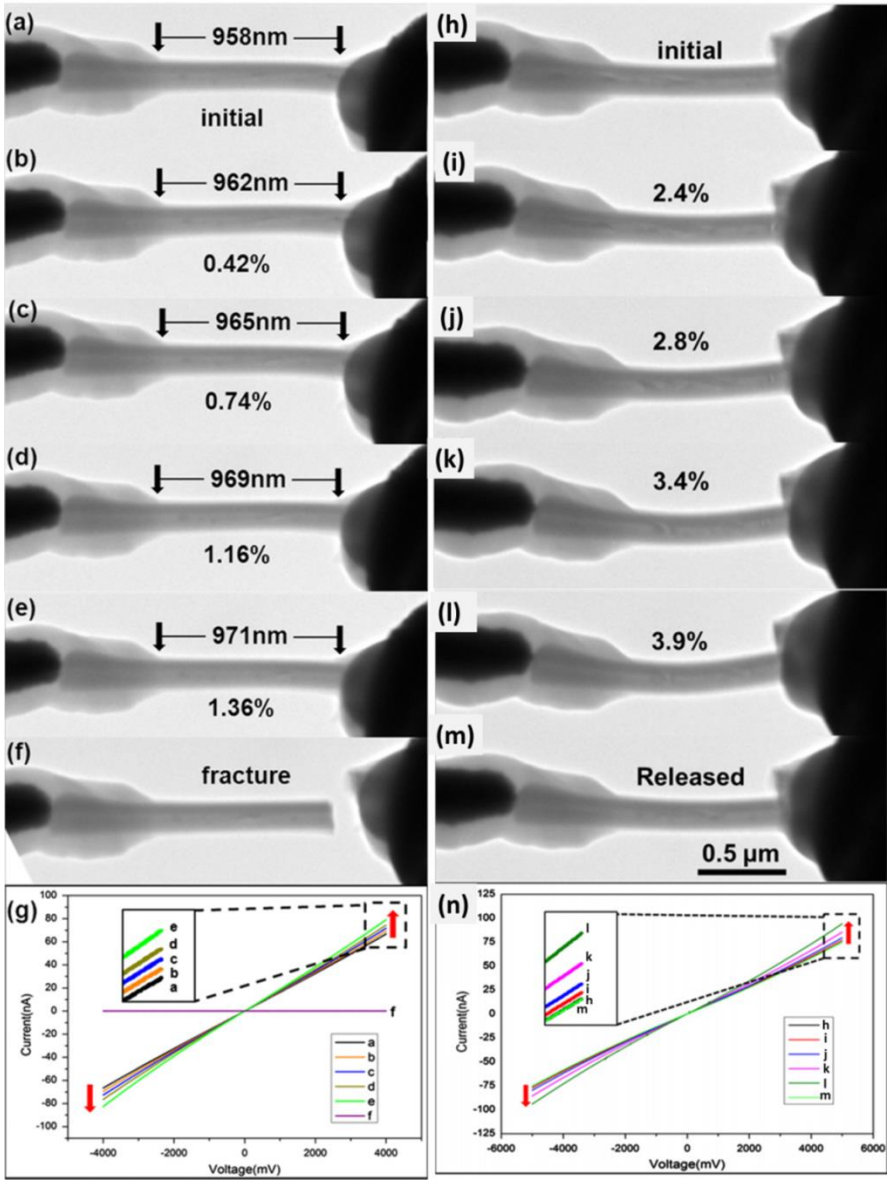

Figure 1.21. (a-e) Images of Si NW under applied tensile strain. (f) The Si NW after fracture. (g) The IV curves for the corresponding images (a-f). (h-l) Images of Si NW undergoing bending strain. (m) Si NW released after the bending strain. (n) The IV curves for the corresponding image images (h-m). Reproduced from Shao et al. (2015).[69]

An enhancement in in carrier transport properties was observed under uniaxial tensile and bending strain in Si NWs performed in situ in a TEM utilising an STM-TEM probing system.[69] The experimental set up consisted of a piezo driven tungsten (W) tip and a silver (Ag) electrode, between which the NW is bonded by electron beam induced deposition (EBID). The NW could be strained by the accurate control of the piezo-motor. Images from two separate experiments are presented in Figure

1.21; (a-g) tensile strain and (h-n) bending strain. The images of the NW in Figure 1.21 (a-g) show the effect of compressive strain on the electrical properties of the Si NW. The NW length could be accurately measured to confirm the type of strain being imposed on the NW. The same case for the bending strain, the in situ images acquired (Figure 1.21 h-m) confirm the type of strain experienced by the NW. In both, tensile and bending strain experiments, the slope of the IV curve increased indicating an improvement in the conductance of the NW. The coupling of the electrical characterisation with induced strain in experiments illustrates the benefit of dynamic TEM.

1.9. Conclusions

Nanostructures such as nanowires are ideal for TEM as they are already at electron transparent dimensions so little/no preparation time is required. TEM sample preparation of bulk samples completely disturbs the sample by introducing additional facets and crystal damage. This is a problem when trying to compare in situ TEM experiments with bulk samples. For this reason in situ TEM of a nanostructure sample is a better representation of the kinetics/mechanism of reactions observed. The knowledge acquired from the in situ experiments described in this chapter is all based on bottom-up (grown) nanowires. From a device perspective in manufacturing, nanowires produced from the top-down methods are more practical. However, grown NWs achieve atomically flat, faceted surfaces which are not easily achieved via lithography processes. The difference between the two different NW fabrication methods could mean that the results highlighted here may differ greatly for a top-down fabricated NW.

Dynamic TEM has been utilised in diverse areas to understand and examine material properties that could further potential applications. The main advantage of in situ TEM experiments is the ability to observe processes as they occur and understand the mechanism and kinetics of the process. The combinations of capabilities within one dynamic TEM holder such as strain and electrical biasing or environmental holders with heating capabilities allow for complex experimentation. The advances in dynamic TEM holder technologies and state of the art aberration corrected TEMs with monochromators have opened up the ability to perform lattice/atomic-resolution experiments.

1.10. References

1 Oh, J. & Campbell, J. C. Thermal desorption of Ge native oxides and the loss of Ge from the surface. *J. Electron. Mater.* 33, 364-367, doi:10.1007/s11664-004-0144-4 (2004).

2 Wang, S. K., Kita, K., Lee, C. H., Tabata, T., Nishimura, T., Nagashio, K., Toriumi, A. Desorption kinetics of GeO from GeO_2/Ge structure. *J. Appl. Phys.* 108, doi:10.1063/1.3475990 (2010).

3 Delabie, A., Bellenger, F., Houssa, M., Conrad, T., Van Elshocht, S., Caymax, M., Heyns, M., Meuris, M. Effective electrical passivation of Ge(100) for high-κ gate dielectric layers using germanium oxide. *Appl. Phys. Lett.* 91, doi:10.1063/1.2773759 (2007).

4 Kingon, A. I., Maria, J.-P. & Streiffer, S. K. Alternative dielectrics to silicon dioxide for memory and logic devices. *Nature* 406, 1032-1038 (2000).

5 Lu, W., Xie, P. & Lieber, C. M. Nanowire transistor performance limits and applications. *IEEE Trans. Electon. Dev.* 55, 2859-2876, doi:10.1109/ted.2008.2005158 (2008).

6 Lieber, C. M. One-dimensional nanostructures: Chemistry, physics & applications. *Solid State Commun.* 107, 607-616, doi:10.1016/S0038-1098(98)00209-9 (1998).

7 Hu, J., Odom, T. W. & Lieber, C. M. Chemistry and physics in one dimension: Synthesis and properties of nanowires and nanotubes. *Acc. Chem. Res.* 32, 435-445, doi:10.1021/ar9700365 (1999).

8 Hobbs, R. G., Petkov, N. & Holmes, J. D. Semiconductor nanowire fabrication by bottom-up and top-down paradigms. *Chem. Mater.* 24, 1975-1991, doi:10.1021/cm300570n (2012).

9 Fan, H. J., Werner, P. & Zacharias, M. Semiconductor nanowires: From self-organization to patterned growth. *Small* 2, 700-717, doi:10.1002/smll.200500495 (2006).

10 Wang, N., Cai, Y. & Zhang, R. Q. Growth of nanowires. *Mater. Sci. Eng. R-Rep.* 60, 1-51, doi:10.1016/j.mser.2008.01.001 (2008).

11 Ramanujam, J., Shiri, D. & Verma, A. Silicon nanowire growth and properties: A Review. *Mater. Express* 1, 105-126, doi:10.1166/mex.2011.1013 (2011).

12 Zhou, W., Oxley, M. P., Lupini, A. R., Krivanek, O. L., Pennycook, S. J., Idrobo, J.-C. Single atom microscopy. *Microsc. Microanal.* 18, 1342-1354, doi:10.1017/S1431927612013335 (2012).

13 Minor, A. M., Lilleodden, E. T., Stach, E. A. & Morris, J. W., Jr. In-situ transmission electron microscopy study of the nanoindentation behavior of Al. *J. Electron. Mater.* 31, 958-964, doi:10.1007/s11664-002-0028-4 (2002).

14 de Jonge, N. & Ross, F. M. Electron microscopy of specimens in liquid. *Nat. Nanotechnol.* 6, 695-704, doi:10.1038/nnano.2011.161 (2011).

15 De Graef, M. Recent progress in Lorentz transmission electron microscopy. *Esomat 2009 - 8th European Symposium on Martensitic Transformations*, doi:10.1051/esomat/200901002 (2009).

16 LaGrange, T., Armstrong, M. K., Boyden, K., Brown, C. G., Campbell, G. H., Colvin, J. D., DeHope, W. J., Frank, A. M., Gibson, D. J., Hartemann, F. V., Kim, J. S., King, W. E., Pyke, B. J., Reed, B. W., Shirk, M. D., Shuttlesworth, R. M., Stuart, B. C., Torralva, B. R., Browning, N. D. Single-shot dynamic transmission electron microscopy. *Appl. Phys. Lett.* 89, 044105, doi:10.1063/1.2236263 (2006).

17 Kim, J. S., LaGrange, T., Reed, B. W., Taheri, M. L., Armstrong, M. R., King, W. E., Browning, N. D., Campbell, G. H. Imaging of transient structures using nanosecond in situ TEM. *Science* 321, 1472-1475, doi:10.1126/science.1161517 (2008).

18 Bostanjoglo, O., Elschner, R., Mao, Z., Nink, T. & Weingärtner, M. Nanosecond electron microscopes. *Ultramicroscopy* 81, 141-147, doi:10.1016/S0304-3991(99)00180-1 (2000).

19 Plemmons, D. A., Park, S. T., Zewail, A. H. & Flannigan, D. J. Characterization of fast photoelectron packets in weak and strong laser fields in ultrafast electron microscopy. *Ultramicroscopy* 146, 97-102, doi:10.1016/j.ultramic.2014.08.001 (2014).

20 Ross, F. M. Controlling nanowire structures through real time growth studies. *Rep. Prog. Phys.* 73, doi:10.1088/0034-4885/73/11/114501 (2010).

21 Hammar, M., LeGoues, F. K., Tersoff, J., Reuter, M. C. & Tromp, R. M. In situ ultrahigh vacuum transmission electron microscopy studies of hetero-

epitaxial growth .1. Si(001)/Ge. *Surf. Sci.* 349, 129-144, doi:10.1016/0039-6028(95)01068-8 (1996).

22 Hannon, J. B., Kodambaka, S., Ross, F. M. & Tromp, R. M. The influence of the surface migration of gold on the growth of silicon nanowires. *Nature* 440, 69-71, doi:10.1038/nature04574 (2006).

23 Kodambaka, S., Hannon, J. B., Tromp, R. M. & Ross, F. M. Control of Si nanowire growth by oxygen. *Nano Lett.* 6, 1292-1296, doi:10.1021/nl060059p (2006).

24 Hillerich, K., Dick, K. A., Wen, C. Y., Reuter, M. C., Kodambaka, S., Ross, F. M. Strategies to control morphology in hybrid group III-V/group IV heterostructure nanowires. *Nano Lett.* 13, 903-908, doi:10.1021/nl303660h (2013).

25 Holmberg, V. C., Panthani, M. G. & Korgel, B. A. Phase transitions, melting dynamics, and solid-state diffusion in a nano test tube. *Science* 326, 405-407, doi:10.1126/science.1178179 (2009).

26 Sharma, R. Kinetic measurements from in situ TEM observations. *Microsc. Res. Tech.* 72, 144-152, doi:10.1002/jemt.20667 (2009).

27 Biswas, S., O'Regan, C., Morris, M. A., Holmes, J. D. In-situ observations of nanoscale effects in germanium nanowire growth with ternary eutectic alloys. *Small* 11, 103-111, doi:10.1002/smll.201401240 (2015).

28 O'Regan, C., Biswas, S., O'Kelly, C., Jung, S. J., Boland, J. J., Petkov, N., Holmes, J. D. Engineering the growth of germanium nanowires by tuning the supersaturation of Au/Ge binary alloy catalysts. *Chem. Mater.* 25, 3096-3104, doi:10.1021/cm401281y (2013).

29 Taheri, M. L., Reed, B. W., LaGrange, T. B., Browning, N. D. In situ laser synthesis of Si nanowires in the dynamic TEM. *Small* 4, 2187-2190, doi:10.1002/smll.200800588 (2008).

30 Lotty, O., Hobbs, R., O'Regan, C., Hlina, J., Marschner, C., O'Dwyer, C., Petkov, N., Holmes, J. D. Self-seeded growth of germanium nanowires: Coalescence and Ostwald ripening. *Chem. Mater.* 25, 215-222, doi:10.1021/cm3032863 (2013).

31 Halder, A. & Ravishankar, N. Ultrafine single-crystalline gold nanowire arrays by orientated attachment. *Adv. Mater.* 19, 1854-1858, doi:10.1002/adma.200602325 (2007).

32 Hobbs, R. G., Barth, S., Petkov, N., Zirngast, M., Marschner, C., Morris, M. A., Holmes, J. D. Seedless growth of sub-10 nm germanium nanowires. *J. Am. Chem. Soc.* 132, 13742-13749, doi:10.1021/ja1035368 (2010).

33 Shayesteh, M., Huet, K., Toque-Tresonne, I., Negru, R., Daunt, C. L. M., Kelly, N., O'Connell, D., Yu, R., Djara, V., Carolan, P. B., Petkov, N., Duffy, R. Atomically flat low-resistive germanide contacts formed by laser thermal anneal. *IEEE Trans. Electron Dev.* 60, 2178-2185, doi:10.1109/ted.2013.2263336 (2013).

34 Nash, A. & Nash, P. The Ge−Ni (germanium-nickel) system. *Bull. Alloy Phase Diagrams* 8, 255-264, doi:10.1007/bf02874917 (1987).

35 Chou, Y. C., Wu, W. W., Lee, C. Y., Liu, C. Y., Chen, L. J., Tu, K. N. Heterogeneous and homogeneous nucleation of epitaxial $NiSi_2$ in 110 Si nanowires. *J. Phys. Chem. C* 115, 397-401, doi:10.1021/jp108686y (2011).

36 Walser, R. M. & Bené, R. W. First phase nucleation in silicon–transition-metal planar interfaces. *Appl. Phys. Lett.* 28, 624-625, doi:10.1063/1.88590 (1976).

37 Wittmer, M., Nicolet, M. A. & Mayer, J. W. The first phase to nucleate in planar transition metal-germanium interfaces. *Thin Solid Films* 42, 51-59, doi:10.1016/0040-6090(77)90077-3 (1977).

38 Nath, R., Soo, C. W., Boothroyd, C. B., Yeadon, M., Chi, D. Z., Sun, H. P., Chen, Y. B., Pan, X. Q., Foo, Y. L., NiGe on Ge(001) by reactive deposition epitaxy: An in situ ultrahigh-vacuum transmission-electron microscopy study. *Appl. Phys. Lett.* 86, doi:10.1063/1.1929100 (2005).

39 Deng, Y., Nakatsuka, O., Suzuki, A., Sakashita, M. & Zaima, S. Epitaxial formation of Ni germanide on Ge(001) substrate by reactive deposition. *Solid-State Electron.*, doi:10.1016/j.sse.2015.01.009 (2015).

40 Lee, J. W., Bae, J. H., Hwang, J. H., Kim, H. K., Park, M. H., Kim, H., Yang, C. W. Dynamic study on microstructural evolution of nickel germanide utilizing zirconium interlayer. *Microelectron. Eng.* 89, 23-26, doi:10.1016/j.mee.2011.03.010 (2012).

41 Lee, J.-W., Kim, H.-K., Bae, J.-H., Park, M.-H., Kim, H., Ryu, J., Yang, C.-W. Enhanced morphological and thermal stabilities of nickel germanide with an ultrathin tantalum layer studied by ex situ and in situ transmission electron microscopy. *Microsc. Microanal.* 19, 114-118, doi:10.1017/S1431927613012452 (2013).

42 Lai, H.-Y., Huang, C.-W., Chiu, C.-H., Wang, C.-W., Chen, J.-Y., Huang, Y.-T., Lu, K.-C., Wu, W.-W. Real time observation of the formation of hollow nanostructures through solid state reactions. *Anal. Chem.* 86, 4348-4353, doi:10.1021/ac500134u (2014).

43 Panciera, F., Chou, Y. C., Reuter, M. C., Zakharov, D., Stach, E. A., Hofmann, S., Ross, F. A.Synthesis of nanostructures in nanowires using sequential catalyst reactions. *Nat Mater* 14, 820-825, doi:10.1038/nmat4352 (2015).

44 Watt, F., Bettiol, A. A., van Kan, J. A., Teo, E. J. & Breese, M. B. H. Ion beam lithography and nanofabrication: A review. *Int. J. Nanosci.* 04, 269-286, doi:10.1142/S0219581X05003139 (2005).

45 Cui, Y., Duan, X. F., Hu, J. T. & Lieber, C. M. Doping and electrical transport in silicon nanowires. *J. Phys. Chem. B* 104, 5213-5216, doi:10.1021/jp0009305 (2000).

46 Borschel, C., Niepelt, R., Geburt, S., Gutsche, C., Regolin, I., Prost, W., Tegude, F.-J., Stichtenoth, D., Schwen, D., Ronning, C. Alignment of

semiconductor nanowires using ion beams. *Small* 5, 2576-2580, doi:10.1002/smll.200900562 (2009).

47 Borschel, C., Spindler, S., Lerose, D., Bochmann, A., Christiansen, S. H., Nietzsche, S., Oertel, M., Ronning, C. Permanent bending and alignment of ZnO nanowires. *Nanotechnology* 22, doi:10.1088/0957-4484/22/18/185307 (2011).

48 Bettge, M., MacLaren, S., Burdin, S., Haasch, R. T., Abraham, D., Petrov, I., Yu, M. F., Sammann, E. Ion-induced surface relaxation: controlled bending and alignment of nanowire arrays. *Nanotechnology* 23, doi:10.1088/0957-4484/23/17/175302 (2012).

49 Pecora, E., Irrera, A., Boninelli, S., Romano, L., Spinella, C., Priolo, F. Nanoscale amorphization, bending and recrystallization in silicon nanowires. *Appl. Phys. A* 102, 13-19, doi:10.1007/s00339-010-6040-2 (2011).

50 Jun, K., Joo, J. & Jacobson, J. M. Focused ion beam-assisted bending of silicon nanowires for complex three dimensional structures. *J. Vac. Sci. Technol., B* 27, 3043-3047, doi:10.1116/1.3259919 (2009).

51 Romano, L., Rudawski, N. G., Holzworth, M. R., Jones, K. S., Choi, S. G., Picraux, S. T. Nanoscale manipulation of Ge nanowires by ion irradiation. *J. Appl. Phys.* 106, doi:10.1063/1.3267154 (2009).

52 Duffy, R., Shayesteh, M., McCarthy, B., Blake, A., White, M., Scully, J., Yu, R., Kelleher, A. M., Schmidt, M., Petkov, N., Pelaz, L., Marques, L. A. The curious case of thin-body Ge crystallization. *Appl. Phys. Lett.* 99, doi:10.1063/1.3643160 (2011).

53 Hinks, J. A. Transmission electron microscopy with in situ ion irradiation. *J. Mater. Res.* 30, 1214-1221, doi:10.1557/jmr.2014.384 (2015).

54 Hattar, K., Bufford, D. C. & Buller, D. L. Concurrent in situ ion irradiation transmission electron microscope. *Nucl. Instrum. Meth. B* 338, 56-65, doi:10.1016/j.nimb.2014.08.002 (2014).

55 Fedina, L. I., Song, S. A., Chuvilin, A. L., Gutakovskii, A. K. & Latyshev, A. V. The mechanism of {113} defect formation in silicon: clustering of interstitial-vacancy pairs studied by in situ high-resolution electron microscope irradiation. *Microsc. Microanal.* 19, 38-42, doi:10.1017/s1431927613012294 (2013).

56 Vanhellemont, J., Anada, S., Nagase, T., Yasuda, H., Bender, H., Rooyackers, R., Vandooren, A. In situ UHVEM irradiation study of intrinsic point defect behavior in Si nanowire structures. *Phys. Stat. Solidi C*, doi:10.1002/pssc.201400100 (2015).

57 Gobulukoglu, I. & Robertson, B. W., In situ STEM technique for characterization of nanoscale interconnects during electromigration testing, *Materials Reliability in Microelectronics Ix* Vol. 563 *Materials Research Society Symposium Proceedings*, 181-186, (1999).

58 Hummelgard, M., Zhang, R. Y., Carlberg, T., Vengust, D., Dvorsek, D., Mihailovic, D., Olin, H. Nanowire transformation and annealing by Joule heating. *Nanotechnology* 21, doi:10.1088/0957-4484/21/16/165704 (2010).

59 Lei, A., Peterson, D. H., Booth, T. J., Homann, L. V., Kallesoe, C., Sukas, O. S., Gyrsting, Y., Molhave, K., Boggild, P. Customizable in situ TEM devices fabricated in freestanding membranes by focused ion beam milling. *Nanotechnology* 21, doi:10.1088/0957-4484/21/40/405304 (2010).

60 Kallesoe, C., Wen, C. Y., Booth, T. J., Hansen, O., Boggild, P., Ross, F. M., Molhave, K. In situ TEM creation and electrical characterization of nanowire devices. *Nano Lett.* 12, 2965-2970, doi:10.1021/nl300704u (2012).

61 Westenfelder, B., Meyer, J. C., Biskupek, J., Algara-Siller, G., Lechner, L. G., Kusterer, J., Kaiser, U., Krill, C. E., Kohn, E., Scholz, F. Graphene-based sample supports for in situ high-resolution TEM electrical investigations. *J. Phys. D Appl. Phys.* 44, doi:10.1088/0022-3727/44/5/055502 (2011).

62 Liu, X. H. & Huang, J. Y. In situ TEM electrochemistry of anode materials in lithium ion batteries. *Energy Environ. Sci.* **4**, 3844-3860, doi:10.1039/c1ee01918j (2011).

63 Liu, X. H., Wang, J. W., Huang, S., Fan, F., Huang, X., Liu, Y., Krylyuk, S., Yoo, J., Dayeh, S. A., Davydov, A. V., Mao, S. X., Picraux, S. T., Zhang, S., Li, J., Zhu, T., Huang, J. Y. In situ atomic-scale imaging of electrochemical lithiation in silicon. *Nat. Nanotechnol.* **7**, 749-756, doi:10.1038/nnano.2012.170 (2012).

64 Liu, X. H., Huang, S., Picraux, S. T., Li, J., Zhu, T., Huang, J. Y. Reversible nanopore formation in Ge nanowires during lithiation-delithiation cycling: An in situ transmission electron microscopy Study. *Nano Lett.* **11**, 3991-3997, doi:10.1021/nl2024118 (2011).

65 Gu, M., Yang, H., Perea, D. E., Zhang, J. G., Zhang, S. L., Wang, C. M. Bending-induced symmetry breaking of lithiation in germanium nanowires. *Nano Lett.* **14**, 4622-4627, doi:10.1021/nl501680w (2014).

66 Hytch, M. J. & Minor, A. M. Observing and measuring strain in nanostructures and devices with transmission electron microscopy. *MRS Bull.* **39**, 138-146, doi:10.1557/mrs.2014.4 (2014).

67 Wang, X., Fan, F., Wang, J., Wang, H., Tao, S., Yang, A., Liu, Y., Beng Chew, H., Mao, S. X., Zhu, T., Xia, S. High damage tolerance of electrochemically lithiated silicon. *Nat. Commun.* **6**, doi:10.1038/ncomms9417 (2015).

68 Tang, D.-M., Ren, C.-L., Wang, M.-S., Wei, X., Kawamoto, N., Liu, C., Bando, Y., Mitome, M., Fukata, N., Golberg, D. Mechanical properties of Si nanowires as revealed by in situ transmission electron microscopy and molecular dynamics simulations. *Nano Lett.* **12**, 1898-1904, doi:10.1021/nl204282y (2012).

69 Shao, R. W., Gao, P. & Zheng, K. The effect of tensile and bending strain on the electrical properties of p-type < 110 > silicon nanowires. *Nanotechnology* **26**, doi:10.1088/0957-4484/26/26/265703 (2015).

Chapter 2

Experimental Methods

2.1. Instrumentation

An FEI Helios 600i NanoLab dual beam system (SEM/FIB) was used for all SEM imaging, ion irradiations and TEM lamellae sample preparation. The SEM is equipped with a FEG (field emission gun) source and the FIB with a Ga LMIS (liquid metal ion source). An omniprobe needle facilitates TEM lamella preparation.

A JEOL 2100, LaB_6 filament source, TEM was used for all TEM imaging. For HRTEM, a Gatan double tilt holder was used to allow tilt in two axes which facilitates tilting a crystal to a zone axis. For heating experiments, a Gatan 628 single tilt heating stage holder was used. The stage operates as a micro furnace and is capable of temperatures of 1000 °C but a maximum temperature of 500 °C was used in this thesis. Temperature was controlled using a Gatan Model 901 SmartSet hot stage controller. The temperature dispersion control is approximately 0.1−0.5 °C, as per the manufacturer's specifications.

A Raith eLine EBL system was used for all EBL exposures. The system is a converted SEM with a laser stage which allows for accurate movement of the stage for patterning.

2.2. Nanowire Fabrication

Two types of nanowires were used in this thesis; grown (bottom up) and GeOI lithography defined (top-down) nanowires.

2.2.1. Grown Nanowires

The grown nanowires were supplied by Dr Subhajit Biswas, Dr Olan Lotty and Dr Colm O'Regan. A SCF (supercritical fluid) method of synthesis for the grown Ge NWs was used which occurs via a VLS-type (vapour-liquid-solid) mechanism.[1-4] The nanowires are grown on Si substrates with a dispersion of Au nanoparticles which act as the seed for growth. The grown nanowires appear like a forest of nanowires on the substrate. Typically, nanowires are removed from the substrate by sonication in isopropyl alcohol (IPA) to produce a suspension of nanowires. This introduces organic solvent contamination and which can be difficult to remove, leaving residue and diminishing the ability of HRTEM. To avoid this, a dry transfer method was used in this work. A scalpel was used to gently remove some NWs from the substrate and transfer to the sample platform, e.g. the SiN membrane.

2.2.2. Lithography defined fabricated nanowires

The lithography defined Ge NWs are fabricated from GeOI substrates using HSQ (hydrogen silsesquioxane) resist in a Raith eLine EBL system by Dr Anushka Gangnaik.[5] All GeOI NWs were defined via EBL from a (001) GeOI wafer along the [100] direction. HSQ is a high resolution negative tone resist which when exposed to the electron beam, becomes insoluble to the developer solution, TMAH (tetramethylammonium hydroxide). As Ge reoxidises rapidly in ambient conditions, a citric acid clean was used to remove the oxide and passivate the surface prior to HSQ resist deposition.[6] A 2.4% HSQ (in methyl isobutyl ketone) solution was deposited directly after the oxide removal step via spin coating at 2000rpm for 33s.[5] The resist film was baked on a hotplate at 120 °C for 3 min, to remove any solvent from the resist. The EBL was operated at 10 kV and exposure doses were set

depending on the NW diameter desired; 1000 μCcm^{-2} for 1 m diameter and 2300 μCcm^{-2} for 20 nm diameter. Essentially, the HSQ forms a SiO_2 mask which can be used as a hard mask for etching. After EBL exposure, the sample was immersed, with agitation, in 2.3% TMAH at room temperature for 70 s, followed by a 30 s rinse in deionised water and then dried in flowing nitrogen for 10 s. The exposed Ge was etched, as described by Ran et al., in a Cl_2 RIE at 80W, 10mTorr, with a flow rate of 30 sccm, for 25 s.[7]

2.3. Nanowire Irradiation via FIB

2.3.1. Concurrent imaging platform for grown nanowires

Grown NWs were transferred to a modified SiN membrane carrier chip platform for concurrent TEM imaging and FIB irradiation. The carrier chip platform used for step-wise implantation/imaging of a specific nanowire is shown in Figure 2.1. Si chips with silicon nitride (SiN) membrane windows were used (Ted Pella), which were patterned using the FIB to label and open slits in the membrane. The patterning is of benefit for two reasons; the slits allow high resolution imaging of sections of the nanowire as well as facile navigation to locate the same nanowire. The parameters for patterning were: 7 lines 10 μm apart, 70 μm long and 0.5 μm wide for a nominal depth of 300 nm with the Ga ion beam operating at 30 kV, 3 nA.

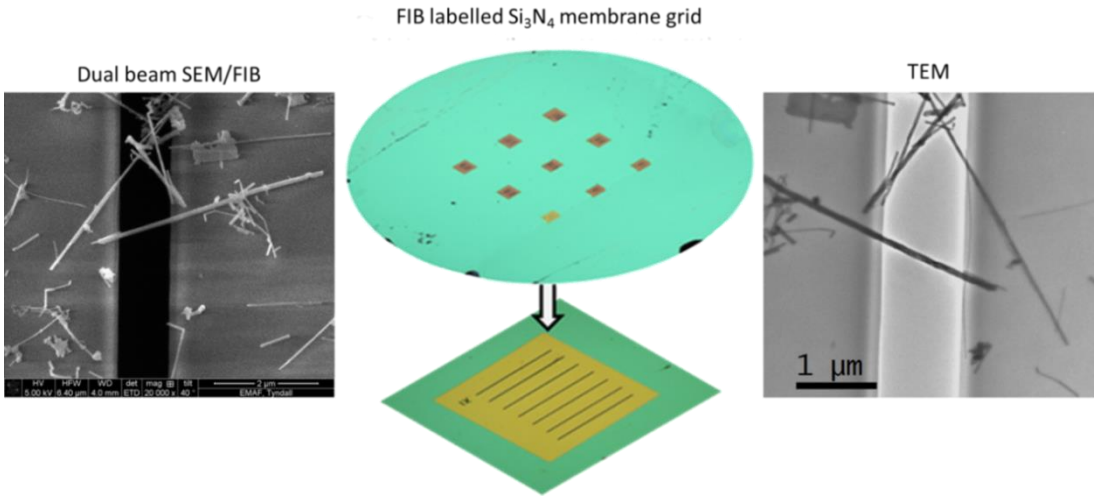

Figure 2.1. Overview of platform for correlative imaging of nanowire on Si_3N_4 membrane grid.

2.3.2. Irradiation of grown nanowires

The grown NWs were first imaged in the TEM where the growth direction, tilt to achieve a low index zone axis and any intrinsic defects were identified. Nanowires that required no more than 10 degrees tilting in one direction, preferably along or perpendicular to their long axis, and fully crossed the opening were selected. The mounting of the membrane chips to the TEM holder was done with the aid of an optical microscope, ensuring the grid is mounted with a fixed orientation. This allows the nanowires to be imaged in the same orientation after each exposure. This accurate mounting method becomes more important as the nanowire reaches a near/fully amorphous state. The grid was then transferred to the SEM/FIB for implantation. All NW irradiation was done using an FEI Helios 600i NanoLab Dual Beam system. The nanowire was located using the SEM and then orientated (stage was rotated and moved in x- and y-directions) so that the nanowire length was at eucentric height when the stage was tilted, i.e. the nanowire was aligned left to right in the SEM. The stage was tilted to 52° so the FIB is normal to the substrate surface.

The position of the NW was saved. The arrow keys, left or right to keep the changing only the y-coordinate, were used to navigate to the edge of the sample. This is to find a safe area away from the NW to align the SEM with the FIB. A feature was identified, without changing the x-coordinate, in the SEM and using beam shift for the ion beam (at 30 kV, 9.7 pA or 5 kV, 10 pA) the same feature was centred. Moving stepwise (one or two clicks of the left/right arrow) back to the NW to be irradiated the alignment was adjusted/checked at increasing magnification to ensure the alignment between SEM and FIB was accurate. Once the NW was within view in the SEM, imaging with the FIB was stopped. Any imaging with the FIB would introduce Ga^+ ions at an unknown dose. With the SEM only, the NW was centred. Assuming accurate alignment with the FIB, the NW should be in the centre of the FIB screen also. The irradiation needs to be done "blind".

Most exposures were done at this tilt unless the tilt required for a nanowire in the TEM is <2°, in this case the stage was tilted to 45° to avoid ion channelling. The pattern for implantation was defined in the ion beam window as a rectangle set to Si mill application: 10 × 10 μm^2 area, 125 ns dwell time, 1 pass and with a total time of 0.316 s to achieve a dose of 1.9 × 10^{13} ions cm^{-2}, operating at 30 kV (or 5 kV), 9.7pA (10pA aperture at 5kV). For partial irradiation of a NW along its length, a 0.5 × 5 μm^2 box was defined, to irradiate a 0.5 μm length section of the NW. The dose was calculated using

$$dose = \frac{I_{ion} \times t_{exposure}}{A_{pattern} \times 1.602 \times 10^{-15}}$$

where I_{ion} is the current/aperture used in pA (9.7 or 10 pA), $t_{exposure}$ is the time of the exposure in seconds (0.316 s) and $A_{pattern}$ is the area of the pattern (100 μm^2). Higher doses were achieved by increasing the number of passes.

The carrier chip was then transferred back to the TEM in the same orientation to image the nanowire after doping. The concurrent implantation/imaging steps were repeated multiple times to build up the step-wise increase in the dose. The maximum implantation dose in our studies was 1.14×10^{14} ions cm^{-2} which corresponds to 6 successive steps. Once the exposure of NWs deposited on SiN membrane grids with trenches was completed, the sample could be directly transferred to the TEM for imaging and even undergo further irradiation.

2.3.3. Irradiation of EBL defined GeOI Nanowires

The method of Ga^+ ion irradiation for grown and lithography defined NWs is nearly identical to grown nanowires, the main difference is how we observe the irradiation damage post anneal and the limitation of only one irradiation event. An overview of the experimental procedure for the irradiation and imaging of NWs is depicted in a schematic in Figure 2.2. NWs deposited on silicon nitride (SiN) membranes do not require any additional steps for observing the damage incurred and subsequent in situ TEM annealing (Figure 2.2 a).[8] The method described in this section is used for grown NWs deposited on a Si/SiO_2 chip via dry transfer from the growth substrate or EBL defined NWs on GeOI (germanium on insulator). In order to observe irradiation damage and in situ TEM recrystallization along the NWs on substrates, the structures need to be extracted with the underlying substrate (Figure 2.2 b iii). This is done via a non-typical inline FIB lift-out technique along the NW length (Figure 2.2 b, Figure 2.3). For all NWs imaged on SiN membranes, the direction of the ion beam (red

arrow) during irradiation is nearly parallel to the electron beam (purple arrow) when imaged in the TEM (Figure 2.2 a). However, for NWs extracted from a substrate (Figure 2.2 b) the direction of the ion beam is orthogonal to the direction of the electron beam when imaged in the TEM, i.e. we have a side view of the irradiated NW along its length.

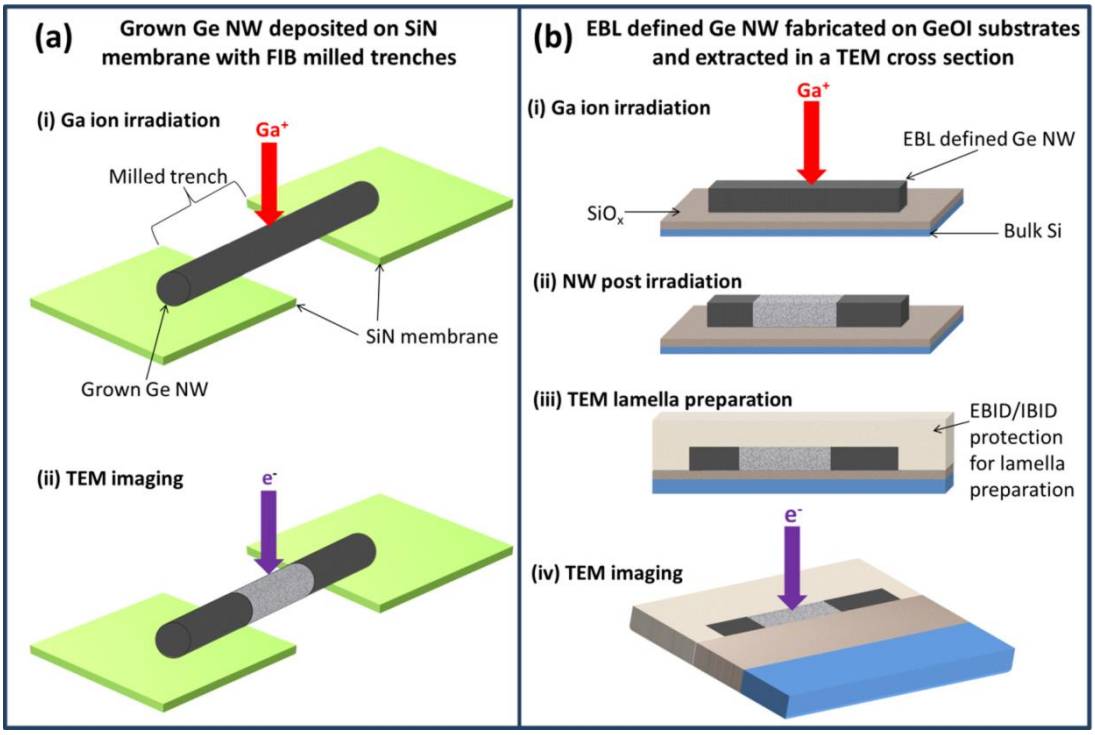

Figure 2.2. Schematic overview of sample preparation and imaging for (a) a nanowire on pre-patterned SiN membrane and (b) EBL defined NW from on GeOI substrate.

The GeOI NWs defined by EBL have a height of approximately 50 nm, which is almost twice the range of interactions of the 30 kV Ga-ions in Ge. Therefore, to achieve amorphisation across the NW (the width of the NWs is approximately 40 nm) and avoid ion channelling, very high ion-beam incidence angles (+/- 62°) were used (Figure 2.4), achieved by tilting the stage to -10°, adding to the 52° tilt of the FIB column.

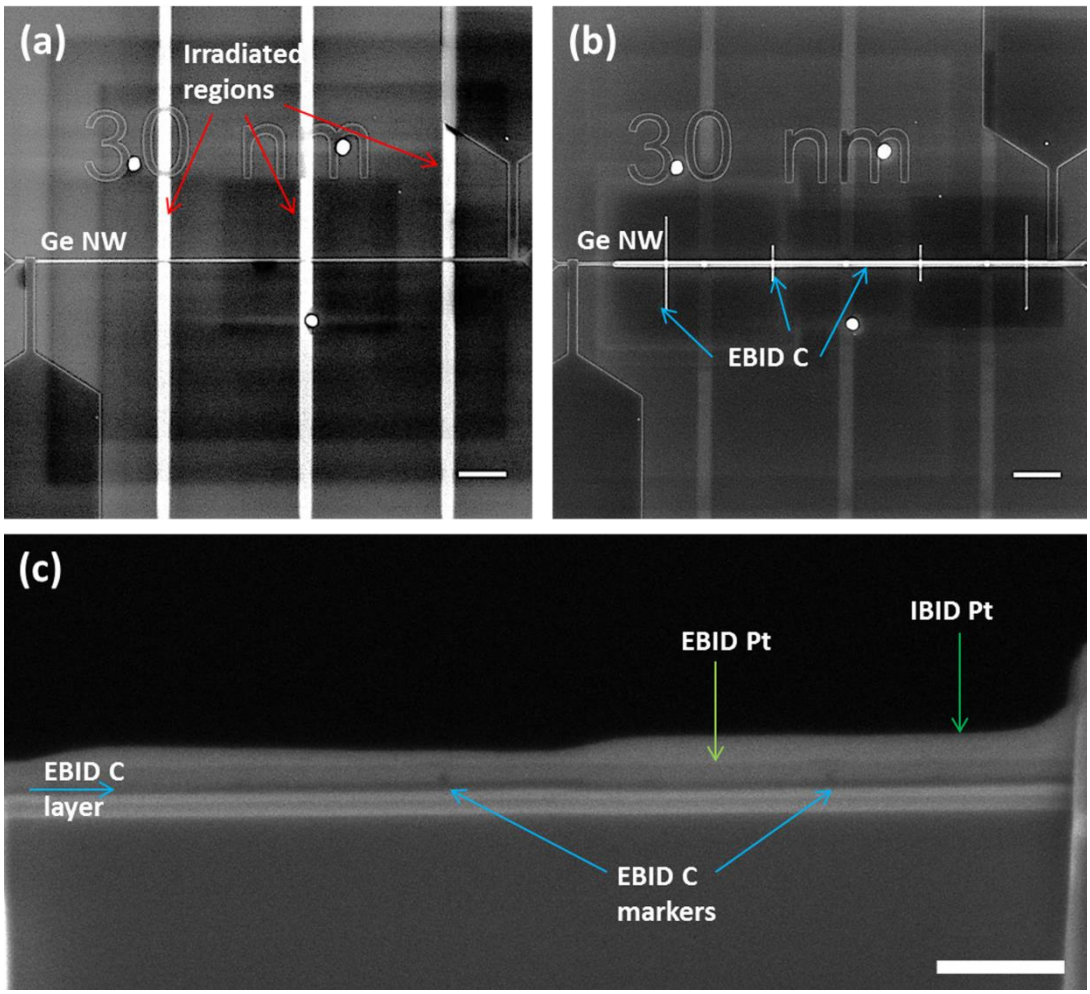

Figure 2.3. Overview of use of EBID carbon for indication of NW exposure during thinning. Scale bar for all images is 1 µm.

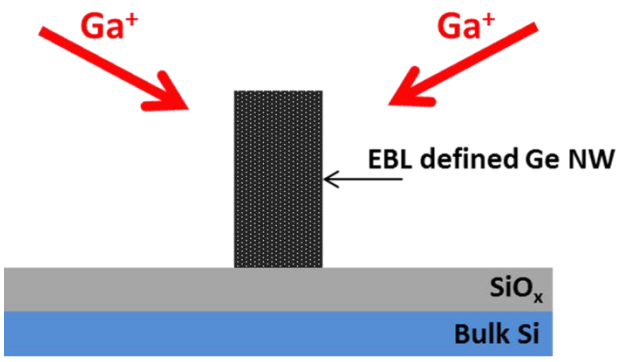

Figure 2.4. Schematic of 62° tilt ion irradiation of EBL defined Ge NW in cross sectional view.

2.4. HRTEM of irradiated nanowires

The Gatan double tilt holder was used for high resolution TEM (HRTEM) imaging as tilt in two directions is nearly always required to orient a NW to a zone axis. To tilt to a zone axis, the convergent beam electron diffraction (CBED) pattern was used to navigate the orientation until a symmetric pattern was achieved. Once a zone axis was achieved, a selected area diffraction (SAD) pattern was acquired by inserting the selected area aperture and spreading the beam. To protect the CCD camera, the beam blank was inserted to block the direct beam.

2.4.1. HRTEM of irradiated grown nanowires

NWs were transferred to labeled/trenched SiN membranes via dry transfer. There were nine 200 × 200 μm^2 membrane sites per grid, each was labelled (for identification) and patterned (to open trenches for HRTEM) with the FIB. NWs which lay securely across a trench and required no more than 10 degrees tilting to a low index zone axis for lattice resolution imaging were selected for irradiation. The tilt required for a specific zone axis was recorded as well as any intrinsic defects. Images of the position of the NW as well as lattice resolution images were acquired.

2.4.2. HRTEM of irradiated lithography defined GeOI nanowires

Irradiated GeOI NWs were extracted in TEM lamellae, as described in section 2.3 Irradiation of EBL defined GeOI Nanowires. The GeOI is fabricated such that the Ge layer crystal is in the same orientation as the bulk Si carrier. This makes the tilt to zone axis easier as the bulk Si can be used for this. All of the GeOI NWs are defined with a “growth direction” in [100] direction and hence the zone axis imaged is [010].

2.5. In situ annealing of irradiated nanowires

An in situ Gatan Model 628 single-tilt heating stage TEM holder was used for all anneals presented in this study. The ramp/temperature used for each NW varied. The sample was loaded in the same orientation in the in situ heating stage as it was for HRTEM imaging in the double tilt holder. The in situ heating stage is only capable of single tilt so the sample was tilted as close to the zone axis used for high resolution imaging as possible. For most samples tilting in two directions is required to achieve a zone axis orientation for lattice resolution imaging. The TEM was operated in bright field mode, isolating the direct beam with the objective aperture, to take advantage of the contrast between the crystalline and amorphous regions. Temperature was controlled using a Gatan Model 901 SmartSet hot stage controller. Temperatures varied from 100 – 500 °C (the temperature dispersion control is approximately 0.1 - 0.5 °C, as per the manufacturer's specifications). Images were acquired every minute at the set temperatures.

2.6 Iradina (ion range and damage in nanowires)

Iradina was used to simulate ion beam irradiation in Ge nanowires. The material of the wire was defined as Ge and the surrounding material set as vacuum. For this experimental procedure the nanowire was defined as a cylinder with a varied diameter, 65 nm, 45 nm or 25nm. The accelerating voltage was set to 5 kV or 30 kV for the Ga ion source. A section of the nanowire was defined by the periodic boundary conditions (PBC), essentially defining a 2 dimensional cross section of the nanowire, which in turn is divided into a number of cells (defined by the user). For the results presented here, the PBC was set at 80 × 80 nm^2, with the individual cells

set at 0.5 × 0.5 nm^2. The ion beam direction is set orthogonal to the nanowire length as the crystallinity of the material is disregarded due to random phase approximation (RPA) of the target atoms so any ion channeling in the crystal is not accounted for.

2.7 Nickel-capped germanium nanopillar fabrication

The process flow for the fabrication of Ni-capped Ge nanopillars is illustrated in Figure 2.5. A method to produce nanopillars of Ge with varied diameters has been developed with the use of EBL. Ni-capped germanium nanopillars were fabricated on Ge(001) substrates. A positive tone EBL resist was used to expose desired circular areas on the Ge substrate as shown in Figure 2.5.

Initially, a two layer (PMMA-copolymer) EBL resist was used to facilitate a facile metal lift process. However, an undesirable lip of Ni was observed for the pillars, which is attributed to the collapse of the upper resist during metal evaporation. As the metal is used as a mask for etching, this results in larger diameter pillars than desired. Hence, for further sample preparation the Ge substrate was patterned by EBL using SML-50, a high resolution positive tone EBL resist.[9] Single pixel dot exposures, with 1 μm pitch, were defined in a line with large markers on either side.

The diameters of the dots were varied with the dose (dwell time) at each spot; the diameter increases with increasing dose. The dose range used was 0.2 – 6.4 fC per single exposure and the electron beam was operated at 10kV accelerating voltage. After exposure, the resist was developed in 7:3 IPA/deionised water for 30 s followed by IPA for 15 s and dried under a flow N_2 for 30 sec. A 50 nm thick Ni layer was evaporated, by electron beam evaporation, onto the patterned substrate

followed by a metal lift-off in acetone to achieve Ni dots (and markers) on the Ge substrate. The Ge was etched, using the Ni as the hard mask, in a Cl reactive ion etch (RIE) at 20 °C, 30 sccm Cl_2, 10 mtorr and 80W RF.[7]

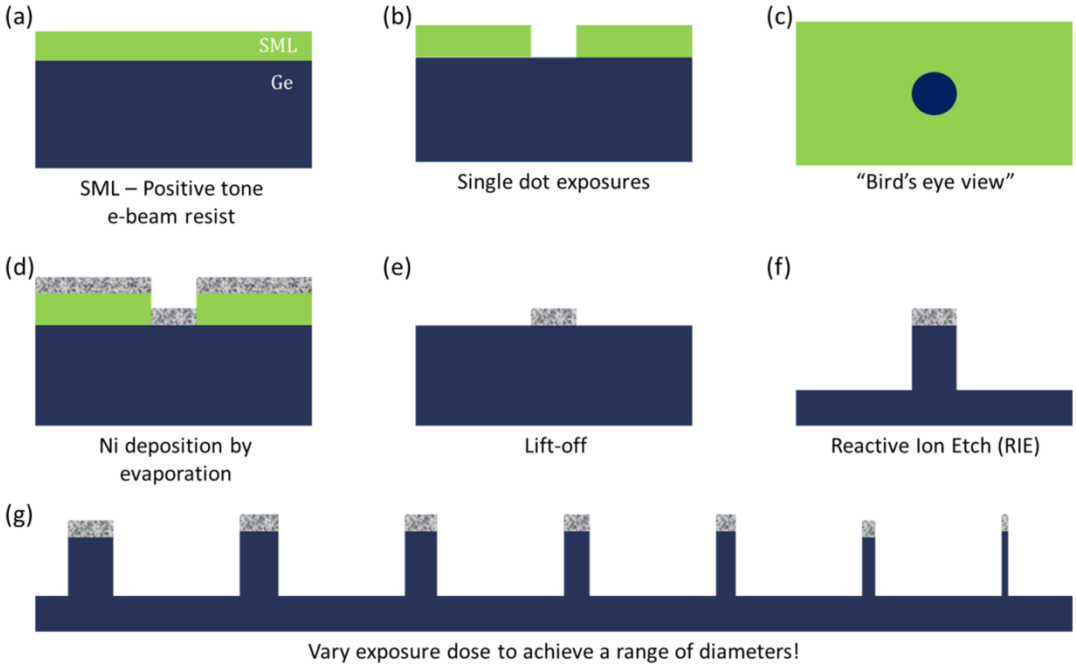

Figure 2.5. Process flows of Ni-capped Ge nanopillars using SML resist.

For annealing experiments, a line of pillars was extracted in a cross section and transferred to an omniprobe grid, as shown in Figure 2.6. To help aid in polishing the cross section to the region of interest, a line of EBID carbon was deposited along the line of dots with a total nominal height of 1 µm, similar to the method described for inline nanowire cross sections described previously in chapter 2. This helps to ensure cut placement and aids in the final FIB polishing of the cross section because the EBID-C has good contrast against the platinum (Pt) protection. The EBID-C also acts as an insulation layer to encapsulate the Ni/Ge pillars. The next layer of protection with the dimensions 15 µm × 2 µm and a nominal height of 250 nm of EBID-Pt was deposited followed by 2 µm ion beam induced deposition (IBID) Pt.

During thinning, the cross section was polished only from the front side, by turning the grid 180° with a stage rotation to polish the other side from the front for accurate final polishing.

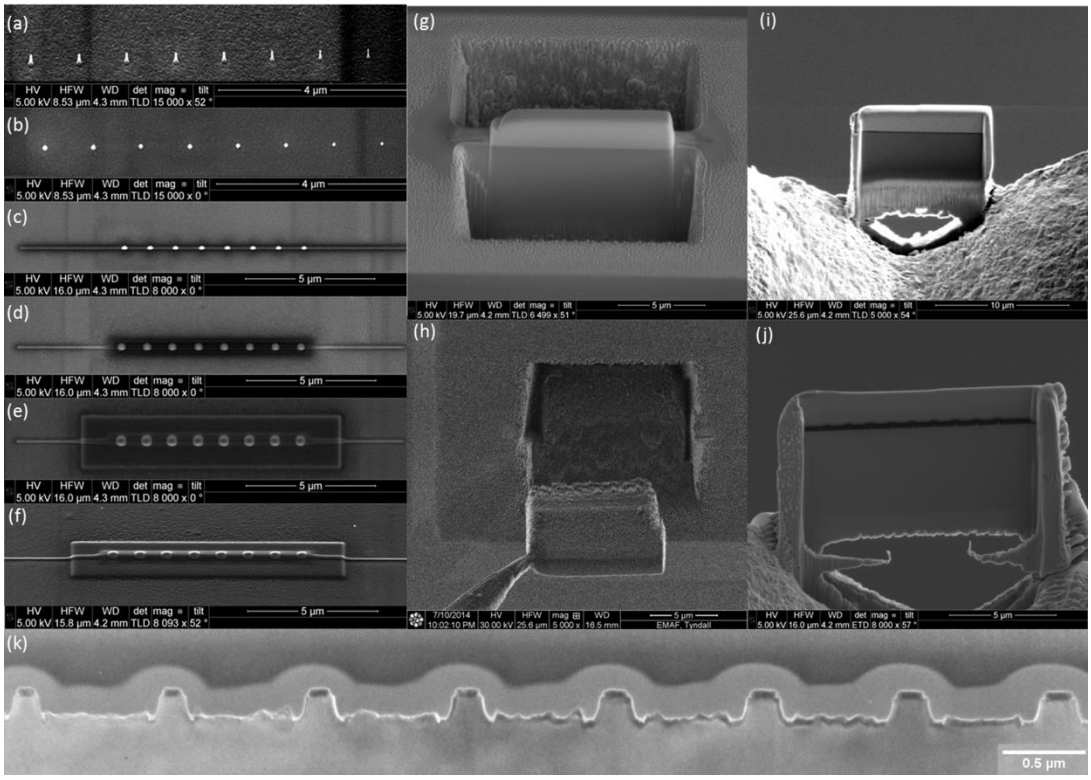

Figure 2.6. Overview of extraction of Ni-capped Ge nanopillars in a TEM lamella. (a) Tilted view of nanopillars. (b) "Birds eye view" of nanopillars. (c) EBID-C line deposited along nanopillars. (d) EBID-Pt as protection of ion beam. (e) Initial IBID-Pt for lamella preparation. (f) Tilted view of initial IBID protection showing nanopillars are fully encapsulated. (g) Trenches milled (with the FIB) either side of the lamella to be extracted. (h) Lamella extracted using omniprobe which transfers the lamella to the omniprobe grid. (i) Lamella attached to the omniprobe grid at the two base points for added stability during in situ annealing experiments. (j) Lamella during thinning process using FIB, dark line of C-protection observed as well as the bumps which show the topography of the nanopillars and hence the endpoint of thinning is close. (k) Example of TEM image of array of nanopillars of increasing diameters extracted in a TEM lamella.

A native GeO_x removal step is required before EBL resist deposition to optimise the surface to avoid dewetting and achieve a uniform resist. The water soluble oxide is removed in a 30 s dip in deionised water, followed by a re-oxidation of surface with a 30 s dip in 4.5 M nitric acid (HNO_3) and a final oxide removal and surface

passivation step in 10% HCl for 10 min.[10] No oxide removal step was performed on the exposed surface before metal evaporation, which could be a major factor for the rough Ge/Ni interface. Ideally, the sample should be placed directly in the metal evaporator post resist development to avoid oxidation of Ge in ambient air.[11,12]

2.8. TEM characterisation of Ni-capped Ge nanopillars

2.8.1. HRTEM of Ni-capped Ge nanopillars

Before annealing, the structures were imaged using a Gatan double tilt imaging holder in a JEOL 2100 HRTEM and tilted to a low index zone axis for HTREM imaging. The bulk substrate was used to orientate the sample into a zone axis. HRTEM images were acquired of the interface between Ge and Ni interface. After the anneal, the bulk Ge is unchanged and hence can be used to find the same zone axis and orientate the nanopillars as they were for HRTEM before the anneal. Lattice resolution images were acquired of the Ge-Ni interface. Because of the size of the germanide region, acquiring a SAED pattern alone is difficult without contribution from the Ge crystal. Lattice resolution images were required to be able to obtain fast Fourier transforms (FFTs) from lattice resolution images to determine germanide phase and orientation.

2.8.2. In situ annealing of Ni-capped Ge nanopillars

A Gatan 628 single tilt heating holder was used for in situ annealing. The pillars were imaged in bright-field mode using the smallest objective aperture during the anneal to enhance the contrast between the Ni and Ge. The tilt required for HRTEM was not achievable with the single tilt holder, also, during the anneal a lot of drift

occurred which would have diminished any possibility of HRTEM during the anneal. The initial temperature and ramp rate was varied for the anneals. After each temperature increase, a stabilisation time of approximately 10 s was given. Smaller temperature increases, for example 10 degrees vs 100 degrees, resulted in less drift. Images were acquired at 1 minute intervals with 1 second acquisition time. After annealing, the sample was imaged in the double tilt holder again for HRTEM imaging in the same orientation as prior to annealing.

2.9 References

1 Biswas, S., Singha, A., Morris, M. A., Holmes, J. D. Inherent control of growth, morphology, and defect formation in germanium nanowires. *Nano Lett.* 12, 5654-5663, doi:10.1021/nl302800u (2012).

2 Biswas, S., O'Regan, C., Petkov, N., Morris, M. A., Holmes, J. D. Manipulating the growth kinetics of vapor-liquid-solid propagated Ge nanowires. *Nano Lett.* 13, 4044-4052, doi:10.1021/nl401250x (2013).

3 O'Regan, C., Biswas, S., O'Kelly, C., Jung, S. J., Boland, J. J., Petkov, N., Holmes, J. D. Engineering the growth of germanium nanowires by tuning the supersaturation of Au/Ge binary alloy catalysts. *Chem. Mater.* 25, 3096-3104, doi:10.1021/cm401281y (2013).

4 Biswas, S., O'Regan, C., Morris, M. A., Holmes, J. D. In-situ observations of nanoscale effects in germanium nanowire growth with ternary eutectic alloys. *Small* 11, 103-111, doi:10.1002/smll.201401240 (2015).

5 Gangnaik, A. S., Georgiev, Y. M., Collins, G., Holmes, J. D. Novel germanium surface modification for sub-10 nm patterning with electron beam lithography and HSQ resist. *J. Vac. Sci. Technol.* **awaiting publication** (2016).

6 Collins, G., Aureau, D., Holmes, J. D., Etcheberry, A., O'Dwyer, C. Germanium oxide removal by citric acid and thiol passivation from citric acid-terminated Ge(100). *Langmuir* 30, 14123-14127, doi:10.1021/la503819z (2014).

7 Ran, Y. Das, S., Hobbs, R., Georgiev, Y., Ferain, I., Razavi, P., Akhavan, N. D., Colinge, C. A., Colinge, J. Top-down process of germanium nanowires using EBL exposure of hydrogen silsesquioxane resist. *J. Ultimate Integr. Silicon* 145-148, doi: 10.1109/ulis.2012.6193378 (2012).

8 Kelly, R. A., Holmes, J. D. & Petkov, N. Visualising dicrete structural transformations in germanium nanowires during ion beam irradiation and subsequent annealing. *Nanoscale* 6, 12890-12897, doi:10.1039/c4nr04513k (2014).

9 Gangnaik, A. , Georgiev, Y. M., McCarthy, B., Petkov, N., Djara, V., Holmes, J. D. Characterisation of a novel electron beam lithography resist, SML and its comparison to PMMA and ZEP resists. *Microelectron. Eng.* 123, 126-130, doi:10.1016/j.mee.2014.06.013 (2014).

10 Hobbs, R. G., Schmidt, M., Bolger, C. T., Georgiev, Y. M., Fleming, P., Morris, M. A., Petkov, N., Holmes, J. D., Xiu, F. X., Wang, K. L., Djara, V., Yu, R., Colinge, J. P. Resist-substrate interface tailoring for generating high-density arrays of Ge and Bi_2Se_3 nanowires by electron beam lithography. *J. Vac. Sci. Technol. B* 30, doi:10.1116/1.4724302 (2012).

11 Law, J. T., Meigs, P. S. Rates of oxidation of germanium. *J. Electrochem. Soc.* 104, 154-159, doi:10.1149/1.2428524 (1957).

12 Prabhakaran, K., Ogino, T. Oxidation of Ge(100) and Ge(111) surfaces: an UPS and XPS study. *Surf. Sci.* 325, 263-271, doi:10.1016/0039-6028(94)00746-2 (1995).

Chapter 3

Investigating crystal damage in germanium nanowires due to ion beam irradiation

3.1. Abstract

In this chapter we detail the application of electron microscopy to visualise discrete structural transitions incurring in single crystalline Ge nanowires upon Ga-ion irradiation and subsequent thermal annealing. Sequences of images for nanowires of varying diameters subjected to an incremental increase of the Ga-ion dose were obtained. Intricate transformations dictated by a nanowire's geometry indicate unusual distribution of the cascade recoils in the nanowire volume, in comparison to planar substrates. Following irradiation, the same nanowires were annealed in the TEM and corresponding crystal recovery followed in situ. Visualising the recrystallization process, we establish that full recovery of defect-free nanowires is difficult to obtain due to defect nucleation and growth.

3.2. Introduction

The irradiation of single crystal semiconductor substrates with energetic ion beams to introduce dopants has been developed extensively over the years, turning ion implantation into a standard doping technique in semiconductor manufacturing. Essentially, doping involves introducing an impurity into a substitutional or an interstitial site within the crystal which alters the electronic structure of the material. Ion implantation allows for accurate control of doping achieving precise dose, depth profile and uniformity. Single crystalline semiconductor nanowires require uniform and controllable doping for the creation of high performance devices such as field effect transistors (FETs),[1,2] advanced sensors,[3,4] photovoltaic[5] and light emitter[6] devices. Specifically, junctionless multigate FETs[7] require a uniform distribution and

high level of active dopants (>1×10^{19} atoms cm^{-2}) within perfectly crystalline source, gate and drain regions for reliable device performance, as demonstrated by both ab-initio simulations and experimental devices.[8] With the aim to achieve enhanced control over the dopant levels and their uniform distribution, ion implantation has been applied to introduce dopants in Si and Ge nanowires.[9-12] In particular, Ge is a potential material for logic and optoelectronic devices due to its high hole and electron mobilities.[13] The processing of bulk and particularly nanostructured Ge, including ion implantation and subsequent crystal recovery, requires further understanding.[14-16]

The interaction of the energetic ions with single crystal nanowires, in comparison to those in bulk substrates, can be considerably altered due to (i) ions impinging at different incident angles at a surface and (ii) abrupt termination of resultant atom recoils at nanowire surfaces.[17] Whilst the range of ion interactions with bulk substrates, accumulated damage and impurity distribution are theoretically simulated through modelling nuclear collisions involving ions and recoiling atoms using SRIM (stopping and range of ions in matter) computer code[18], the simulation of ion interactions in nanowires has recently been developed using an extension of the SRIM code; iradina (**i**on **r**ange **a**nd **d**amage **i**n **na**nostructures).[17,19] Iradina is a static Monte Carlo simulation similar to SRIM, except the target shape can be defined within a nanoscale simulation volume.

Herein, electron microscopy data demonstrating the discrete structural transformations within single crystalline Ge nanowires upon ion irradiation is presented. Using a procedure based on a correlative analysis approach,[20] sequences

of TEM images following accumulated crystal damage at varying Ga-ion fluence and energy were acquired. A relationship between the initial nanowire geometry and crystal structure is identified.

3.3. Experimental Procedure

3.3.1 Instrumentation

The instruments used were an FEI Helios 600i NanoLab Dual Beam system (SEM/FIB) and a JEOL 2100 HRTEM equipped with a Gatan double tilt imaging holder. The dual beam FIB was used for all ion beam exposures using the Ga ion source. The double tilt holder was used for all high resolution TEM imaging.

3.3.2 Nanowires

Two methods were used for fabrication of nanowires used in this study – bottom-up and top-down. The bottom-up Ge nanowires were grown from Au NP seeds via a supercritical fluid process on Si substrates by Dr Subhajit Biswas, Dr Olan Lotty and Dr Colm O'Regan.[15] Most of the nanowires were grown in the [111] direction, a small fraction of the nanowires were grown in the [211] direction, some of which contain intrinsic longitudinal defects in the [111] direction. The top-down Ge nanowires were defined on 50 nm GeOI substrates using HSQ (Hydrogen silsesquioxane) which is a negative tone electron beam resist. The EBL system used is a Raith eLINE operated at 10 kV by Dr Anushka Gangnaik.

3.3.3. Concurrent imaging platform

The carrier chip platform used for step-wise implantation/imaging of a specific nanowire is depicted schematically in Figure 3.1. Si chips with silicon nitride (SiN) membrane windows were used (Ted Pella), which were patterned using the FIB to label and open slits in the membrane. The patterning is of benefit for two reasons; the slits allow high resolution imaging of sections of the nanowire as well as facile navigation to locate the same nanowire. The parameters for patterning were: 7 lines 10 µm apart, 70 µm long and 0.5 µm wide for a nominal thickness of 300 nm with the Ga ion beam operating at 30 kV, 3 nA.

The nanowires were first imaged in the TEM where the growth direction, tilt required to achieve a low index zone axis and any intrinsic defects were identified. Nanowires that required no more than 10 degrees tilting in one direction, preferably along or perpendicular to their long axis, and fully crossed the opening were selected. The mounting of the membrane chips to the TEM holder was done with the aid of an optical microscope, ensuring the grid was mounted with a fixed orientation. This allows the nanowires to be imaged in the same orientation after each exposure. This accurate mounting method became more important as the nanowire reached a near/fully amorphous state. The grid was then transferred to the SEM/FIB for implantation. The nanowire was located using the SEM and then orientated (stage was rotated and moved in x- and y-directions) so that the nanowire length was at eucentric height when the stage was tilted, i.e. the nanowire was aligned left to right in the SEM. The eucentric height is the height where a point, here our nanowire, remains stationary when tilted. The coincidence point of the SEM and FIB is set at

the eucentric height. The stage was tilted to 52° so the FIB is normal to the substrate surface. Most exposures were done at this tilt unless the tilt required for a nanowire in the TEM is <2°, in this case the stage was tilted to 45° to avoid ion channelling. Ion channelling occurs if the ion beam direction is parallel to a crystal direction. The effect of ion channelling is a longer range of ion and hence a variation in implantation depth. The pattern for implantation was defined in the ion beam window as a Si mill rectangle: 10 × 10 μm^2 area, 125 ns dwell time, 1 pass and with a total time of 0.316 s to achieve a dose of 1.9×10^{13} ions cm^{-2}, operating at 30 kV (or 5 kV), 9.7pA (10pA aperture at 5kV). The carrier chip was then transferred back to the TEM in the same orientation to image the nanowire after doping. The concurrent implantation/imaging steps were repeated multiple times to build up the step-wise increase in the dose. The maximum implantation dose in our studies was 1.14×10^{14} ions cm^{-2} which corresponds to 6 successive steps.

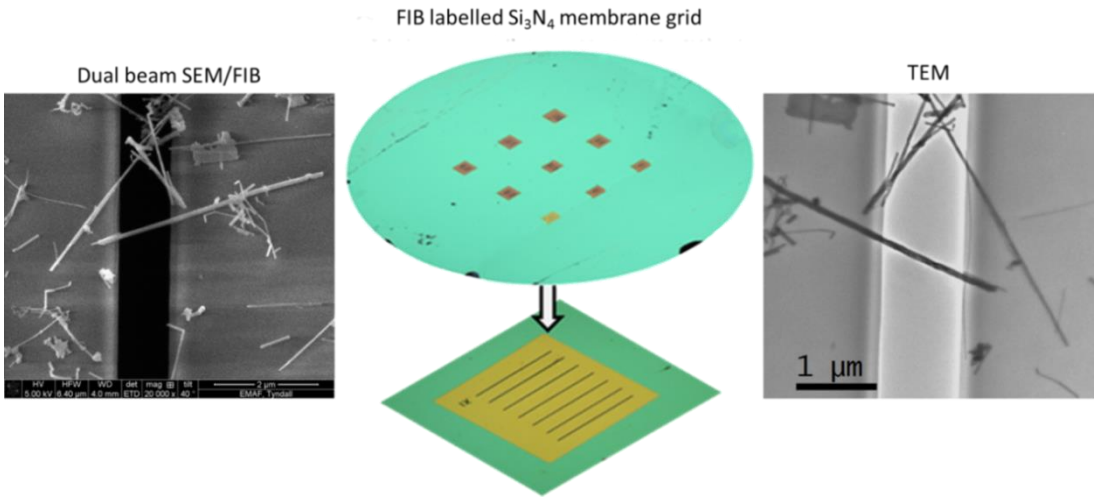

Figure 3.1. Overview of platform for correlative imaging of nanowire on Si_3N_4 membrane grid.

3.3.4. Iradina (ion range and damage in nanostructures)

Iradina was used to simulate ion beam irradiation in Ge nanowires. The material of the wire was defined as Ge and the surrounding material set as vacuum. For this experimental procedure the nanowire was defined as a cylinder with a varied diameter, 65 nm, 45 nm or 25nm. The accelerating voltage was set to 5 kV or 30 kV for the Ga ion source. A section of the nanowire was defined by the periodic boundary conditions (PBC), essentially defining a 2 dimensional cross section of the nanowire, which in turn is divided into a number of cells (defined by the user). For the results presented here, the PBC was set at 80 × 80 nm^2, with the individual cells set at 0.5 × 0.5 nm^2. The ion beam direction is set orthogonal to the nanowire length as the crystallinity of the material is disregarded due to random phase approximation (RPA) of the target atoms so any ion channeling in the crystal is not accounted for.

3.4. Results and Discussion

3.4.1. 30 kV single exposure irradiation

In Figure 3.2 cross-sections of three different nanowires are presented, all approximately 45 nm in diameter, subjected to an increasing Ga-ion dose at 30 kV. The extent of crystal damage in the nanowires at the fixed implantation energy can be directly related to the dose used. At a fluence of 1.9×10^{13} ions cm^{-2} (Figure 3.2 a and d), the arc of crystal damage shows large contrast variations due to lattice distortions resulting from clustering of point defects. Small amorphous regions (3 - 5 nm in size) were seen at the nanowire surface imaged at lattice resolution, imaged

with the electron beam perpendicular to the longitudinal direction of the nanowire (Figure 3.3). With the increase of the implantation fluence by 2 and 3 times (Figure 3.2 b -and c), further increase of the top surface damage depth from approximately 18 nm to 25 and 34 nm, respectively, in the form of full amorphisation towards the interior (across the diameter) of the nanowires was observed.

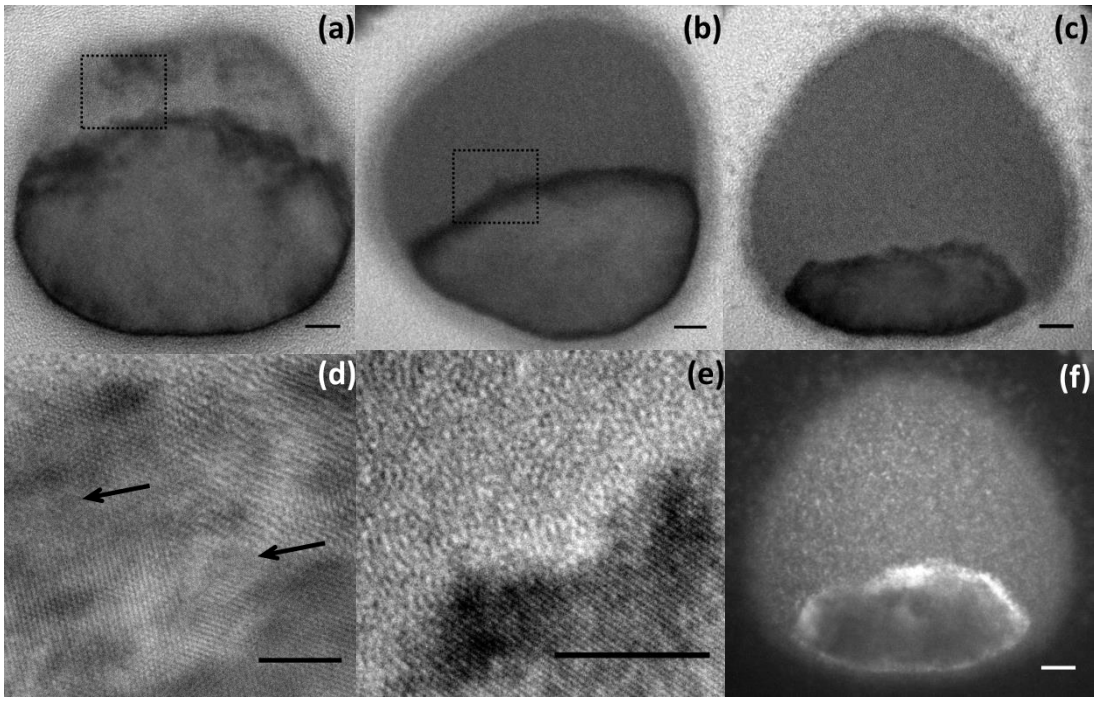

Figure 3.2. Cross-sectional TEM images of different Ge nanowires of approximately 45 nm in diameter after irradiation at 30 kV with increasing Ga-ion doses of (a) 1.9×10^{13}, (b) 3.8×10^{13} and (c) 5.7×10^{13} ion cm^{-2}. (d) and (e) lattice resolution TEM images taken from the marked areas in (a) and (b), respectively. (f) Dark field TEM image of the same nanowire as in (c). In all images, the direction of the ion flux is from the top and the cross-sections were imaged in the [111] zone direction. Arrows in (d) mark small amorphous pockets. Scale bar for all images is 5 nm.

Additionally, Figure 3.2 demonstrates gradual decrease in the roughness of the amorphous to crystalline interface as a function of increasing fluence as the amorphisation depth reaches the maximum range of the ion in the material.

Measuring from the top and centre of the nanowire in Figure 3.2 c, this depth for a 30 kV Ga ion beam in Ge is approximately 32 nm. In comparison to the experimental results for ion irradiation of Ge (001) substrates, the maximum depth was approximately 35 nm for a dose of 1.45×1014 ions cm-2 for a 30kV ion beam. Intrinsic (111) stacking fault defects present in some of the Ge nanowires (Figure 3.5 a) produced during growth showed a slight susceptibility to damage at the grain boundary but this was a minimal variation and cannot be fully attributed to the intrinsic defect present. Other nanowires presented in Figure 3.5 b-d also show a non-uniform crystalline-amorphous (c/a) interface. Importantly, the analysis of the crystal damage was done post-factum, with no account of the initial nanowire structure and orientation towards the incoming ion beam. Conventionally, when implanting planar substrates the orientation of the incoming ion beam to the crystal is known, set at an angle (about 7 degrees off normal direction) to minimize unwanted channeling effects.

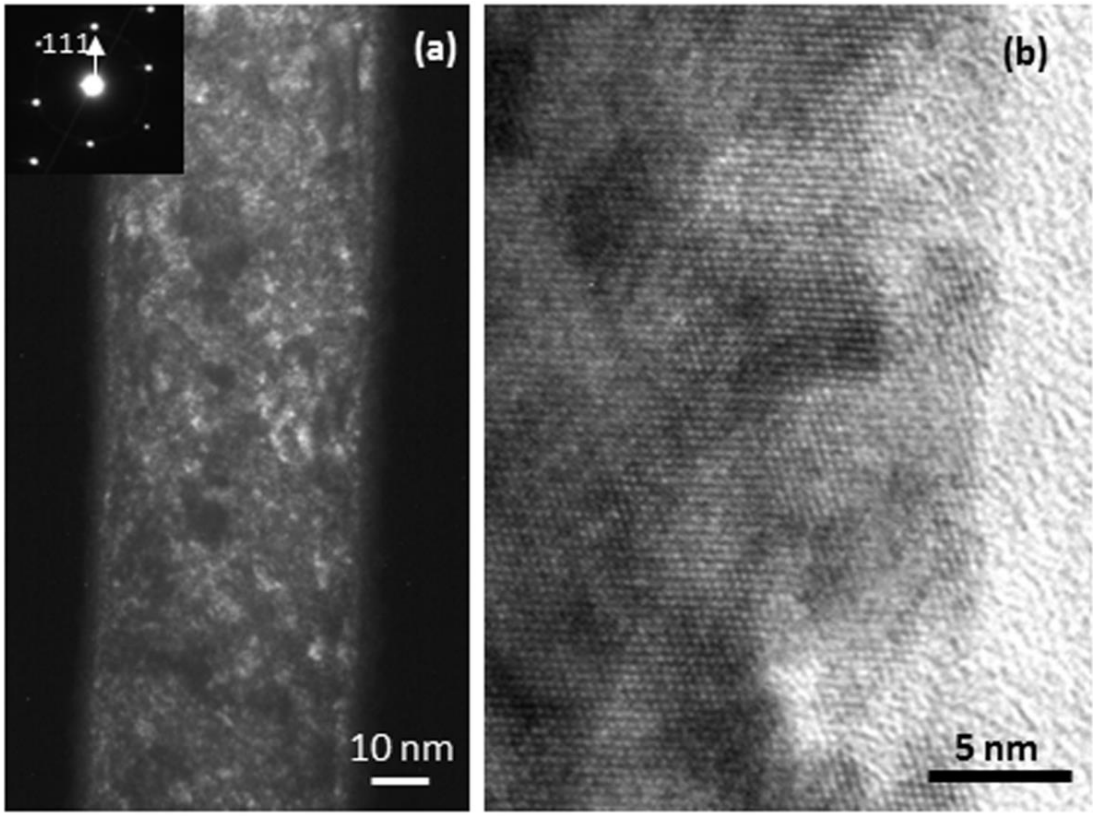

Figure 3.3. Consecutive 30kV Ga ion irradiations of a 50 nm diameter Ge nanowire 6 degrees off the [110] zone direction at a fluence of 1.9×10^{13} ion cm-^{12}. (a) Dark field imaging taken under g, 2g with g = 220 condtions. (b) Corresponding lattice resolution image taken in the [110] zone direction at the nanowire side surface. After further irradiation; The white spots in the dark field images are due to roughness of the surface but could also be Ga clusters embedded in the NW.

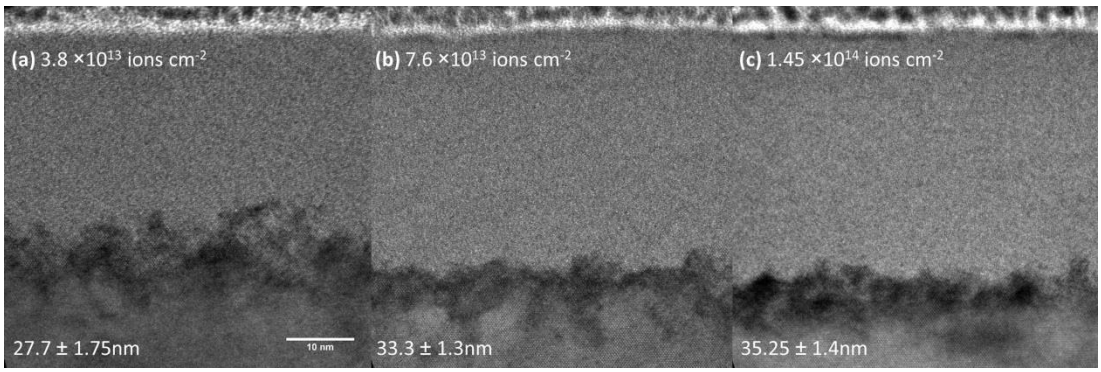

Figure 3.4. Cross sectional TEM of Ge(001) substrate exposed to Ga-ion implantations 7 degrees off the normal direction at increasing fluences for 30 kV. Doses and measured average thicknesses of amorphous layers are given in the insets.

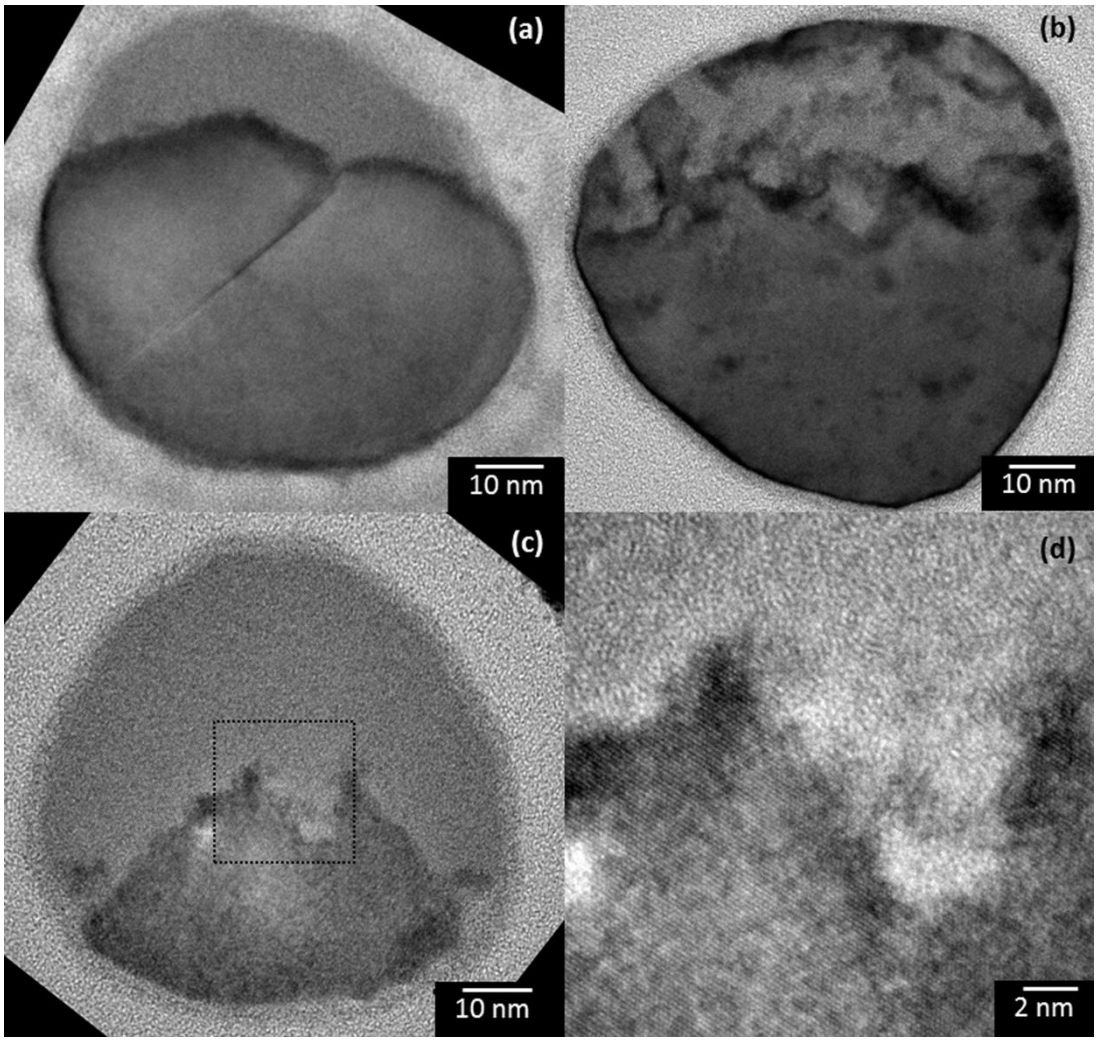

Figure 3.5. Cross-sectional TEM images of different nanowires subjected to Ga-ion implantations (a-d) at 30kV with the incoming irradiation from the top. Excluding the nanowire in (a), all nanowires were defect free and grown in the [111] direction. (a) 64 nm Ge nanowire grown along the [211] direction irradiated with a fluence of 3.8×10^{13} ion cm^{-2}, featuring intrinsic stacking fault defects along the (111) set of planes. (b) 74 nm diameter Ge nanowire irradiated with a fluence of 1.9×10^{13} ion cm^{-2}, featuring amorphous pockets within a mostly crystalline structure. (c) 60 nm nanowire irradiated with a fluence of 7.6×10^{13} ion cm^{-2} featuring extended but not full amorphisation leaving crystalline domains towards the middle/bottom of the nanowire cross-section. (d) Lattice resolution image of the area marked in (c), demonstrating an uneven c/a interface.

3.4.2. Concurrent stepwise 30 kV irradiation

A procedure to accurately follow the evolution of crystal damage in nanowires was developed based on a correlative analysis approach,[20] using a carrier chip platform with markers that facilitated exchange between the TEM and FIB/SEM instruments (Figure 3.1). Figure 3.6 represents the evolution of damage build-up in a 38 nm Ge nanowire with a step-wise increase in the Ga-ion dose at 30 kV, starting at a minimum fluence (step) of 1.9×10^{13} ions cm^{-2}. The nanowire was first imaged in the TEM to obtain information about crystallinity and its orientation towards the incoming electron beam. Although most of the examined nanowires were defect free and grown along the [111] direction, in order to demonstrate the capabilities of our visualization methodology a [211] grown Ge nanowire with a set of stacking fault defects along the [111] direction was selected. A cross-section of an equivalent nanowire, having the same type of intrinsic defect and growth orientation (but with a larger diameter) is presented in Figure 3.5 a. The carrier chip was first tilted approximately 8 degrees (in one direction) to image the nanowire in the [110] zone direction. After transferring to the SEM/FIB instrument the sample was imaged first with the SEM to locate and orient the carrier chip. After tilting the stage to 52 degrees (ion beam normal to the carrier chip surface) successive ion irradiation was performed at a known tilt angle, i.e. 8 degrees away from the (110) zone axis.

Following ion implantation, the nanowire sample was transferred back to the TEM and imaged along the same zone axis to observe sustained structural transformations. These sequences were repeated several times to build up the implantation dose and obtain images monitoring the consecutive transformations. At the lowest Ga-ion

fluence used (Figure 3.6 b) lattice distortions as well as amorphous regions (about 5 nm in size) were observed in comparison to the initial single crystalline nanowire. By further multiplying the initial ion fluence of 1.9×10^{13} ions cm^{-2} by 2, 3 and 4 times the volume of amorphous regions increased, breaking the stacking fault planes at the centre of the nanowire and transforming almost the whole volume of the nanowire amorphous. These transformations were unevenly distributed along the nanowire length. At the highest fluence used, the resultant amorphous nanowire contained isolated crystalline domains in the sub-10 nm range, with the same orientation as the initial single crystal structure, as seen from the lattice resolution image (Figure 3.6 f); some slightly misoriented domains were also observed. Taking into account the cross-sectional data (Figure 3.2 and Figure 3.5), one can envision that these crystalline islands would be predominantly located towards the middle and bottom (bottom is defined as the side opposite to the incoming ion beam) of the nanowire. These data collaborate very well to the simulations by iradina (Figure 3.7 a-d), where the lowest number of atom displacements for a 45 nm nanowire is in the middle and bottom of the nanowire cross-section.

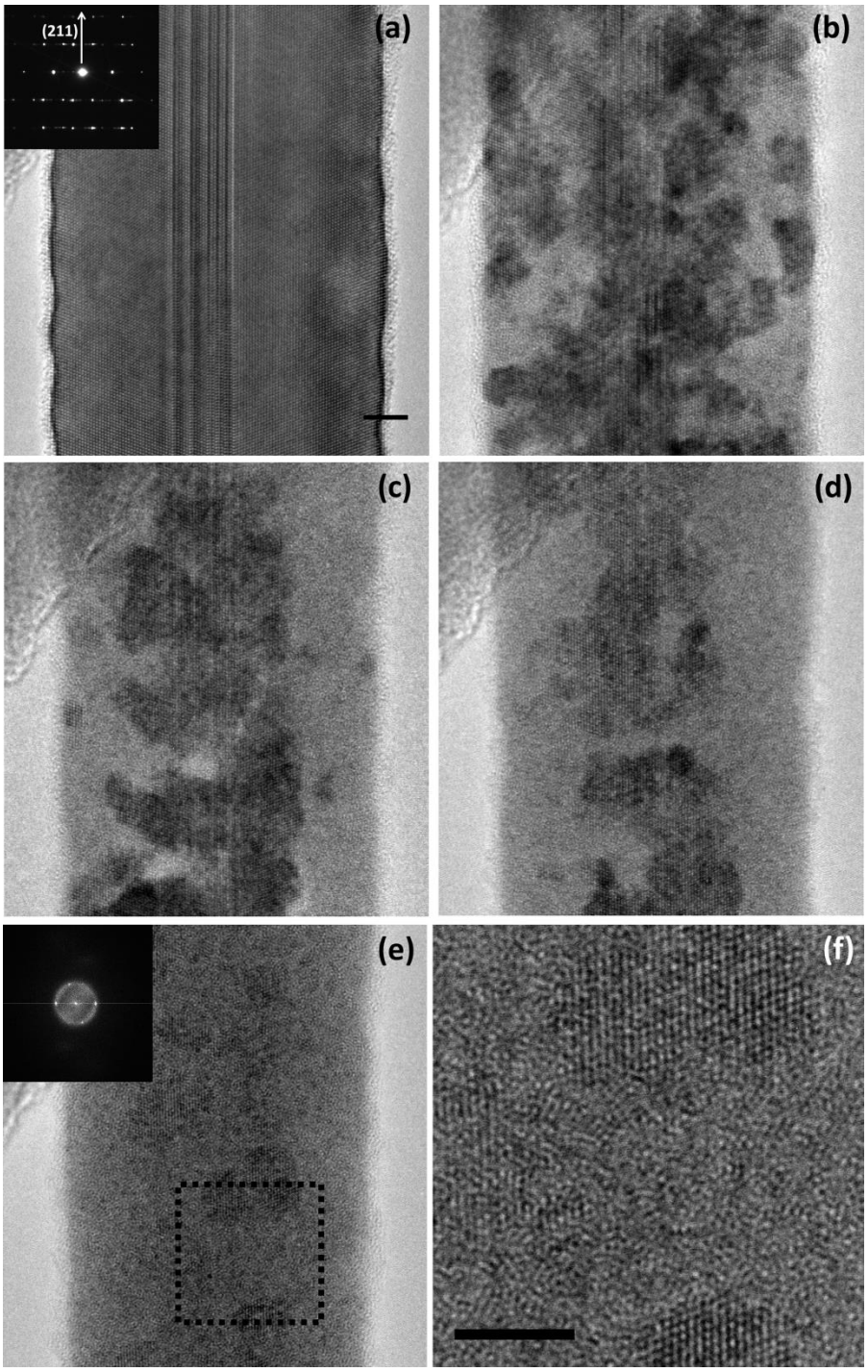

Figure 3.6. Step-wise irradiation of a 38 nm diameter Ge nanowire with a 30 kV Ga-ion beam. (a) Initial nanowire before irradiation imaged close to the [110] zone axis, inset demonstrating complex SAED due to longitudinal (111) stacking fault defect. (b-e) Images of the same area taken close to the same zone direction after irradiation with increasing fluence of (b)1.9×10^{13}, (c), 3.8×10^{13} (d) $5.7 \times 10^{13}$and (e) 7.6×10^{13} ion cm^{-2}. All images were acquired at the same magnification. (f) Inset of (e) shows FFT of region marked. Lattice resolution TEM image of the marked area in (e), demonstrating crystal domains orientated in the same [110] direction as the initial nanowire. Scale bar for all images is 5 nm.

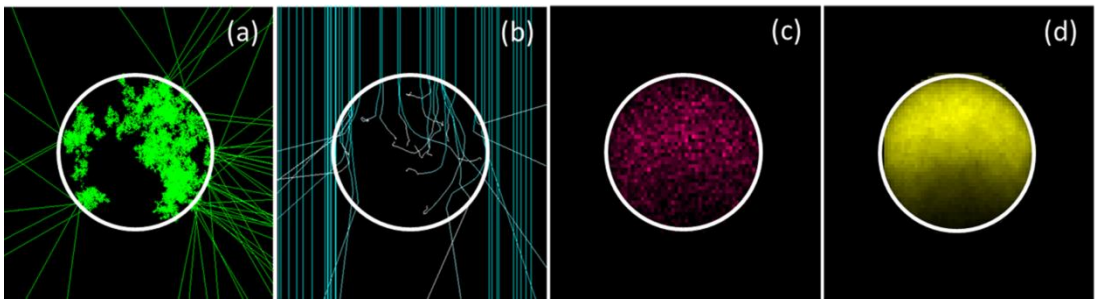

Figure 3.7. Iradina maps of (a) cascade recoils, (b) ion paths, (c) implanted ions and (d) atom displacements based on a cylindrical Ge nanowire with a diameter of 45 nm irradiated by a 30 kV Ga ion beam orthogonal to the nanowire.

The cascade recoils (Figure 3.7 a) show the resultant collisions which occur within the NW. The ion paths (Figure 3. b) show the path of the ions as they enter, and leave, the NW volume. Both the cascade recoils and ions paths illustrate how the ions and atoms from NW can easily be expelled and hence resulting in a lower concentration of implanted ions as well as sputtering events at NW surface. The implanted ion map (Figure 3.7 c) shows the estimated distribution of ions within the NW. The atom displacements map (Figure 3.7 d) shows the distribution of displacement of atoms within the volume, which can be used to estimate the damage and amorphisation in the NW.

In comparison, a larger diameter Ge nanowire (64 nm, grown along [111] direction with prominent stacking fault defects along [11-1] direction) implanted with successive Ga-ion doses of 1.9×10^{13} to 7.6×10^{13} ions cm^{-2}, imaged along the (110) zone axis, displayed an increase in lattice distortions and build-up of amorphous pockets, increasing in size from 3 to 10 nm at the side surfaces (Figure 3.8). For this large diameter nanowire, extended amorphisation was not observed even at a dose as high as 1.1×10^{14} ions cm^{-2}.

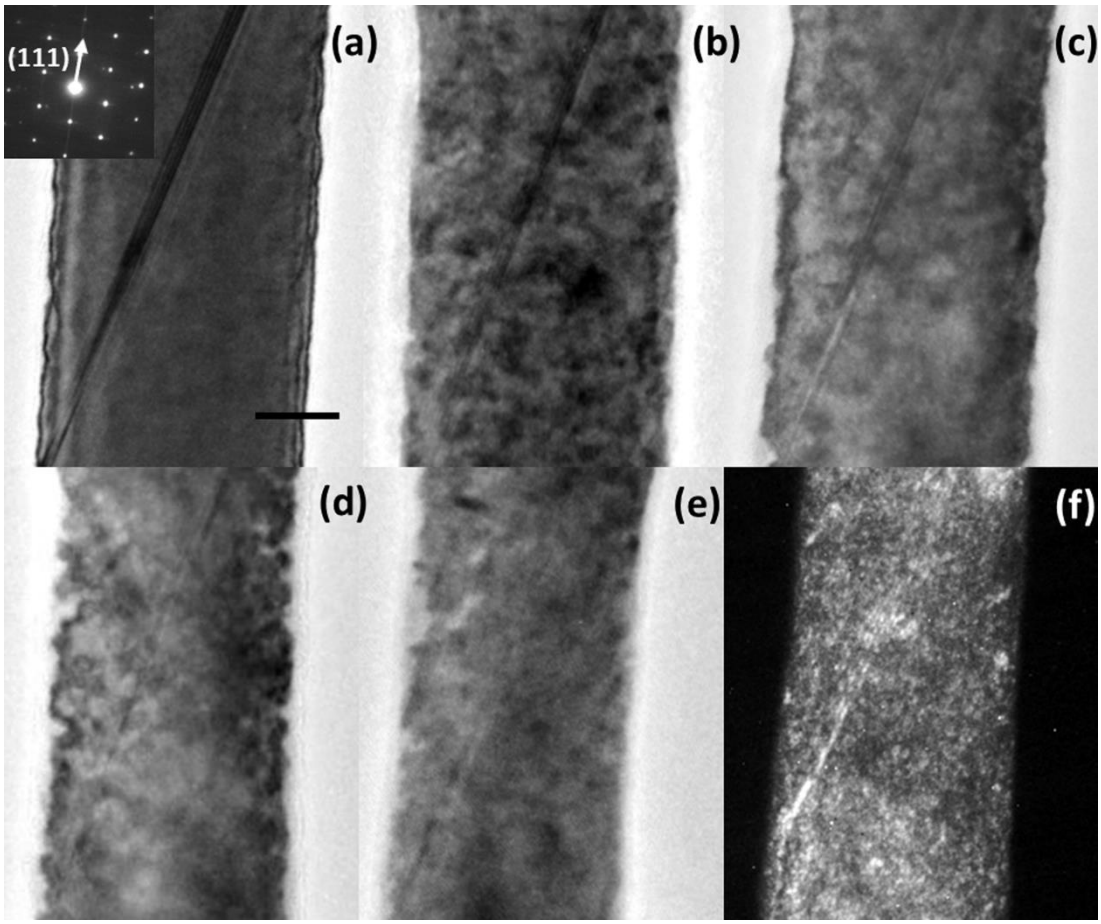

Figure 3.8. Consecutive 30 kV Ga-ion irradiations of a 64 nm diameter Ge nanowire tilted approximately 3 degrees off the [110] zone axis during the exposures. (a) Initial nanowire before irradiation imaged in the [110] zone axis, inset SAED pattern taken at a region without the defect shown. Images of the same area taken in the same zone axis after irradiation, with an increasing fluence of (b) 1.9×10^{13}, (c) 3.8×10^{13}, (d) 5.7×10^{13} and (e) 7.6×10^{13} ion cm^{-2}. All images are at the same magnification. (f) Weak beam dark field image taken under g, 2g = 220 conditions highlights most of the stacking fault defects are still present after irradiation. Scale bar for all images is 20 nm.

Using this method, the evolution of crystal damage was monitored for 10 different nanowires with diameters ranging between 25 and 65 nm for a step-wise increase of the Ga-ion dose at 30 kV from 1.9×10^{13} to 1.1×10^{14} ions cm^{-2}. For the largest (>50 nm) diameter nanowires, crystal damage scaled with Ga-ion fluence but full amorphisation was not observed even at the highest fluence used. For the nanowires in the 30-50 nm range the evolution of the crystal damage was equivalent to the

sequence of images in Figure 3.6. Whereas the nanowires in the 25-30 nm range were almost fully amorphised (with remaining <5 nm crystallites) even at the lowest fluence (1.9×10^{13} ions cm^{-2}) used (Figure 3.9, and Figure 3.10 a and b).

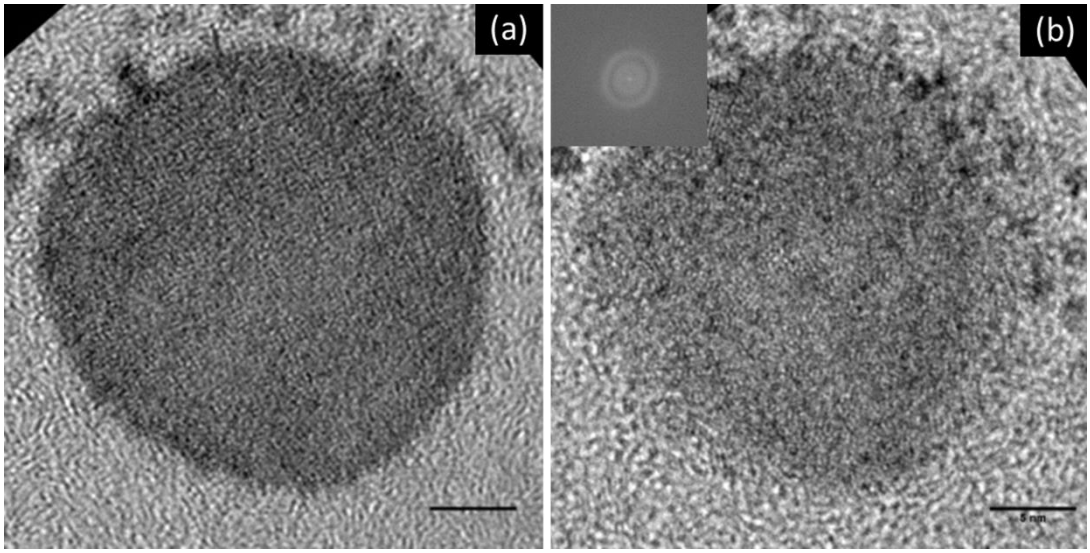

Figure 3.9. (a) and (b) Cross-sectional TEM images at different tilt angles of almost fully amorphised 25 nm nanowire that was subjected to 30 kV Ga-ion implantation at a fluence of 1.9×10^{13} ions cm^{-2}. Initially the nanowire was imaged along the growth direction (image on the left) which was determined by using the electron diffraction of the Si carrier wafer. Image (b) is after 28 degrees tilt in one-direction. Selected area electron diffraction patterns for both nanowires showed attenuated amorphous rings.

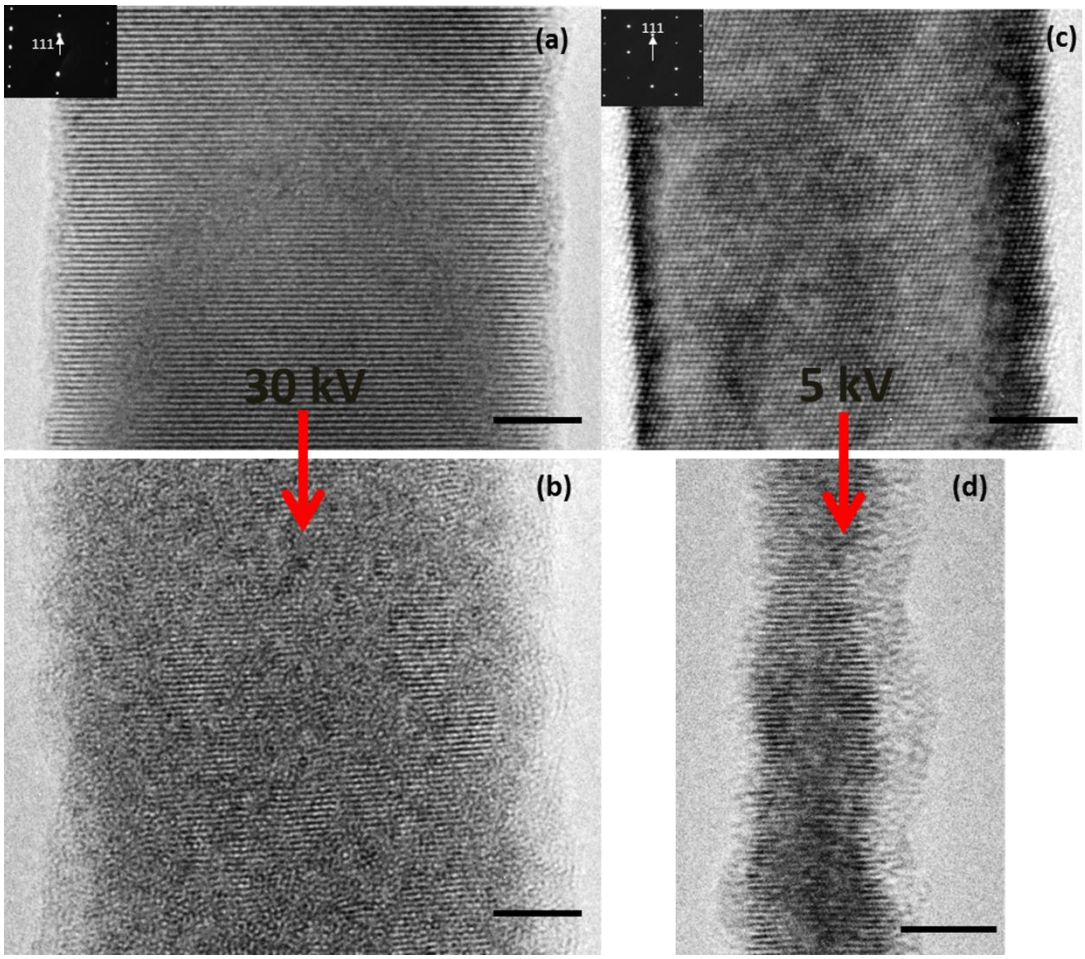

Figure 3.10. 30 kV Ga ion irradiation of a 25 nm diameter Ge nanowire with a beam tilted to about 3 degrees away from the [210] zone direction. **(a)** Before irradiation and **(b)** after irradiation at 1.9 $\times 10^{13}$ ion cm^{-2}. Lattice resolution images are taken close to the [210] zone direction. 5 kV Ga-ion irradiation of a 20 nm diameter Ge nanowire with the beam tilted to about 5 degrees away from the [110] zone direction; **(c)** before irradiation and **(d)** after irradiation at 7.6 $\times 10^{13}$ ion cm^{-2}. Lattice resolution images are taken close to the [110] zone direction. Scale bars in all images are 5 nm.

3.4.3. 5 kV irradiation

To examine the possibility of lower energy implantations and corresponding evolution of the crystal damage in small diameter nanowires (<25 nm), ion implantations at 5 kV were performed. Due to the drastically limited range of interactions of Ga-ions with Ge at 5 kV, the largest number of atom displacements

was predicted from Iradina at approximately 5 – 8 nm from the surface (Figure 3.11). The decreased range due to reduced accelerated voltage is shown for bulk substrates in Figure 3.12. Hence step-wise increase in the ion fluence can be used to build-up crystal damage in analogy to 30 kV implantations in Ge nanowires with diameters >30 nm. Figure 3.13. presents a sequence of images for a 22 nm Ge nanowire subjected to an increasing Ga-ion fluence at 5 kV. Although the damage build-up followed a similar trend as for the 30 kV implantations, i.e. amorphisation starting at the nanowire surface after forming defects, there are some morphological differences. The increase in ion fluence resulted in a reduced nanowire diameter, forming an undulated surface, while the remaining crystalline nanowire interior appeared less distorted with reduced number of domains containing crystal defects, in comparison to the 30 kV implantations. The amorphisation was predominantly localised at the nanowire surface and progressed with gradual decrease of the crystalline core of the nanowire from 20 to 8 nm ± 3 nm for the dose increase of 1.9 to 5.7 $\times 10^{13}$ ions cm^{-2}. A further increase in the ion fluence resulted in further deterioration of the nanowire due to amorphisation and subsequent knock-out damage from the nanowire surface (Figure 3.13 d).

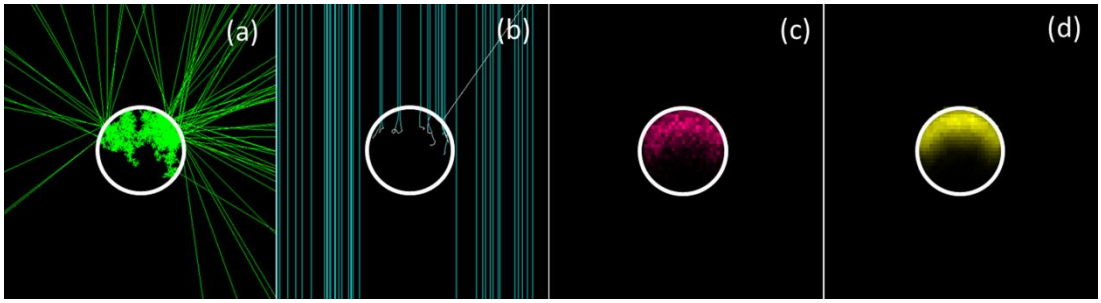

Figure 3.11. Iradina maps of (a) cascade recoils, (b) ion paths, (c) implanted ions and (d) atom displacements based on a cylindrical Ge nanowire with a diameter of 45 nm irradiated by a **5 kV** Ga ion beam orthogonal to the nanowire.

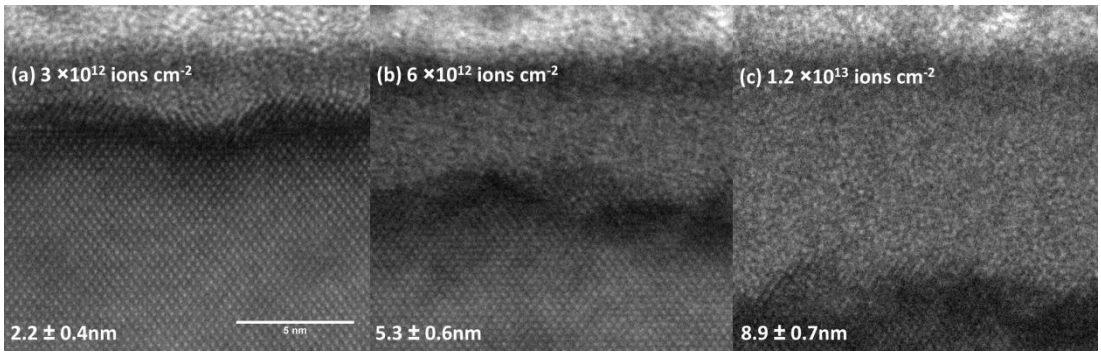

Figure 3.12. Cross sectional TEM of Ge(001) substrate exposed to Ga-ion implantations 7 degrees off the normal direction at increasing fluences at 5 kV. Doses and measured average thicknesses of amorphous layers are given in the insets.

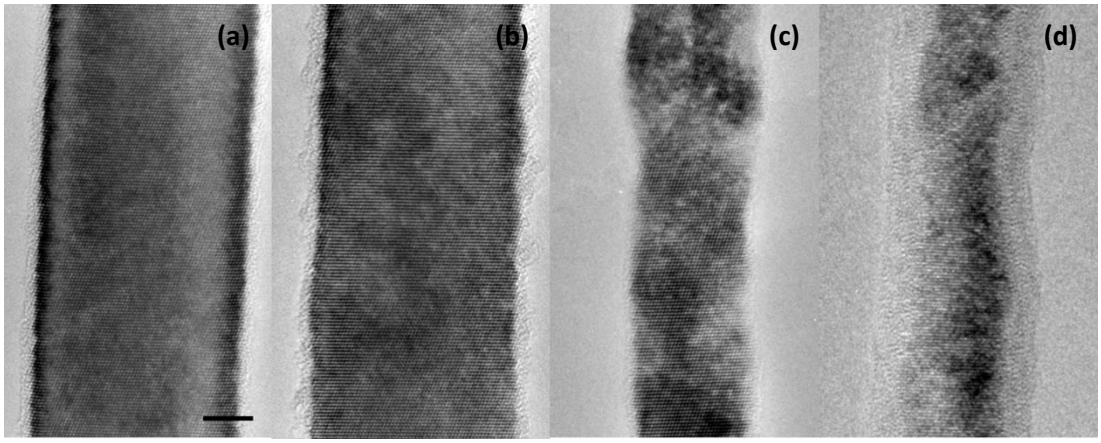

Figure 3.13. Step-wise irradiation of a 22 nm diameter Ge nanowire with a 5 kV Ga-ion beam. (a) Initial nanowire before irradiation imaged close to the [110] zone axis. (b–e) Images of the same area taken in the same zone direction after irradiation with increasing fluence of 1.9×10^{13}, 3.8×10^{13}, 5.7×10^{13} and 7.6×10^{13} ion cm^{-2}. All images were acquired at the same magnification. Scale bar for all images is 5 nm. The direction of the incoming Ga-ion beam during implantation was 5 degrees off the [110] direction.

Similar to flat substrates (Figure 3.4 and Figure 3.12), the depth of crystal damage in the Ge nanowires scaled with the Ga-ion energy and fluence. However, in our study we recorded several differences that are solely related to nanowires. Firstly, the amount and profile of the incurred ion beam damage, at a set energy and fluence, is strongly dependent on nanowire size. The thickness of the damage arc is not conformal; it is much wider at the top of the nanowire cross-section where the ion

beam is normal to the nanowire surface and narrower where the beam is at an oblique or parallel direction. In contrast, flat substrates normally exhibit uniform crystal damage across the whole irradiated surface. This non-conformal damage profile, which is in agreement with the atom displacement maps obtained by iradina, can be understood by looking at the cascade recoils in the nanowires (Figure 3.7). Cascade recoils initiated by the ion beam that are normal to the nanowire surface, i.e. entering at the top/middle of the nanowire, terminate in the bulk of the nanowire after losing their energy. In comparison, the recoils that are localised near the side surfaces (absent in flat substrates) can exit the volume of the nanowire thus diminishing the probability of atom displacements. Specifically at lower energies, e.g. 5 kV, the range of cascade recoils is concentrated in approximately 5 - 8 nm of the nanowire surface. Hence, a large implantation dose will not only induce extended amorphisation in these regions but will also promote greater knock-out damage, as seen in our experiments. The unusual distribution of the cascade recoils in nanowires, in comparison to planar substrates, can be used to explain the observed uneven distribution of amorphisation pockets along the length of the nanowires. Iradina does not predict any variations in the ion interactions in the axial direction of the nanowires as the periodic boundary conditions along this direction are kept constant.

On the other hand, there are aspects of the crystalline to amorphous transition in nanowires that are similar to planar Ge substrates. The formation of the amorphous phase in Si and Ge substrates due to ion bombardment has been associated with the formation of a large number of point defects, including local rearrangement of bonds

(interstitial-vacancy pair (Frenkel) defects), which when reaching a critical density spontaneously relax towards the amorphous phase.[21] At low Ga-ion fluence, lattice distortions in the form of large numbers of clustered point defects[22] and amorphous pockets which at higher fluences merged into extended amorphous regions. The spatial distribution of these regions is dictated by the geometry of the nanowires leading to an unusual, in comparison to planar substrates, distribution of the collision cascades. The transformation process described herein is different to the crystalline to amorphous transitions observed previously by in-situ TEM for single crystalline nanowires under incremental increase of mechanical (bending) stress. During these mechanical influences the formation and movement of dislocations towards the region that is transformed into the amorphous phase has been observed.[23]

3.5. Conclusions

In this chapter, a method for the mechanistic understanding of ion beam induced damage in NWs has been presented. We have described the application of electron microscopy to study the crystalline-amorphous transition in single crystal Ge nanowires upon Ga-ion irradiation. Sequences of images for nanowires of varying diameters subjected to an incremental increase of the Ga-ion dose were obtained. Intricate transformations dictated by a nanowire's geometry indicate an unusual distribution of the cascade recoils in the nanowire volume, in comparison to planar substrates. Our findings will have large implications in designing ion beam doping of Ge nanowires for electronic devices but also for other devices that use single

crystalline nanostructured Ge materials such as thin membranes, nanoparticles and nanorods.

From the analysis of sustained structural transformations upon ion irradiation we establish that there are morphological differences in the Ga-ion beam damage of Ge nanowires suggesting that critical defect densities, corresponding critical damage energy, knock-out damage and dynamic annealing effects are altered as compared to those known for planar substrates. We postulate that the obtained ion implantation data using Ga-ion beams as a probe to induce structural transformations can be used to comprehend the final degree of damage in Ge nanowires but also in other nanostructured Ge materials induced by any heavy ions. Critical damage energy (5eV/at) in Ge substrates is found to be independent of the density of the cascades induced by different ions and energies.[24,25] A critical damage energy density model for ion implantation in nanostructures is important to establish and compare with bulk but this is beyond the scope of this study. A variation in energy, dopant atom, temperature and also dimensions of a nanostructure would be required for a sufficient study.

3.6. References

1 Huang, Y., Duan, X. F., Cui, Y., Lauhon, L. J., Kim, K. H., Lieber, C. M. Logic gates and computation from assembled nanowire building blocks. *Science* 294, 1313-1317, doi:10.1126/science.1066192 (2001).

2 Cui, Y., Duan, X. F., Hu, J. T. & Lieber, C. M. Doping and electrical transport in silicon nanowires. *J. Phys. Chem. B* 104, 5213-5216, doi:10.1021/jp0009305 (2000).

3 Michel, J., Liu, J. & Kimerling, L. C. High-performance Ge-on-Si photodetectors. *Nat. Photonics* 4, 527-534, doi:10.1038/nphoton.2010.157 (2010).

4 Cui, Y., Wei, Q. Q., Park, H. K. & Lieber, C. M. Nanowire nanosensors for highly sensitive and selective detection of biological and chemical species. *Science* 293, 1289-1292, doi:10.1126/science.1062711 (2001).

5 Tian, B., Zheng, X., Kempa, T. J., Fang, Y., Yu, N., Yu, G., Huang, J., Lierber, C. M. Coaxial silicon nanowires as solar cells and nanoelectronic power sources. *Nature* 449, 885-U888, doi:10.1038/nature06181 (2007).

6 Yan, R., Gargas, D. & Yang, P. Nanowire photonics. *Nat. Photonics* 3, 569-576, doi:10.1038/nphoton.2009.184 (2009).

7 Ferain, I., Colinge, C. A. & Colinge, J.-P. Multigate transistors as the future of classical metal-oxide-semiconductor field-effect transistors. *Nature* 479, 310-316, doi:10.1038/nature10676 (2011).

8 Colinge, J. P., Kranti, A., Yan, R., Lee, C. W., Ferain, I., Yu, R., Akhavan, N. D., Razavi, P. Junctionless Nanowire Transistor (JNT): Properties and design guidelines. *Solid-State Electron.* 65-66, 33-37, doi:10.1016/j.sse.2011.06.004 (2011).

9 Fukata, N., Takiguchi, R., Ishida, S., Yokono, S., Hishita, S., Murakami, K. Recrystallization and Reactivation of Dopant Atoms in Ion-Implanted Silicon Nanowires. *ACS Nano* 6, 3278-3283, doi:10.1021/nn300189z (2012).

10 Das Kanungo, P., Koegler, R., Nguyen-Duc, K., Zakharov, N., Werner, P., Goesele, U. Ex situ n and p doping of vertical epitaxial short silicon nanowires by ion implantation. *Nanotechnology* 20, doi:10.1088/0957-4484/20/16/165706 (2009).

11 Colli, A., Fasoli, A., Ronning, C., Pisana, S., Piscanec, S., Ferrari, A. C. Ion beam doping of silicon nanowires. *Nano Lett.* 8, 2188-2193, doi:10.1021/nl080610d (2008).

12 Das Kanungo, P., Koegler, R., Zakharov, N., Werner, P., Scholz, R., Skorupa, W. Characterization of Structural Changes Associated with Doping Silicon Nanowires by Ion Implantation. *Cryst. Growth Des.* 11, 2690-2694, doi:10.1021/cg200108u (2011).

13 Haynes, J. R. & Shockley, W. The mobility and life of injected holes and electrons in germanium. *Phys. Rev.* 81, 835-843, doi:10.1103/PhysRev.81.835 (1951).

14 Duffy, R., Shayesteh, M., McCarthy, B., Blake, A., White, M., Scully, J., Yu, R., Kelleher, A. M., Schmidt, M., Petkov, N., Pelaz, L., Marques, L. A. The curious case of thin-body Ge crystallization. *Appl. Phys. Lett.* 99, doi:10.1063/1.3643160 (2011).

15 Biswas, S., O'Regan, C., Petkov, N., Morris, M. A. & Holmes, J. D. Manipulating the Growth Kinetics of Vapor-Liquid-Solid Propagated Ge Nanowires. *Nano Lett.* 13, 4044-4052, doi:10.1021/nl401250x (2013).

16 Yu, R., Georgiev, Y. M., Das, S., Hobbs, R. G., Povey, I. M., Petkov, N., Shayesteh, M., O'Connell, D., Holmes, J. D., Duffy, R. Junctionless nanowire transistor fabricated with high mobility Ge channel. *Phys. Status Solidi RRL* 8, 65-68, doi:10.1002/pssr.201300119 (2014).

17 Borschel, C. & Ronning, C. Ion beam irradiation of nanostructures - A 3D Monte Carlo simulation code. *Nucl. Instrum. Methods Phys. Res., Sect. B* 269, 2133-2138, doi:10.1016/j.nimb.2011.07.004 (2011).

18 Ziegler, J. Particle interactions with matter, <http://www.srim.org/>

19 C Borschel, C. R. Ion beam irradiation of 3D nanostructures-a new Monte Carlo simulation code, <www.iradina.de> (2011).

20 Stiegler, J. M., Tena-Zaera, R., Idigoras, O., Chuvilin, A. & Hillenbrand, R. Correlative infrared-electron nanoscopy reveals the local structure-conductivity relationship in zinc oxide nanowires. *Nat. Commun.* 3, doi:10.1038/ncomms2118 (2012).

21 Claverie, A., Vieu, C., Faure, J. & Beauvillain, J. Cross-sectional high-resolution electron microscopy investigation of argon-ion implantion-induced amorphization of silicon. *J. Appl. Phys.* 64, 4415-4423, doi:10.1063/1.341264 (1988).

22 Rettig, R., Steuer, S. & Singer, R. F. Diffusion of Germanium in Binary and Multicomponent Nickel Alloys. *J. Phase Equilib. Diffus.* 32, 198-205, doi:10.1007/s11669-011-9853-6 (2011).

23 Decoster, S. & Vantomme, A. Implantation-induced damage in Ge: strain and disorder profiles during defect accumulation and recovery. *J. Phys. D: Appl. Phys. 42*, 165404, doi: 10.1088/0022-3727/42/16/165404 (2009).

24 Claverie, A., Koffel, S., Cherkashin, N., Benassayag, G. & Scheiblin, P. Amorphization, recrystallization and end of range defects in germanium. *Thin Solid Films* 518, 2307-2313, doi:10.1016/j.tsf.2009.09.162 (2010).

25 Yeh, M. S., Lee, Y. J., Hung, M. F., Liu, K. C. & Wu, Y. C. High-Performance Gate-All-Around Poly-Si Thin-Film Transistors by Microwave Annealing With NH3 Plasma Passivation. *IEEE Trans. Nanotechnol.* 12, 636-640, doi:10.1109/tnano.2013.2265778 (2013).

Chapter 4

Epitaxial post-implant recrystallization in germanium nanowires

4.1. Abstract

As transistor dimensions continue to diminish, techniques for their fabrication need to be adapted. In particular, crystal recovery post ion implantation is required due to destructive ion bombardment inducing crystal damage including amorphisation. In this chapter, we report a study on the post-implant recrystallization in Ge nanowires (NWs) following gallium (Ga) ion doping. In this work a variation of NW diameters and orientations were irradiated and annealed in situ to investigate the mechanism of recrystallization. An added complication of misorientation of crystal grains increases the complexity of crystal recovery for suspended NWs. We show that when the misorientation is prevented, by leaving a crystal link between two seeds and providing a rigid support, recrystallization occurs primarily via solid phase epitaxial growth (SPEG). Finally, we demonstrate that top-down fabricated Ge NWs on insulator can be recovered with no extended defects. This work highlights both experimentally and through molecular dynamic simulations the importance of engineering crystal recovery in Ge NWs which may have potential for next-generation complementary metal-oxide semiconductor (CMOS) devices.

4.2. Introduction

Accurate control of doping is vital when fabricating NW FETs[1, 2] and other NW devices such as sensors,[3,4] photovoltaics[5] and photonic devices.[6] In inversion mode nanowire FET devices, variability issues are attributed to non-uniform dopant distribution.[7] There has been a lot of research on the control of dopant depth as well as concentration which has seen the development of new doping techniques such as

molecular layer doping and single ion doping.[8-11] Ion beam doping is currently common practice in industrial microprocessing, but transferring this technique to nanostructures is challenging. For ion beam doping the dopant atom (and resulting cascade recoils) can be easily lost/ejected if the path of the dopant atom leaves the nanowire volume and hence the energy of the ion beam needs to be selected depending on the desired depth of implantation. Moreover, the destructive nature of ion beam doping due to ion bombardment and resultant cascade recoils within the NW volume requires a crystal recovery step.[12] An increase in conductivity has been demonstrated in grown Ge NWs irradiated with a Ga ion source up to a fluence of 6.25×10^{12} cm^{-2} without an activation (annealing) step.[13] Above this fluence, a drop in conductivity is observed and is attributed to amorphisation. However, higher implantation fluences are required to achieve the proper function of advanced transistors such as junctionless nanowire transistors (JNTs)[14] and photonic devices.[15-16] Unfortunately, full recovery of irradiated nanostructures is not easily achievable.[12, 17]

Thermal annealing is the final step required to activate the implanted dopant atoms and recover the crystallinity of the nanowire. Recrystallization occurs via two competing mechanisms; solid phase epitaxial regrowth (SPER) and random nucleation and growth (RNG).[25] It has been observed, like silicon, the germanium [111] direction is the least favourable for crystallization and {111} stacking faults are common.[29-30] It has been predicted by molecular dynamics simulations that the recrystallization process in nanowires can be largely influenced by the presence of interfaces which propagate the formation of stacking fault defects.[31] Simulations of

the defect dynamics have also shown that such defects are pinned at the nanowire surface and can be a result of overlapping growth fronts.

There has been an extensive body of research investigating the recrystallization of bulk Ge and some progress in recent years on Si and Ge nanostructure recrystallization post ion irradiation.[12, 17-22] The high surface-area to volume ratio in nanostructures results in a greater sensitivity to surface roughness and possible over-layers.[23,24] Therefore, formation of dangling bonds, and by extension stacking faults, are prevalent during regrowth.[12, 17] The bulk material acts as a seed for the recrystallization of fin structures and nanopillars via SPEG, however, a polycrystalline region is observed to occur at the top of the structure (i.e. not in proximity to the bulk crystal seed).[20, 25] This polycrystalline region is likely due to the predominance of RNG. NWs with no contact to a bulk substrate which undergo ion irradiation along its entire length, and hence experience full amorphisation, lack the seed which facilitates SPEG and hence recrystallization occurs solely via RNG. However, recrystallization of Ge fin structures has been shown to achieve full recrystallization via SPEG with high defect density at the top of the structures.[17] Another undesirable factor which affects the recrystallization of NWs is loss of rigidity (bending) with ion bombardment induced amorphisation. A misorientation between two crystalline fronts results in a crystal mismatch and hence defect formation.[26] It has been shown that NWs can be bent in a desired direction depending on the energy and the direction of the incoming ion beam.[21, 27-28] Bending occurs to minimize stress within the NW due to amorphisation. The stress may be due to formation of a crystalline/amorphous (c/a) interface,[21] a combination of

compressive and tensile stress due to formation of vacancies and interstitials,[28] or it may be due to densification during irradiation.[27] Importantly, the influence of the topology of the c/a interface and the rigidity (bending) of the NW on high temperature regrowth has not been investigated.

An understanding of the recrystallization process will aid in the engineering of defect-free highly doped nanostructures. Experimental data coupled with modeling calculations have already shown the dependence of crystal orientation for the rate of recrystallization.[17,32-34] In this work, a detailed investigation into Ge NW recrystallization post Ga-ion irradiation by in situ TEM combined with molecular dynamics calculations is presented. The main aim of this study is to devise a method to reduce residual defects after recrystallization in Ge NWs. By minimizing the contribution of RNG and the role of misorientation in the recrystallization fronts due to NW bending, a predominately SPEG mechanism and defect-free regrowth is promoted. It is demonstrated that NW partial amorphisation allows for single crystal seed remnants which facilitate SPEG recrystallization as growth templates. For the investigation of the role of misorientation of crystal seeds for regrowth, NWs were encapsulated in an external amorphous matrix on a flat wafer support to preserve their rigidity during irradiation. Combining these approaches, post-anneal Ga-ion implanted Ge NWs (with implantation doses up to 4.8×10^{15} cm^{-2}) with no apparent stacking fault defects were demonstrated on buried oxide.

4.3. Experimental Procedure

4.3.1. Concurrent imaging platform and irradiation

The method for platform preparation, concurrent imaging and doping of NWs using a dual beam FIB/SEM, has been described previously in Chapter 2 section 2.3.3.[12] For accurate selective area doping within a section of single NW it is important to align the electron and ion beam coincident point precisely as the exposure needs to be done "blind" with the aid of the electron beam for navigation. A 30 keV Ga ion beam, operating at a current of 9.6 pA, was used for all implantation experiments presented here. A rectangle area is defined for the irradiations. The length of the NWs irradiated varied between 200 nm and 1 μm. The typical area irradiated was 200 nm (along length of NW) × 5 μm. A minimum dose of 1.9×10^{13} ions cm^{-2} was used in the experiments presented here. Small areas can be accurately irradiated with Ga ions without introducing impurities to the surrounding structures by using a well-aligned FIB.

4.3.2. Irradiated EBL defined GeOI Nanowires

An overview of the experimental procedure for the irradiation and imaging of NWs is depicted in a schematic in Figure 4.1. NWs deposited on silicon nitride (SiN) membranes do not require any additional steps for observing the damage incurred and subsequent in situ TEM annealing (Figure 4.1 a).[12] For the NWs on a substrate, grown NWs deposited on a Si/SiO_2 chip via dry transfer from the growth substrate or EBL defined NWs on GeOI (germanium on insulator) were used.[35-36] In order to observe the in situ TEM recrystallization along the NWs on substrates, the structures need to be extracted with the underlying substrate

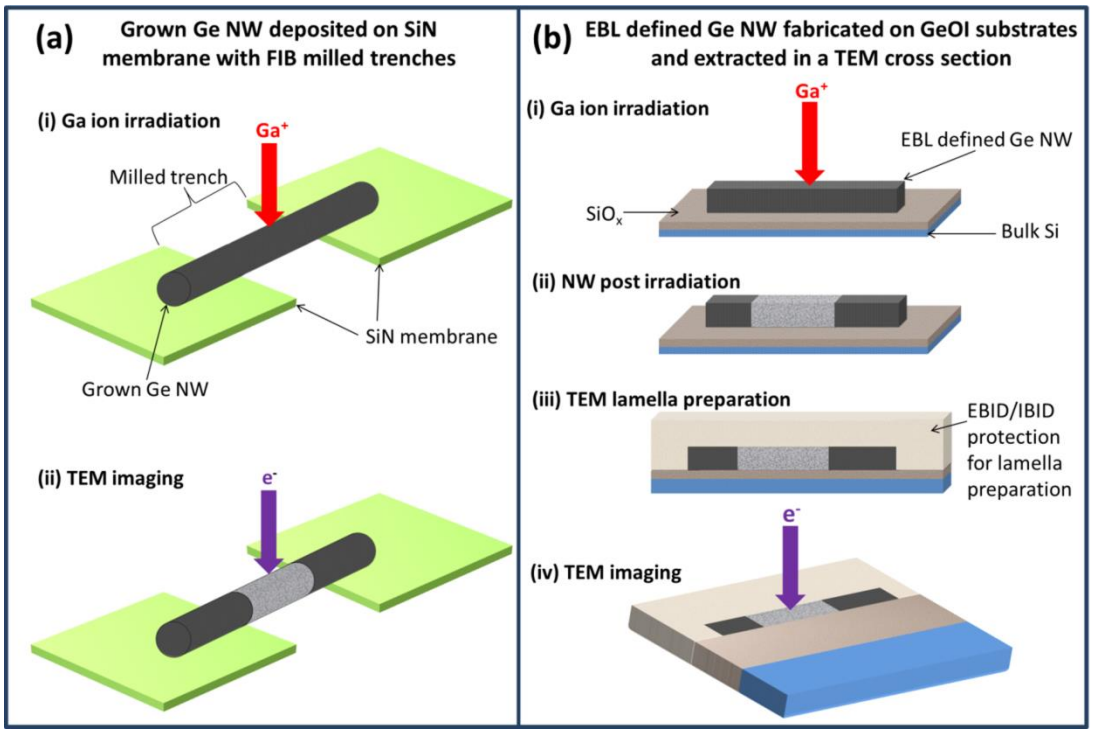

Figure 4.1. Schematic overview of sample preparation and imaging for (a) a nanowire on pre-patterned SiN membrane and (b) EBL defined NW from on GeOI substrate.

(Figure 4.1 b iii). This is done via a non-typical inline FIB lift-out technique along the NW length (Figure 4.2). For all NWs imaged on SiN membranes, the direction of the ion beam (red arrow) during irradiation is nearly parallel to the electron beam (purple arrow) when imaged in the TEM (Figure 4.1 a). However, for NWs extracted from a substrate (Figure 4.1 b) the direction of the ion beam is orthogonal to the direction of the electron beam when imaged in the TEM, i.e. we have a side view of the irradiated NW along its length. The GeOI NWs defined by EBL have a height of approximately 50 nm, which is almost twice the range of interactions of the 30 kV Ga-ions in Ge. Therefore, to achieve amorphisation across the NW (the width of the NWs is approximately 40 nm) and avoid ion channeling, very high ion-beam incidence angles (+/- 62°) were used (Figure 4.3).

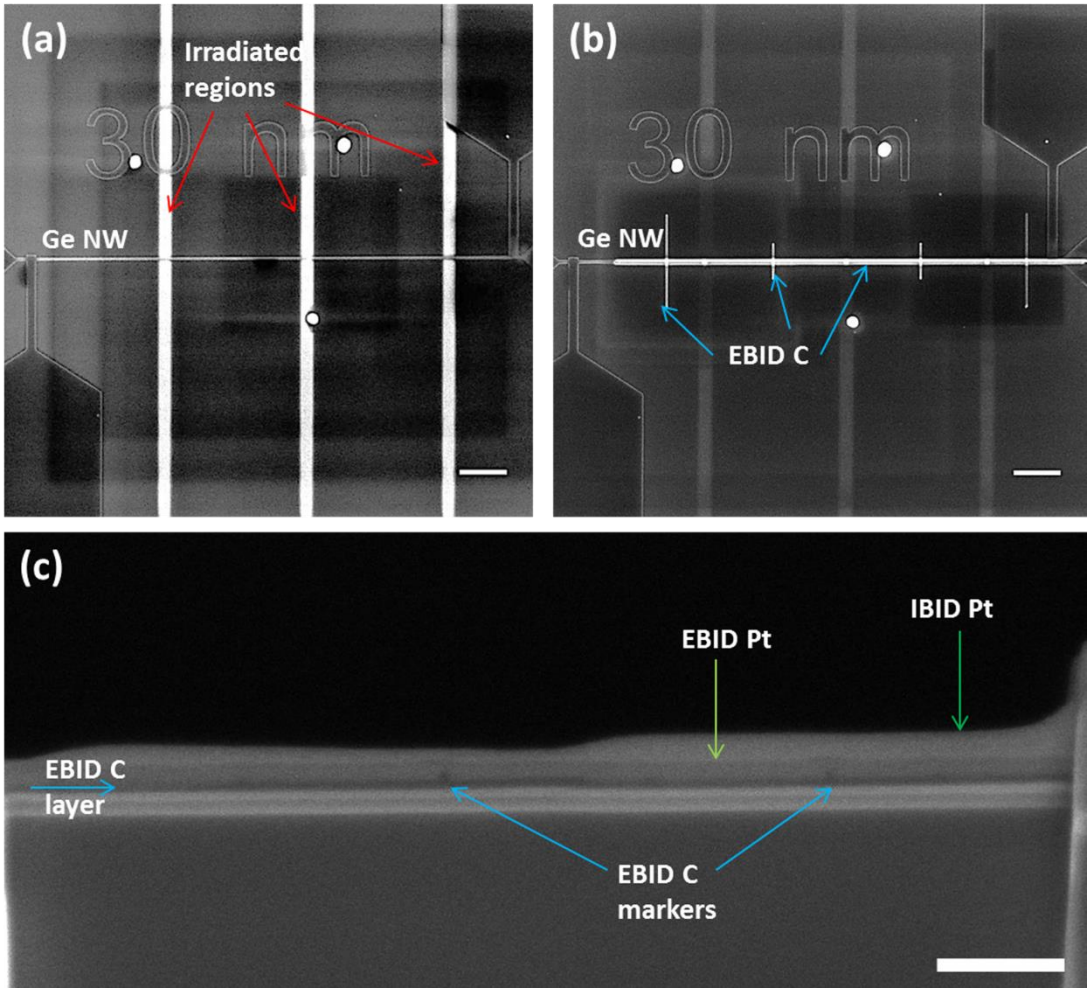

Figure 4.2. Overview of use of EBID carbon for indication of NW exposure during thinning. Scale bar for all images is 1 μm.

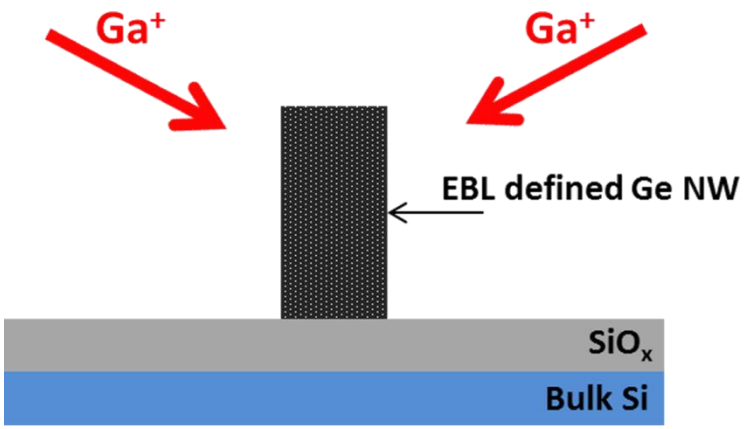

Figure 4.3. Schematic of 62° tilt ion irradiation of EBL defined Ge NW in cross sectional view.

4.3.3. In situ anneal

An in situ Gatan Model 628 single-tilt heating stage TEM holder was used for all anneals presented in this study. The ramp/temperature used for each NW varied. The sample was loaded in the same orientation in the in situ heating stage as it was for HRTEM imaging in the double tilt holder. The in situ heating stage is only capable of single tilt so the sample was tilted as close to the zone axis used for high resolution imaging as possible. For most samples tilting in two directions is required to achieve a zone axis orientation for lattice resolution imaging. The TEM was operated in bright field mode, isolating the direct beam with the objective aperture, to take advantage of the contrast between the crystalline and amorphous regions. Temperature was controlled using a Gatan Model 901 SmartSet hot stage controller. Temperatures varied from 100 – 500 °C (the temperature dispersion control is approximately 0.1 - 0.5 °C, as per the manufacturer's specifications). Images were acquired every minute at the set temperatures.

4.4. Results and Discussion

4.4.1. Recrystallization of nanowire with extensive amorphisation

In order to examine Ge nanowire crystal recovery, the same nanowire from Figure 3.6 was thermally annealed in situ in the TEM at 490 °C. For the initial 20 min of the anneal there is no apparent crystal growth; this could be due to the resolution of our technique. There is likely curing of crystal fronts in the first 20 min. The remaining crystalline islands, identified as the dark regions in Figure 4.4 are approx. 10 nm in

diameter and located, at the back and middle of the nanowire with respect to the direction of the incoming beam as discussed before. These crystallites are the only remaining "seed" available for the crystal regrowth.[41]

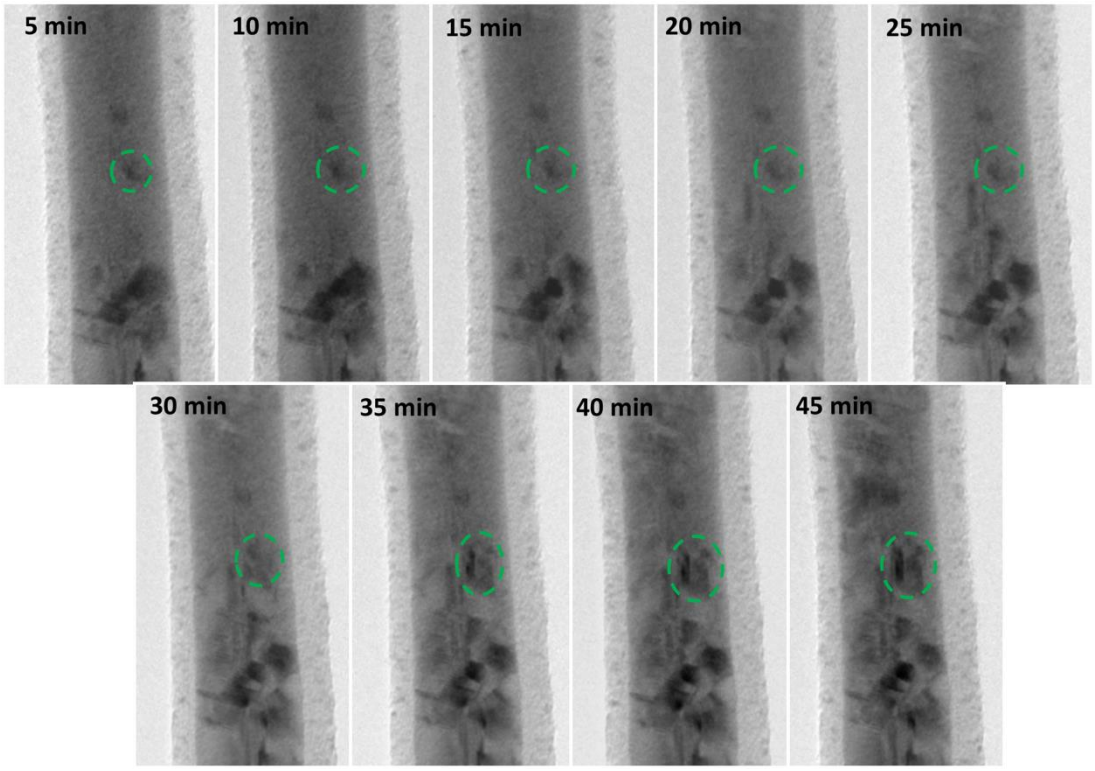

Figure 4.4. In situ anneal of nanowire after implantation at 490 °C for 45 min. There is a large amorphous layer around the NW which is a build-up of contamination (carbon). Green circle highlights an example of a crystallite growth during the anneal.

As seen from the sequence of images in Figure 4.4, the crystallites grow in size after developing recrystallization fronts in the surrounding amorphous region an example is highlighted (green circles) in Figure 4.4. Self-nucleation of crystallites in the amorphous regions can also not be excluded. The final image in Figure 4.4 shows the nanowire after 45 min at 490 °C with corresponding lattice resolution images in Figure 4.5. The crystallisation process resulted in a complex mixture of a large number of extended defects; mainly (111) stacking faults including the recovery of

the stacking fault sequence that existed before the irradiation (see Figure 3.6 (a) for comparison). Although, the majority of the newly formed (111) stacking faults were pinned to the nanowire surface (shown with black arrows), some are parallel to the side wall facets and the initial stacking fault sequence (shown with white arrows). At the regions where these defects overlap a complex pattern is formed (marked with dashed boxes), that can be understood as interference patterns due to overlapping twinned grains.[42]

Interestingly, the majority of the newly formed (111) stacking faults formed an ordered arrangement, similar to stacking faults identified in grown nanowires previously.[29, 43] The crystallisation nucleated from separate crystal islands. The growth results in epitaxial recovery until recrystallization fronts meet, forming a planar defect. Obtained recrystallization data collaborate very well with the molecular dynamics simulations obtained for Si nanowires.[31] The appearance of newly formed defects and recovery of the parent crystal can be attributed to two separate processes: (i) epitaxial propagation of recrystallization fronts (fastest growing in the (110) and (100) directions, as predicted previously[38]) and (ii) the interaction of these fronts when self-intersected and with the nanowire surface. These two processes result in formation of (111) stacking fault defects as well as epitaxial recovery of the rest of the nanowire including pre-existing defects. The fact that the majority of the newly formed stacking faults are pinned to the nanowire surface suggests that the surface plays a predominant role in defect formation.

Significantly, using developed correlative analysis platform, detailed recrystallization data (Figure 4.4) were recorded in the same region of the nanowire

that has been ion-beam damaged (Figure 3.6); hence allowing a direct correlation of structural transformations as result of ion beam damage and thermal annealing.

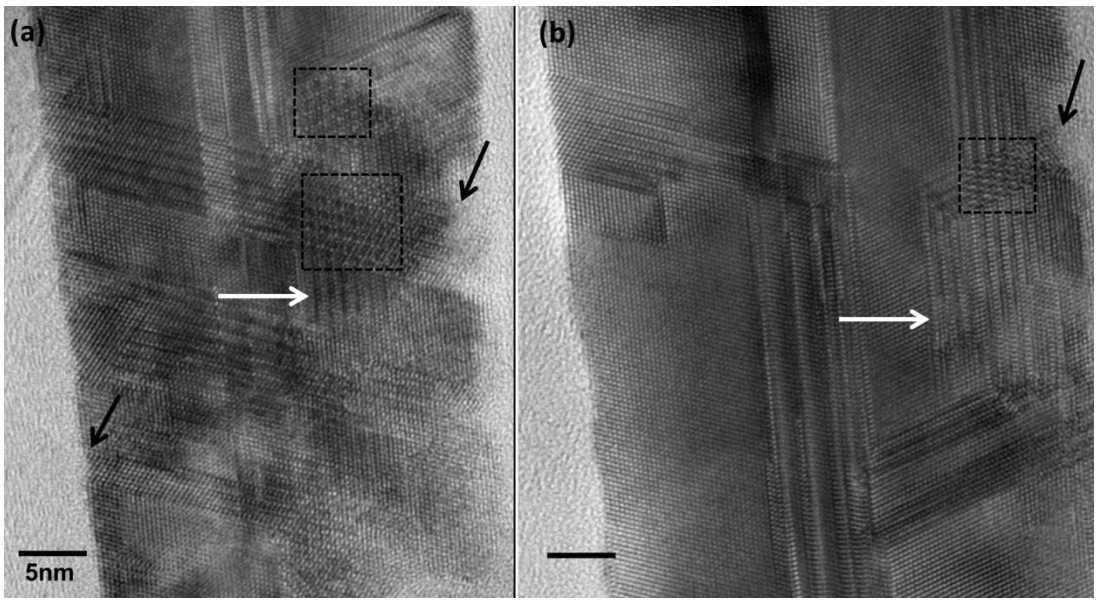

Figure 4.5. Lattice resolution images of nanowire post recrystallization at (a) region of interest showing a high density of stacking fault defects as well as an increase in edge roughness. In another region of the same nanowire (b) a mixture of intrinsic defect curing, high density defect formation and retention of original crystal structure are all observed. Scale bar for image is 5 nm.

4.4.2. Recrystallization of nanowire with partial amorphisation

Another nanowire was irradiated within a selected region to induce amorphisation only within the selected section. Figure 4.6 (a) and (b) show TEM images of a 38 nm diameter <111> grown NW (NW1), imaged along the $[\bar{2}11]$ zone axis, irradiated to induce full amorphisation in a 200 nm section of the NW length. Note that the NW is suspended across an open trench of the SiN membrane. A misorientation is observed between the two crystalline regions, X and Y, separated by the amorphous region which is approximately 205 nm in length. The two crystalline regions were estimated to be at a relative angle (θ) of approximately 3° to each other.[44] Although only a

small region experienced full amorphisation, damage to the NW (partial amorphisation) is observed extending approximately 300 nm either side of the region which was irradiated.

In situ annealing of the NW was observed in the TEM at 400 °C for 83 min and subsequently at 450 °C for 37 min (Figure 4.6 d). An amorphous layer is observed to develop around the NW during the anneal; this is commonly observed during in situ TEM annealing experiments and it is due to carbon-based contaminants desorbed at high temperatures and redeposited due to EBID. Because there was a misorientation of the two crystal seeds only one seed was selected for observation during the anneal process. Within the first 25 min of the anneal, the damaged region, which experienced partial amorphisation and contains many crystallites, developed a continuous crystal growth front (Figure 4.6 (d) at 25 min). The recrystallization appears to occur preferentially along the length and in the center of the NW forming an arrow-head type crystal front. As the crystal front approaches a fully amorphous region, the crystal front flattens, which is expected as growth in the <111> direction is least favorable.[45] The arrow-head recrystallization front is observed again when the temperature is increased to 450 °C (and the rate in turn increases) until a point when the front meets region Z. The recrystallization rate was estimated by measuring the crystalline region from the images acquired during the anneal. See Figure 4.A in the appendix for the analytical procedure adopted to determine crystal regrowth rates with the TEM images acquired during the anneal.

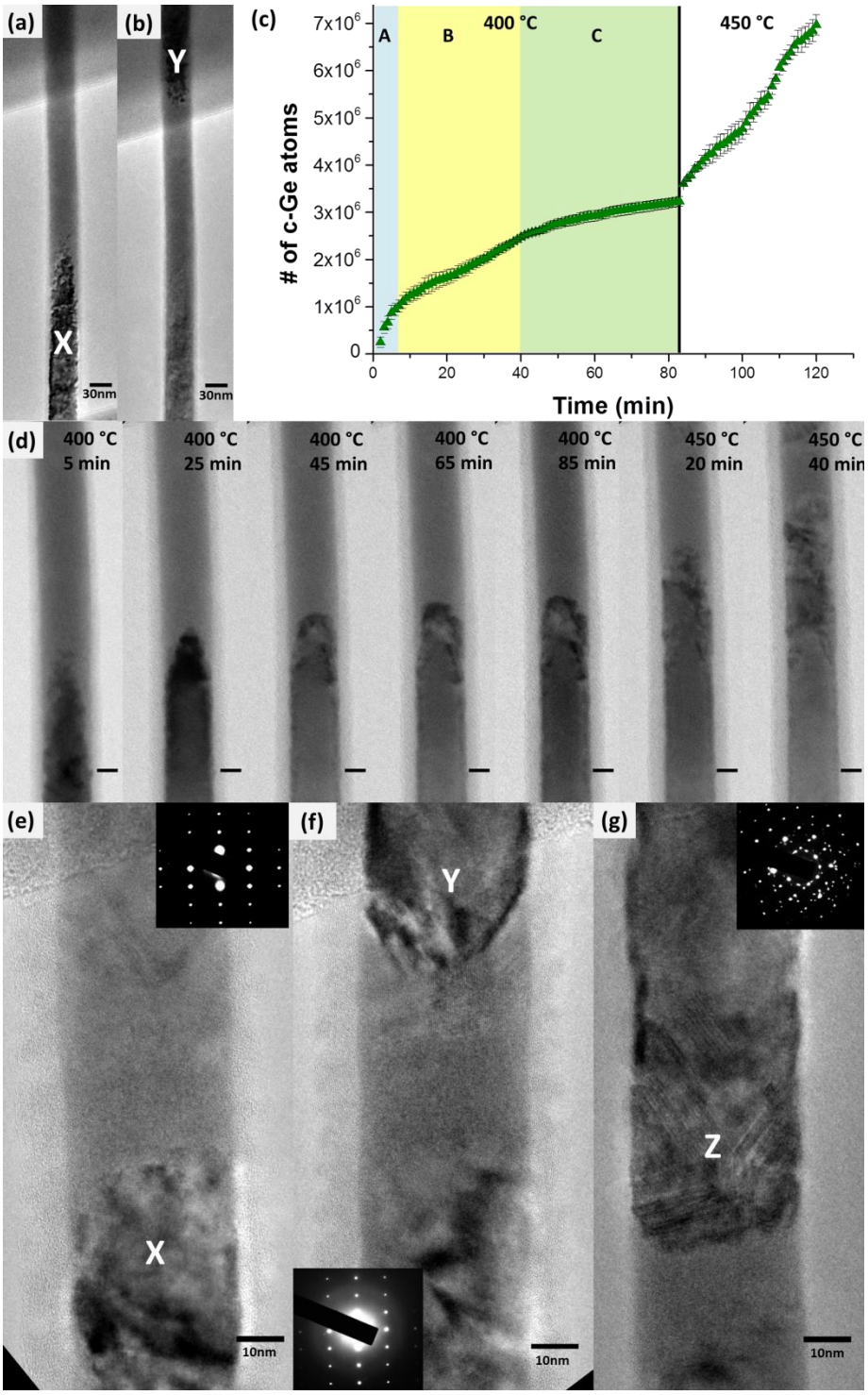

Figure 4.6. NW after irradiation to only part of the length which experiences full amorphisation, (a) and (b). (c) Graphical representation of recrystallization. (d) Selected images from the in situ anneal at 400 °C for 83 min and a further 37 min at 450 °C. Focus issues encountered due to thickness variations and thick carbon layer which developed around NW. Scale bar is 5nm. Before the anneal (a, b) regions X and Y are approximately 3° relative to each other. After the anneal (e-g) regions X and Y maintain the misorientation with a relative angle of 4.2° and the third region Z is at a relative angle of 17° and 14.7° to X and Y, respectively.

A graphical representation of the calculation results is presented in Figure 4.6 (c). The measurements were completed at least three times to achieve a statistically correct overview. It can be observed that a constant rate is not observed for the duration of the 400 °C anneal. The initial recrystallization rate for the first 5 min was approximately 3405 atoms s^{-1} (Figure 4.6 (c) region A), which decreased to 700 atoms s^{-1} for minutes 6-40 (region B) after which the rate dropped again to 280 atoms s^{-1} (region C). The recrystallization rate after the temperature increase to 450 °C rose again to 1600 atoms s^{-1}. The initial high recrystallization rate is postulated to be due to the higher number of mono-oriented and connected crystalline seeds within the partially damaged region which act as preferential growth sites.[46] Similar deviation from linear growth has been observed previously for Ge and particularly for short anneal times for thin amorphous layers and has been attributed to void formation or the introduction of oxygen during the anneal.[45] In another study, it was shown that the rate of SPEG decreased as the growth front approached within 0.3 μm of the surface and has been attributed to H infiltration and this has a higher impact on Ge than Si SPEG.[47]

Figure 4.6 (e), (f) and (g) show HRTEM images of the recrystallized NW after annealing. The mismatch of the two crystal planes was retained with the formation of a highly defective region between the two crystal grains, region Z. The relative angles for the crystal grains imaged were calculated; $\theta_{XY} = 4.2°$; $\theta_{YZ} = 17°$; $\theta_{XZ} = 14.7°$. The region between grains X and Y appears to be amorphous but when imaged in the zone axis for Z it is clear that it is in fact crystalline. The formation of the defective grain (Z) is highly irregular. The smallest possible angle between

$< 211 >$ and $< 011 >$ is 30°. The two original grains, X and Y, are both in the $[\bar{2}11]$ zone axis and C is in the [011] zone axis. The relative angle between $< 211 >$ and $< 011 >$ directions were calculated from

$$cos\ \theta = \frac{(hH+kK+lL)}{\sqrt{(H^2+K^2+L^2)(h^2+k^2+l^2)}}$$

where the two axes are (hkl) and (HKL). A plausible explanation for this unexpected grain formation is RNG in the strained region. Regions X and Y have maintained the original crystallographic relationship with a misorientation between the two regions. However, region Z has no rational crystallographic relationship with either regions X or Y indicating a polycrystalline growth due to RNG. It has been shown that a NW can be bent in a desired direction upon FIB exposure and maintains the bent shape even after high temperature annealing.[21, 27-28] The result for NW1 correlates well with results on Si NW recrystallization published by Pecora et al. in which NWs were irradiated and experienced bending.[21] Some NWs, presented by Pecora et al., straightened during recrystallization and were single crystalline, albeit partially defective, but NWs which remain bent were polycrystalline. Summarizing the mechanism of recrystallization for the suspended Ge NW (Figure 4.6) two different regrowth mechanisms can be identified (single crystalline vs polycrystalline) with SPEG resulting in the single crystalline regrowth from regions X and Y, and RNG resulting in the polycrystalline regrowth in region Z.

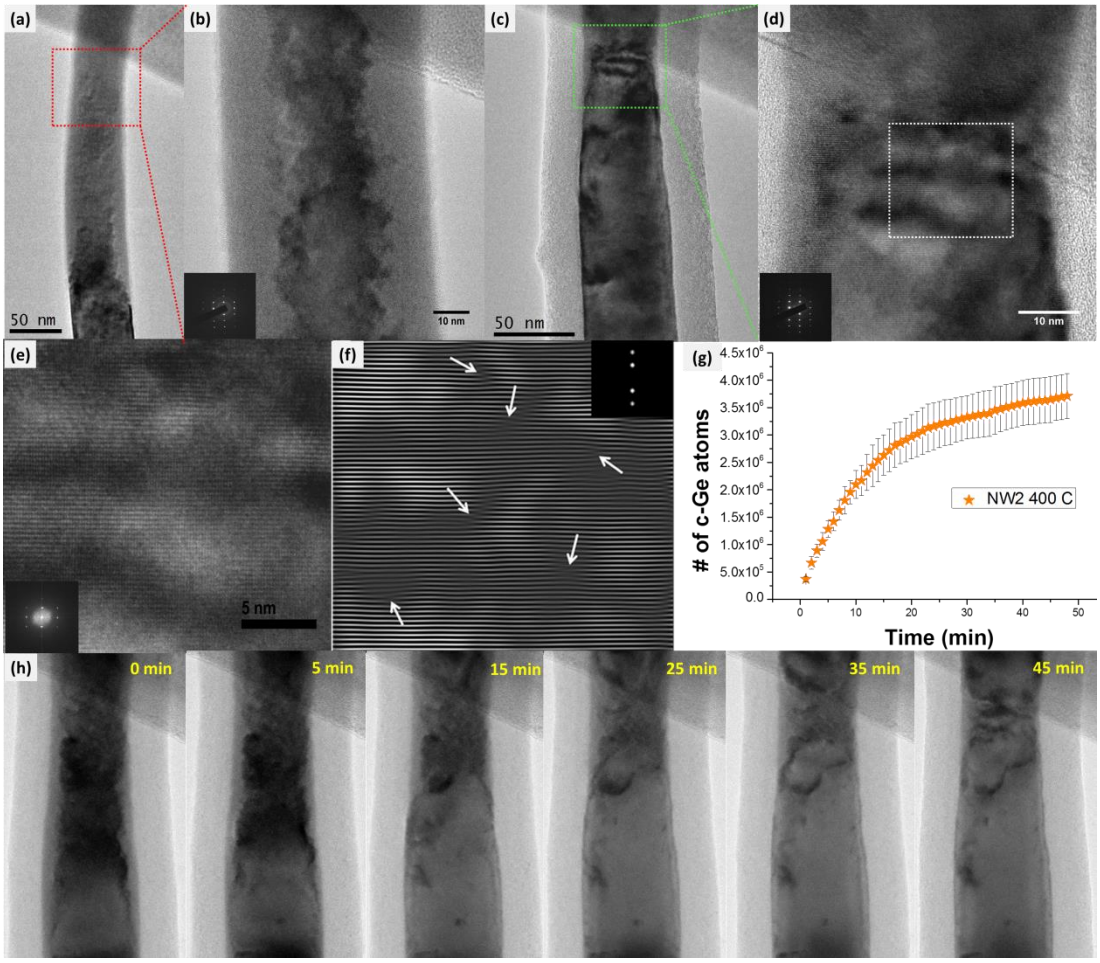

Figure 4.7. NW2 (a) and (b) partially irradiated with remaining crystal in irradiated region imaged along the $[\bar{2}11]$ zone axis. (c) and (d) after annealing at 400 °C for 47 min. (e) A high resolution lattice image of region identified in (d). (f) Inverse of <111> reflections from FFT of (e). White arrows indicate misfit dislocations. (g) Graphical representation of recrystallization. (h) Selected images from the in situ anneal at 400 °C for 47 min.

A (larger) 56 nm diameter <111> grown NW also imaged in $[11\bar{2}]$ zone axis was irradiated to induce amorphisation but retain a crystalline "backbone" for a section of the NW across an open trench of a SiN membrane (Figure 4.7) . A cross section of another irradiated 50 nm <111> grown NW has been presented in Figure 3.5 (c). Depending on the energy of the ion beam, the range of the ions can be estimated.[48] In this case, a 30kV Ga ion beam does not have enough energy to penetrate and induce cascade recoils through the whole diameter of the NW and hence a crystal region

remains along the back of the NW. This backbone provides a support for the NW, maintaining some rigidity by preventing misorientation and allowing a direct link between the two non-irradiated regions. It is observed in Figure 4.7 (a) that the NW experiences some bending. The only way to avoid this bending for a grown NW is to provide a flat and stable support, e.g. on Si_3N_4 or SiO_2 substrate as we show below. The thermal anneal of NW2 was observed in situ in the TEM at 400 °C for 47 min (Figure 4.7 h). An estimation of the recrystallization rate is represented graphically in Figure 4.7 (g). When recrystallization occurred in the NW1 in Figure 4.6 there was a clear interface between the crystalline and amorphous regions. In Figure 4.7 (a) and (b), the volume of the amorphous region is difficult to quantify based on the images alone. Thus, the estimation of the recrystallization rate calculated for NW2 is an underestimation of the rate and volume of Ge recrystallized. The initial recrystallization rate for the first 15 min is estimated to be 3130 atoms s^{-1}. HRTEM images post-anneal show a monocrystalline NW (Figure 4.7 c-e). No stacking fault defects are observed along the growth direction of the NW imaged in the $[11\bar{2}]$ zone axis. From the reconstructed FFT (Figure 4.7 f), the presence of dislocations in the crystal can be identified (white arrows), these are likely to be stacking faults along the $(\bar{1}11)$, $(1\bar{1}1)$ and/or $(11\bar{1})$ planes. To confirm these "hidden defects" it would be required to tilt to another zone axis such as the $[011]$ zone axis.[49]

In an attempt to reduce and understand the influence of strain experienced by a suspended NW, a NW deposited on a substrate was irradiated, encapsulated and recrystallized in situ (Figure 4.8) (NW3). The 64 nm diameter, <112> grown NW containing intrinsic $(11\bar{1})$ stacking faults along the NW length was imaged along the

[$1\bar{1}0$] zone axis. NW3 was irradiated on a Si/SiO_2 substrate and then extracted as an inline FIB cross-section, i.e. along its length (Figure 4.2). In this method, the NW is encapsulated in EBID carbon. A section approximately 500 nm along the NW was defined for irradiation but a length of approximately 600 nm experienced amorphisation (Figure 4.8). As observed in Figure 4.8 (a), only partial amorphisation across the NW diameter is achieved leaving a continuous backbone similarly to the NW2. The embedded NW was annealed in situ at 400 °C for 30 min (Figure 4.8 g). It is clear from the images taken in situ that the recrystallization occurs epitaxially, i.e. via a SPEG mechanism. Two major crystal fronts can be identified; one in the [$11\bar{1}$] direction orthogonal to the NW long axis, which is the larger growth front, and the other growth front in [112] direction, i.e. the NW growth direction. HRTEM images post-anneal show a mixture of defect curing, intrinsic defect propagation as well as the appearance of newly formed (extrinsic) defects (Figure 4.8 e). Some of the extrinsic defects formed are ($\bar{1}11$) stacking faults in the same direction as the intrinsic defects (along the NW length) and the rest are {111} stacking faults which are pinned to the NW surface. Interestingly, the region towards the middle of the amorphous area recrystallized with the formation of mainly extrinsic stacking faults. The intrinsic defect propagation is limited to the edges of the damaged region. The recovery of intrinsic stacking faults from a fully amorphous structure, i.e. the phenomenon of crystal memory, an apparent memory of an amorphised material which retains some ordering and hence fully retains the crystal structure upon recrystallization without the assistance of an epitaxial template, has not been observed.

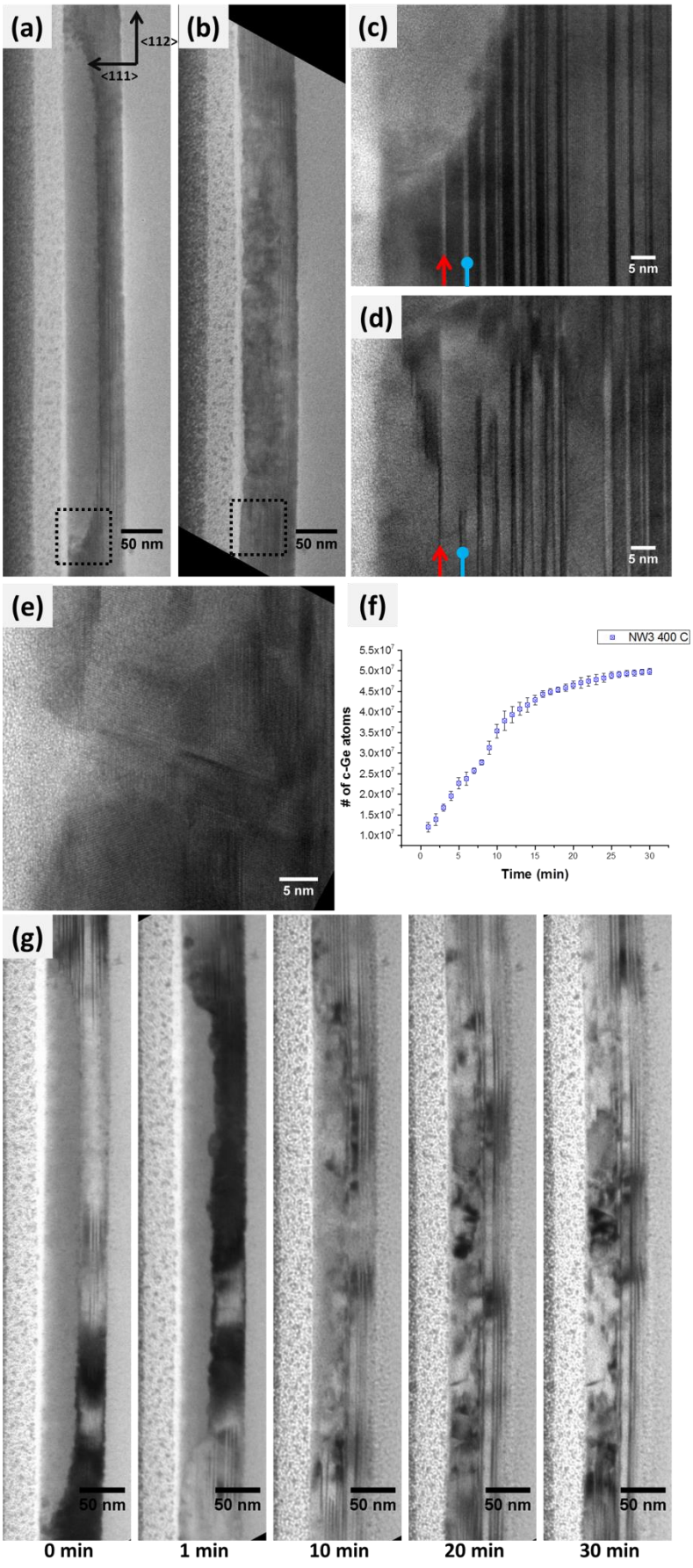

Figure 4.8. <112> grown NW3 (a) after irradiation and (b) after anneal at 400 °C for 30 min. (c) and (d) are higher resolution images from the marked regions in (a) and (b) respectively. The red arrow indicates SF1 and the blue pin indicates SF2. (e) HRTEM of recrystallized NW3 from middle of damaged region post-anneal. A combination of {111} stacking faults pinned to the surface, stacking faults parallel to intrinsic defects and defect free regions are observed. (f) Graphical representation of Ge recrystallization rate during the anneal of NW3. (g) Selected images from the in situ anneal of NW3 at 400 °C for 30 min. Changes in contrast of the NW are observed during the anneal due to drift moving the sample further away from the zone axis.

However, seeding of parallel stacking faults through defects in the Au seed and their propagation along the <112> grown Ge NWs has been reported.[29] For stacking fault 1 (SF1) (indicated with red arrows in Figure 4.8 c), there is a damaged region which has not experienced full amorphisation, this is due to cascade recoils being ejected from the NW volume.[12, 19] A broadening is observed for SF1 grain in Figure 4.8 (d) post-anneal. This type of migration has been previously observed where it was attributed to the slower growth rate in <111> than in the <115> direction, resulting in a migration of the twin grain in a stepwise fashion.[50] At stacking fault 2 (SF2) (indicated with blue pins in Figure 4.8) the c/a interface is sharp with little or no ordering present. The bulk crystal grain engulfs the stacking fault and effectively prevents propagation of the stacking fault in the <112> direction. This illustrates the importance of the roughness of the c/a interface. An initial recrystallization rate of 39046 atoms s^{-1} was estimated for the first 15 min based on the images from the in situ anneal. As observed for the previous two anneals, the rate begins to level off as the NW recrystallizes fully.

A Ge NW (NW4) was defined via EBL from a (001) GeOI wafer along the [100] direction. The etched NW4 with rectangular cross-section (width 40 nm, height 55 nm) was irradiated and annealed in situ, imaged close to the [010] zone axis (Figure 4.9). The irradiation was done at high incidence angles (+/-62°, i.e. -10° tilt of the stage) to induce amorphisation as the width of the NW is less than the height of the Ge (Figure 4.3). Annealing was initiated at 100 °C with incremental increases in

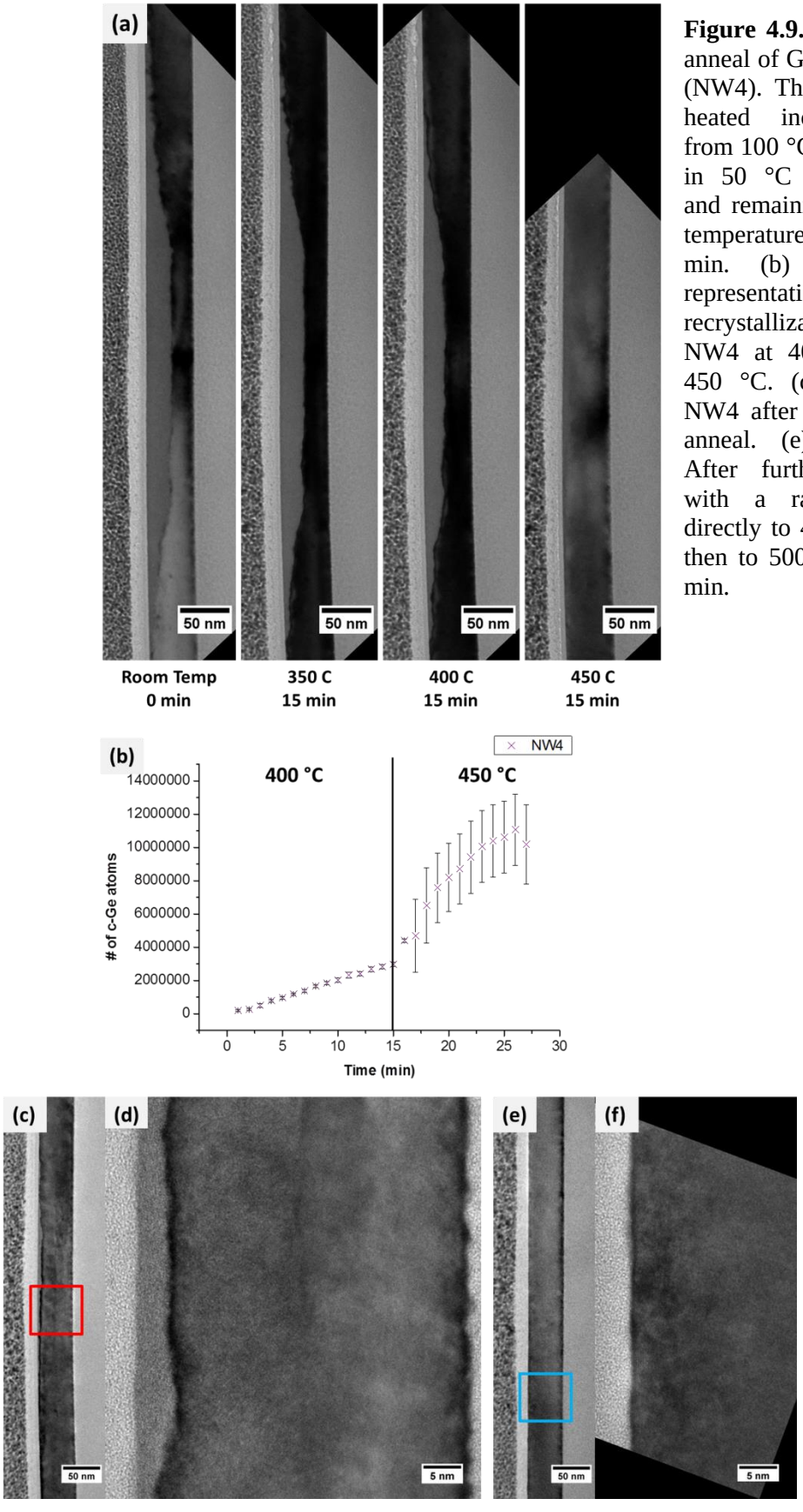

Figure 4.9. (a) In situ anneal of Ge[100] NW (NW4). The NW was heated incrementally from 100 °C to 450 °C in 50 °C increments and remaining at each temperature for 15 min. (b) Graphical representation of recrystallization of NW4 at 400 °C and 450 °C. (c) and (d) NW4 after the in situ anneal. (e) and (f) After further anneal with a rapid ramp directly to 400 °C and then to 500 °C for 10 min.

steps of 50 °C every 15 min. Notable recrystallization was only observed from 400 °C. Recrystallization rates were extracted from the in situ images for 400 and 450 °C, approximately 3480 and 18570 atoms s^{-1}, respectively (Figure 4.9). The initial heating rate affects the recrystallization temperature observed.[51] Estimation of the recrystallized volume is more accurate as the cross sectional shape of GeOI NW is rectangular. Similar to NW3, two recrystallization fronts can be identified; predominantly along the [001] direction. A final anneal with a direct ramp to 400 °C followed by a temperature increase 500 °C was done to fully recover the crystallinity of the NW. Based on the HRTEM images acquired, in Figure 4.9 (f), no stacking fault defects were observed and this is attributed to the SPEG.

Activation energies (E_a) in the range between 2.0 eV and 2.19 eV have been previously reported for Ge recrystallization.[45,52-55] To calculate the E_a of recrystallization in a NW, the rate of recrystallization of two different temperatures for the same NW were used, the calculation is described in the Supporting Information. For this report, NW4 was used to calculate a crude estimation of the E_a of recrystallization to be approximately 1.4 eV. Only this NW was used for the E_a calculation due to the slow ramp rate for both temperatures (400 and 450 °C) for the calculation and the abundant amorphous "sink" for both anneal temperatures, i.e. less than 50% of the volume recrystallized at the 400 °C. The contribution of the electron beam was not accounted for in the calculations of activation energy. The anneal of NW4 was initiated at 100 °C with recrystallization only observed from 400 °C. This would suggest that the electron beam had little or no effect on the recrystallization. However the oriented attachment of crystals and further extended growth from

amorphous phase has been observed in systems such as suspensions of NPs[56] and by us in ALD (atomic layer deposition) deposited hafnia films (unpublished results). The temperature distribution in an electron transparent metal sample has been measured by EELS to obtain nanoscale maps of the temperature distribution when metal circuits are electrically loaded.[57] This is done by looking into changes in the plasmon band at different temperatures along the metal lines. Possibly this can be extended to calculating the activation energy of various thermally associated reactions at the nanoscale. The E_a obtained in MD simulations was 0.92 eV which confirms a slightly smaller value in comparison to simulations of planar recrystallization, where the activation energy was E_a=1.09 eV.[38]

A notable difference between irradiated NWs and bulk substrates is the shape of the c/a interface. In a bulk substrate, the c/a interface may be rough but the interface is relatively flat so recrystallization occurs primarily in one direction. For a grown NW with a remaining crystal backbone the interface has two extra dimensions to consider – the crystal fronts created at the edge of the irradiated region and the curved cross sectional interface. Although the crystal backbone has proven successful in facilitating SPEG any strain may result in misorientation, as seen in the suspended NWs, and hence defect formation. With an increase in rigidity, i.e. presence of crystal seed (backbone), and a rectangular cross section the post-implantation anneal of the top-down fabricated NW4 is more comparable with a bulk substrate, resulting in almost defect-free SPEG. From a device perspective, patterned Ge NWs developed by lithography (not necessary EBL) show greater promise for large-scale device fabrication in comparison to grown structures.[58]

4.5 Conclusions

Suspended Ge NWs that have experienced full amorphisation after irradiation and have lost their rigidity (i.e. bent NWs after irradiation), although having crystal seed templates, show competing action of the SPEG and RNG processes, resulting in highly defective and poly-crystal growth. A loss of ordering with amorphisation results in misorientation of crystal seeds in NWs due to deformation with decreasing rigidity. The effect of misorientation of the crystal grains due to ion beam induced bending is minimized when the amorphisation is limited to allow a crystalline backbone and/or with external support in a matrix. The minimized misorientation resulted in diminished RNG and hence SPEG was promoted.

Recrystallization of a NW is complex due to the high surface area and hence sensitivity to any alteration to the surface, such as surface roughness and H infiltration.[47] {111} stacking fault pinning at the surface of the NW has been directly observed in this study. This result highlights the contributing factor that the surface-area to volume ratio has on NW recrystallization for both the rate and crystal structure.

It has been observed that for <111> grown NWs, no defects formed in the growth direction of the NW, i.e. no lateral (111) stacking faults are formed.[30] However, for the <112> grown NW containing intrinsic ($\bar{1}$11) longitudinal defects, extrinsic ($\bar{1}$11) defects parallel to the intrinsic defects formed as well as {111} stacking fault defects pinned to the surface. In other studies, a high temperature anneal has shown to cure extrinsic {111} stacking faults[17] but a thermal budget for device fabrication may limit process temperatures. An alternative potential route for ion beam doping of

nanostructures is moderate heating (approximately 250 °C) during irradiation which promotes dynamic annealing.[59]

In summary, crystal recovery of grown and top-down fabricated Ge NWs studied using in situ TEM has been presented. Using in situ TEM data supported by MD calculations, we demonstrate that the recrystallization of the Ge NWs is complex and may result in structures having polycrystalline regions, large number of extended crystal defects such as stacking faults, and in some cases full crystal recovery. We identified that factors such as the amount of initial crystal damage and associated rigidity of the NWs as well as the roughness of the c/a interface and the surface to volume ratio, i.e. proximity of the re-growth front(s) to the surface are very important in engineering the NW crystal recovery.

4.6 References

1 Cui, Y., Zhong, Z. H., Wang, D. L., Wang, W. U. & Lieber, C. M. High performance silicon nanowire field effect transistors. *Nano Lett.* 3, 149-152, doi:10.1021/nl025875l (2003).

2 Huang, Y., Duan, X. F., Cui, Y., Lauhon, L. J., Kim, K. H., Lieber, C. M. Logic gates and computation from assembled nanowire building blocks. *Science* 294, 1313-1317, doi:10.1126/science.1066192 (2001).

3 Michel, J., Liu, J. & Kimerling, L. C. High-performance Ge-on-Si photodetectors. *Nat. Photonics* 4, 527-534, doi:10.1038/nphoton.2010.157 (2010).

4 Cui, Y., Wei, Q. Q., Park, H. K. & Lieber, C. M. Nanowire nanosensors for highly sensitive and selective detection of biological and chemical species. *Science* 293, 1289-1292, doi:10.1126/science.1062711 (2001).

5 Tian, B., Zheng, X., Kempa, T. J., Fang, Y., Yu, N., Yu, G., Huang, J., Lieber, C. M. Coaxial silicon nanowires as solar cells and nanoelectronic power sources. *Nature* 449, 885-U888, doi:10.1038/nature06181 (2007).

6 Yan, R., Gargas, D. & Yang, P. Nanowire photonics. *Nat. Photonics* 3, 569-576, doi:10.1038/nphoton.2009.184 (2009).

7 Yoon, J. S., Rim, T., Kim, J., Kim, K., Baek, C. K., Jeong, Y. H. Statistical variability study of random dopant fluctuation on gate-all-around inversion-mode silicon nanowire field-effect transistors. *Appl. Phys. Lett.* 106, doi:10.1063/1.4914976 (2015).

8 Koenraad, P. M. & Flatte, M. E. Single dopants in semiconductors. *Nat. Mater.* 10, 91-100, doi:10.1038/nmat2940 (2011).

9 Duffy, R., Shayesteh, M., Thomas, K., Pelucchi, E., Yu, R., Gangnaik, A., Georgiev, Y. M., Carolan, P., Petkov, N., Long, B., Holmes, J. D. Access resistance reduction in Ge nanowires and substrates based on non-destructive gas-source dopant in-diffusion. *J. Mater. Chem. C* 2, 9248-9257, doi:10.1039/c4tc02018a (2014).

10 Long, B., Alessio Verni, G., O'Connell, J., Holmes, J. D., Shayesteh, M., O'Connell, D., Duffy, R. Molecular layer doping: Non-destructive doping of silicon and germanium. *Proceedings of the 20th International Conference on Implantation Technology.* 1-4, doi:10.1109/iit.2014.6939995 (2014)

11 O'Connell, J., Verni, G. A., Gangnaik, A., Shayesteh, M., Long, B., Georgiev, Y. M., Petkov, N., McGlacken, G. P., Morris, M. A., Duffy, R., Holmes, J. D. Organo-arsenic Molecular Layers on Silicon for High-Density Doping. *ACS Appl. Mater. Interfaces* 7, 15514-15521, doi:10.1021/acsami.5b03768 (2015).

12 Kelly, R. A., Holmes, J. D. & Petkov, N. Visualising discrete structural transformations in germanium nanowires during ion beam irradiation and subsequent annealing. *Nanoscale* 6, 12890-12897, doi:10.1039/c4nr04513k (2014).

13 Zeiner, C., Lugstein, A, Buchhart, T., Pongratz, P., Connell, J. G., Lauhon, L. J., Bertagnolli, E. Atypical Self-Activation of Ga Dopant for Ge Nanowire Devices. *Nano Lett.* 11, 3108-3112, doi:10.1021/nl201105k (2011).

14 Yu, R., Georgiev, Y. M., Das, S., Hobbs, R. G., Povey, I. M., Petkov, N., Shayesteh, M., O'Connell, D., Holmes, J. D., Duffy, R. Junctionless nanowire transistor fabricated with high mobility Ge channel. *Phys. Status Solidi RRL* 8, 65-68, doi:10.1002/pssr.201300119 (2014).

15 Guilloy, K., Pauc, N., Robin, E., Calvo, V., Gentile, P., Foubert, K., Rothman, J., Reboud, V., Chelnokov, A., Benevent, V., Hartmann, J. M. Band structure engineering of strained and doped germanium nanowires and 2D layers. *IEEE Int. Conf.IV Photonics,11th* 233-234 doi:10.1109/Group4.2014.6961940 (2014).

16 Priolo, F., Gregorkiewicz, T., Galli, M. & Krauss, T. F. Silicon nanostructures for photonics and photovoltaics. *Nat. Nanotechnol.* 9, 19-32, doi:10.1038/nnano.2013.271 (2014).

17 Duffy, R., Shayesteh, M., McCarthy, B., Blake, A., White, M., Scully, J., Yu, R., Kelleher, A. M., Schmidt, M., Petkov, N., Pelaz, L., Marques, L. A. The curious case of thin-body Ge crystallization. *Appl. Phys. Lett.* 99, doi:10.1063/1.3643160 (2011).

18 Duffy, R. Van Dal, M. J. H., Pawlak, B. J., Kaiser, M., Weemaes, R. G. R., Degroote, B., Kunnen, E., Altamirano, E. Solid phase epitaxy versus random nucleation and growth in sub-20nm wide fin field-effect transistors. *Appl. Phys. Lett.* 90, doi:10.1063/1.2749186 (2007).

19 Barth, S., Boland, J. J. & Holmes, J. D. Defect transfer from nanoparticles to nanowires. *Nano Lett.* 11, 1550-1555, doi:10.1021/nl104339w (2011).

20 Geaney, H., Dickinson, C., Weng, W. H., Kiely, C. J., Barrett, C. A., Gunning, R. D., Ryan, K. M. Role of Defects and growth directions in the formation of periodically twinned and kinked unseeded germanium nanowires. *Cryst. Growth Des.* 11, 3266-3272, doi:10.1021/cg200510y (2011).

21 Marques, L. A., Pelaz, L., Santos, I., Lopez, P. & Duffy, R. Molecular dynamics simulation of the regrowth of nanometric multigate Si devices. *J. Appl. Phys.* 111, doi:10.1063/1.3679126 (2012).

22 Jun, K., Joo, J. & Jacobson, J. M. Focused ion beam-assisted bending of silicon nanowires for complex three dimensional structures. *J. Vac. Sci. Technol. B* 27, 3043-3047, doi:10.1116/1.3259919 (2009).

23 Ronning, C., Borschel, C., Geburt, S. & Niepelt, R. Ion beam doping of semiconductor nanowires. *Mater. Sci. Eng., R* 70, 30-43, doi:10.1016/j.mser.2010.07.002 (2010).

24 Das Kanungo, P., Koegler, R., Zakharov, N., Werner, P., Scholz, R., Skorupa, W. Characterization of Structural Changes Associated with Doping Silicon Nanowires by Ion Implantation. *Cryst. Growth Des.* 11, 2690-2694, doi:10.1021/cg200108u (2011).

25 Pecora, E., Irrera, A., Boninelli, L., Spinella, C., Priolo, F. Nanoscale amorphization, bending and recrystallization in silicon nanowires. *Appl. Phys. A: Mater. Sci. Process* 102, 13-19, doi:10.1007/s00339-010-6040-2 (2011).

26 Fukata, N., Takiguchi, R., Ishida, S., Yokono, S., Hishita, S., Murakami, K. Recrystallization and Reactivation of Dopant Atoms in Ion-Implanted Silicon Nanowires. *ACS Nano* 6, 3278-3283, doi:10.1021/nn300189z (2012).

27 Zhang, Y. F., Tang, Y. H., Wang, N., Lee, C. S., Bello, I., Lee, S. T. Germanium nanowires sheathed with an oxide layer. *Phys. Rev. B: Condens. Matter Mater. Phys.* 61, 4518-4521 (2000).

28 Seo, K. I., Sharma, S., Yasseri, A. A., Stewart, D. R. & Kamins, T. I. Surface charge density of unpassivated and passivated metal-catalyzed silicon

nanowires. *Electrochem. Solid-State Lett.* 9, G69-G72, doi:10.1149/1.2159295 (2006).

29 Grossklaus, K. A., Banerjee, A., Jahangir, S., Bhattacharya, P. & Millunchick, J. M. Misorientation defects in coalesced self-catalyzed GaN nanowires. *J. Cryst. Growth* 371, 142-147, doi:10.1016/j.jcrysgro.2013.02.019 (2013).

30 Romano, L., Rudawski, N. G., Holzworth, M. R., Jones, K. S., Choi, S. G., Picraux, S. T. Nanoscale manipulation of Ge nanowires by ion irradiation. *J. Appl. Phys.* 106, doi:10.1063/1.3267154 (2009).

31 Borschel, C., Spindler, S., Lerose, D., Bochmann, A., Christiansen, S. H., Nietzsche, S., Oertel, M., Ronning, C. Permanent bending and alignment of ZnO nanowires. *Nanotechnology* 22, doi:10.1088/0957-4484/22/18/185307 (2011).

32 Gomez-Selles, J. L., Darby, B. L., Jones, K. S. & Martin-Bragado, I. Lattice kinetic Monte Carlo modeling of germanium solid phase epitaxial growth. *Phys. Status Solidi C* 11, 93-96, doi:10.1002/pssc.201300159 (2014).

33 Darby, B. L., Yates, B. R., Martin-Bragado, I., Gomez-Selles, J. L., Elliman, R. G., Jones, K. S. Substrate orientation dependence on the solid phase epitaxial growth rate of Ge. *J. Appl. Phys* 113, doi:10.1063/1.4776718 (2013).

34 Pelaz, L., Marques, L., Aboy, M., Lopez, P., Santos, I., Duffy, R. Atomistic process modeling based on Kinetic Monte Carlo and Molecular Dynamics for optimization of advanced devices. *IEEE Int. Electorn Devices Meet.* 1-4, doi:10.1109/iedm.2009.5424309 (2009).

35 Hobbs, R. G., Schmidt, M., Bolger, C. T., Georgiev, Y. M., Fleming, P., Morris, M. A., Petkov, N., Holmes, J. D., Xiu, F. X., Wang, K. L., Djara, V., Yu, R., Colinge, J. P. Resist-substrate interface tailoring for generating high-density arrays of Ge and Bi_2Se_3 nanowires by electron beam lithography. *J. Vac. Sci. Technol., B* 30, doi:10.1116/1.4724302 (2012).

36 Ran, Y., Das, S., Hobbs, R., Georgiev, Y., Ferain, I., Razavi, P., Akhavan, N. D., Colinge, C. A., Colinge, J. Top-down process of germanium nanowires using EBL exposure of hydrogen silsesquioxane resist. *J. Ultimate Integr. Silicon* 145-148, doi: 10.1109/ulis.2012.6193378 (2012).

37 Plimpton, S. Fast parallel algorithms for short-range molecular dynamics. *J. Computat. Phys.* 117, 1-19, doi:10.1006/jcph.1995.1039 (1995).

38 Posselt, M. & Gabriel, A. Atomistic simulation of amorphous germanium and its solid phase epitaxial recrystallization. *Phys. Rev. B* 80, doi:10.1103/PhysRevB.80.045202 (2009).

39 Luedtke, W. D. & Landman, U. Preparation, structure, dynamics, and energetics of amorphous silicon: A molecular-dynamics study. *Phys. Rev. B:*

Condens. Matter Mater. Phys. 40, 1164-1174, doi:10.1103/PhysRevB.40.1164 (1989).

40 Berendsen, H. J. C., Postma, J. P. M., van Gunsteren, W. F., DiNola, A. & Haak, J. R. Molecular dynamics with coupling to an external bath. *J. Chem. Phys.* 81, 3684-3690, doi:10.1063/1.448118 (1984).

41 Wang, Y., Hu, Y. Z. & Irene, E. A. Electron –cyclotron-resonance plasma and thermal-oxidation mechanisms of germanium. *J. Vac. Sci. Technol., A* 12, 1309-1314, doi:10.1116/1.579313 (1994).

42 Bender, H., Deveirman, A., Vanlanduyt, J. & Amelinckx, S. HREM investigation of twinning in very high-dose phosphorus ion-implanted silicon. *Appl. Phys. A* 39, 83-90, doi:10.1007/bf00616823 (1986).

43 Su, Z., Dickinson, C., Wan, Y., Wang, Z., Wang, Y., Sha, J., Zhou, W. Crystal growth of Si nanowires and formation of longitudinal planar defects. *CrystEngComm* 12, 2793-2798, doi:10.1039/b925198g (2010).

44 Kelly, P. M., Wauchope, C. J. & Zhang, X. Calculation of overall tilt angles for a double tilt holder in a TEM. *Microsc. Res. Tech.* 28, 448-451, doi:10.1002/jemt.1070280512 (1994).

45 Csepregi, L., Küllen, R. P., Mayer, J. W. & Sigmon, T. W. Regrowth kinetics of amorphous Ge layers created by ^{74}Ge and ^{28}Si implantation of Ge crystals. *Solid State Commun.* 21, 1019-1021, doi:10.1016/0038-1098(77)90009-6 (1977).

46 Priolo, F., Battaglia, A., Nicotra, R. & Rimini, E.Low-temperature reordering in partially amorphized Si crystals. *Appl. Phys. Lett.* 57, 768-770, doi:10.1063/1.103415 (1990).

47 Johnson, B. C., Gortmaker, P. & McCallum, J. C. Intrinsic and dopant-enhanced solid-phase epitaxy in amorphous germanium. *Phys. Rev. B* 77, 214109 doi:10.1103/PhysRevB.77.214109 (2008).

48 Borschel, C. & Ronning, C. Ion beam irradiation of nanostructures - A 3D Monte Carlo simulation code. *Nucl. Instrum. & Methods Phys. Res. B* 269, 2133-2138, doi:10.1016/j.nimb.2011.07.004 (2011).

49 den Hertog, M. I., Cayron, C., Gentile, P., Dhalluin, F., Oehler, F., Baron, T., Rouviere, J. L. Hidden defects in silicon nanowires. *Nanotechnology* 23, doi:10.1088/0957-4484/23/2/025701 (2012).

50 Drosd, R. & Washburn, J. Some observations on the amorphous to crystalline transformation in silicon. *J. Appl. Phys.* 53, 397-403, doi:10.1063/1.329901 (1982).

51 Olson, G. L. & Roth, J. A. Kinetics of solid phase crystallization in amorphous silicon. *Mater. Sci. Rep.* 3, 1-77, doi:10.1016/S0920-2307(88)80005-7 (1988).

52 Donovan, E. P., Spaepen, F., Turnbull, D., Poate, J. M. & Jacobson, D. C. Calorimetric studies of crystallization and relaxation of amorphous Si and Ge

prepared by ion implantation. *J. Appl. Phys.* 57, 1795-1804, doi:10.1063/1.334406 (1985).

53 Lu, G. Q., Nygren, E. & Aziz, M. J. Pressure-enhanced crystallization kinetics of amorphous Si and Ge: Implications for point-defect mechanisms. *J. Appl. Phys.* 70, 5323-5345, doi:10.1063/1.350243 (1991).

54 Haynes, T. E., Antonell, M. J., Lee, C. A. & Jones, K. S. Composition dependence of solid-phase epitaxy in silicon-germanium alloys: Experiment and theory. *Phys. Rev. B: Condens. Matter Mater. Phys.* 51, 7762-7771 doi:10.1103/PhysRevB.51.7762 (1995).

55 Kringhøj, P. & Elliman, R. G. Solid-Phase Epitaxial Crystallization of Strain-Relaxed $Si_{1-x}Ge_x$ Alloy Layers. *Phys. Rev. Lett.* 73, 858-861 doi:10.1103/PhysRevLett.73.858 (1994).

56 Li, D., Nielsen, M. H., Lee, J. R. I., Frandsen, C., Banfield, J. F., De Yoreo, J. J. Direction-Specific Interactions Control Crystal Growth by Oriented Attachment. *Science* 336, 1014-1018, doi:10.1126/science.1219643 (2012).

57 Mecklenburg, M., Hubbard, W. A., White, E. R., Dhall, R., Cronin, S. B., Aloni, S., Regan, B. C. Nanoscale temperature mapping in operating microelectronic devices. *Science* 347, 629-632, doi:10.1126/science.aaa2433 (2015).

58 Hobbs, R. G., Petkov, N. & Holmes, J. D. Semiconductor Nanowire Fabrication by Bottom-Up and Top-Down Paradigms. *Chem. Mater.* 24, 1975-1991, doi:10.1021/cm300570n (2012).

59 Posselt, M., Bischoff, L., Grambole, D. & Herrmann, F. Competition between damage buildup and dynamic annealing in ion implantation into Ge. *Appl. Phys. Lett.* 89, doi:10.1063/1.2360238 (2006).

4.7. Appendix

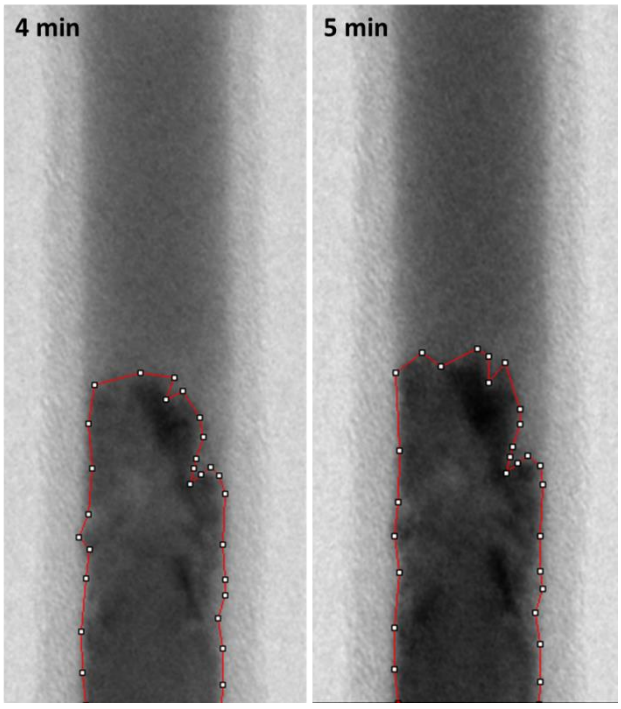

Figure 4.A. Area of crystal region measured from in-situ anneal images for NW1.

The method used to calculate the rates of crystallization presented in this study:

The grown nanowire is assumed to have a circular cross section, i.e. a cylindrical shape nanowire. The cross sectional area of the nanowire is calculated $=\pi r^2$. This area was taken and the volume was averaged to assume a square cross section, i.e. cuboid shape nanowire, and the square root of the circular cross section was determined as the effective depth of the nanowire. When an amorphous area was measured (as shown in Figure 4.A), this was multiplied by the effective depth to calculate an approximate volume in nm^3. To convert the volume into number of atoms (to make the units relatable to the simulation data) this volume was multiplied by the number of atoms per nm^3 which for Ge is 44.355 atoms nm^{-3}.

Molecular dynamics simulations were contributed by Dr Bartosz Liedke, Dr Matthias Posselt and Mr Stefan Baldauf of Helmholtz Zentrum Dresden Rossendorf, Institute of Ion Beam Physics and Materials Research in Dresden. In this study the LAMMPS program was employed[37] with a Stillinger-Weber-type interatomic potential.[38] The simulation cell used for the calculation were cuboids with a size of 20 x 20 x 30 a^3 and 20 x 20 x 60 a^3, i.e. initially with a total of 96000 and 192000 atoms, respectively, where a = 5.657 Å is the lattice parameter of c-Ge. Simulation cells with long sides parallel to the <111> and the <100> crystal axes were considered in order to study NWs with these orientations. Periodic boundary conditions in three directions and a canonical ensemble (NVT) were used. The amorphous region was prepared by the method of Luedtke et al.[39] via slow cooling from the melt at a rate of 1 K ps^{-1}, analogically to the work of Posselt et al.[38] To obtain a NW with free surfaces in x- and y-directions, all atoms within the distance of 5a from the x,y-borders of the simulation cell were removed. The resulting systems with 24000 (for 20 x 20 x 30a^3 simulation cell) and 48000 atoms (for 20 x 20 x 60a^3 simulation cell) consist of two c/a interfaces as shown in Figure 4.B (a) and (c). In recrystallization calculations at 700, 750, 800, and 900 K (426.85, 476.85, 526.85, and 626.85 °C, respectively) a Berendsen thermostat was used.[40] Zero pressure (stress) was maintained at the cell boundaries in both z-directions using a Berendsen barostat.

Molecular dynamics (MD) calculations are presented (by Dr Bartosz Liedke, Dr Matthias Posselt and Mr Stefan Baldauf of Helmholtz Zentrum Dresden Rossendorf, Institute of Ion Beam Physics and Materials Research in Dresden) in Figure 4.B for a

< 111 > grown NW. The notable comparison between the MD calculations and the experimental results is the trend of an initial linear growth followed by a saturation of the recrystallization rate (regions B and C in Figure 4.6 g and in Figure 4.7 g). From the MD calculations in figure 4.B (a), it can be observed that the initial average growth rate is approximately 1×10^{12} atoms s^{-1} for the first 6 ns. The observed average rate for the time from 6 to 16 ns is approximately 6×10^{11} atoms s^{-1} which is a drop to 60% of the initial average rate. The absolute values of simulated recrystallization rates are larger than the measured data. This is related to the quality of the interatomic potential used in the calculations, which was designed to reproduce realistic properties of crystalline, amorphous and liquid Ge but does not describe SPEG quantitatively correct. Therefore the comparison with experimental results is focused on the general trends regarding the recrystallization process and not on the absolute values of the recrystallization rates.

MD calculations have also been presented for a <100> grown nanowire in Figure 4.B (c) and (d). Three different rates of SPEG are visible for each curve, except 700 K annealing, where saturation has not yet been achieved. Decrease of the regrowth rate in the first few ns of annealing for each temperature suggests a considerable importance of confinement effects. The rates decrease again after the two fronts of recrystallization meet in the middle of the supercell. The thick lines are the linear fits applied for the initial slopes, used to calculate activation energy of SPEG that equals 0.92 eV.

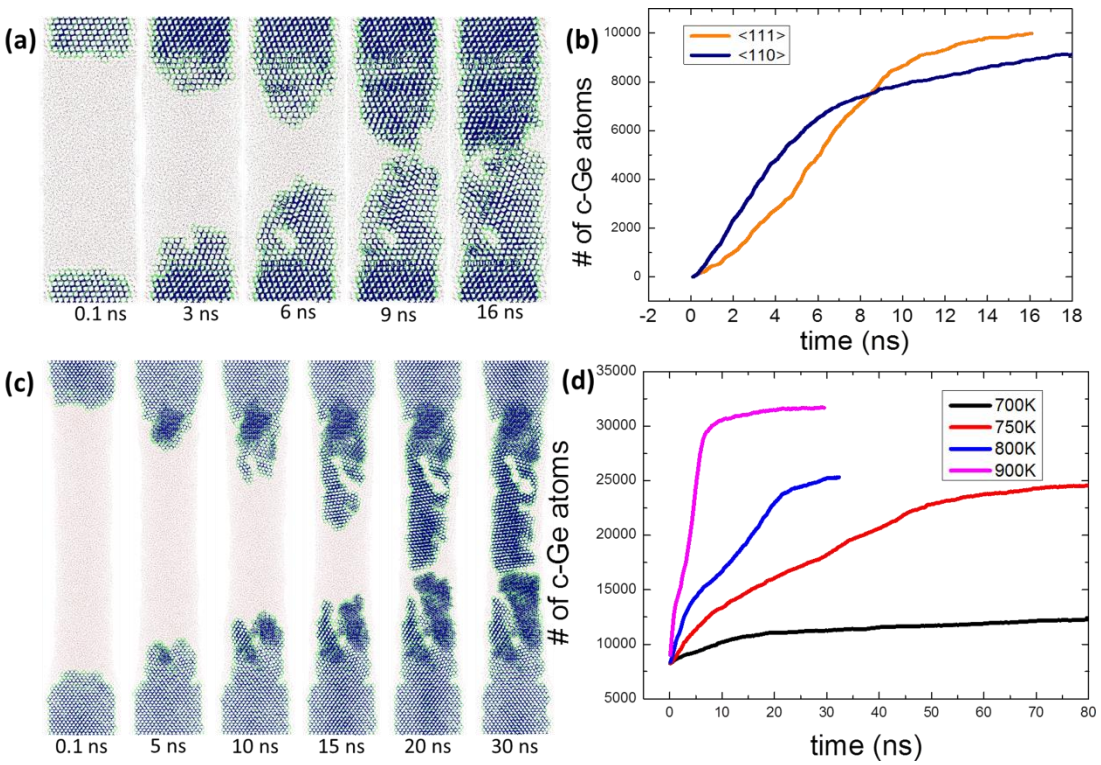

Figure 4.B. **These calculations were contributed to the work by Dr Bartosz Liedke, Dr Matthias Posselt and Mr Stefan Baldauf of Helmholtz Zentrum Dresden Rossendorf, Institute of Ion Beam Physics and Materials Research in Dresden.** (a) Molecular dynamics simulation of recrystallization of a <111> grown Ge NWs at 800K. (b) Comparison of SPEG of NWs for two orientations <100> and <111> shows a very similar growth rate using MD calculations. Simulation cell size is $20\times20\times30a^3$, where a = 5.657 Å in both figures (a) and (b). (c) <100> growth in Ge NW at T=800K (d) <100> growth in Ge NWs at varied T: 700K, 750K, 800K and 900K. Simulation cell size is $20\times20\times60a^3$, where a = 5.657 Å in both figures (c) and (d).

Chapter 5

Investigating the formation of nickel germanides in germanium nanostructures

5.1. Abstract

In this chapter, a method to directly observe the formation of germanides in Ge nanostructures is described. The method involves the preparation of Ge nanopillars with nickel caps via EBL. In situ observation of germanide formation via TEM for a range of diameters is detailed. Overall migration of Ni is observed as well as some Ge migration. The importance of the Ni seed and diameter of the nanostructure is discussed. A comparison to the atomically flat interface in Ni-seed Ge nanowire growth is presented.

5.2. Introduction

To realise the potential of Ge nanowires as transistor interconnects, an (ideally) Ohmic contact is required to overcome the Schottky barrier at the mental-semiconductor interface especially as the trend towards smaller dimensions is pushed. Germanides are quasi-metallic compounds formed between Ge and metals which are more electropositive than Ge. The phase diagram for nickel germanide is very complex and many phases have been identified.[1] Wittmer et al. presented a report based on the rule proposed by Walser and Bené[2] predicting Ni_2Ge to nucleate first, followed by NiGe.[3] NiGe has shown promise as a germanide of choice due to its low resistivity of 22 μΩcm and thermal stability.[4] The (orthorhombic) NiGe phase has been shown to have the lowest resistance of germanide materials, with the added bonus that Ni chemical etches are compatible with Ge device processing.[5] A sharp germanide/Ge interface has demonstrated a decrease in sheet resistance and

hence a method to form solely the NiGe phase with a sharp Ge/NiGe interface is desired.[6]

Studies into the formation of nickel germanides have concentrated mainly on bulk Ge substrates.[6-15] Some researchers have ventured into the investigation of the formation of nickel germanides in nanowires.[15-18] The growth of the germanide along the Ge NW can be controlled to tune the channel length.[17] Tsai et al. used EBL/metal lift off technique to produce Ni contacts to grown Ge NWs on Si_3N_4 membranes and produced the nickel germanides by rapid thermal annealing (RTA). They found that the channel length was controllable by adjusting the number of annealing steps.

Nath et al. observed germanide formation by reactive deposition via electron beam evaporation of Ni in situ at 300 °C on Ge(001) in UHV TEM system.[19] The NiGe phase formed directly with the relationship to the Ge given by NiGe($\bar{1}$01)//Ge(001) and NiGe[010] //Ge[110]. Deng et al. also used reactive deposition and achieved near-atomically flat Ge/germanide interface on Ge(001) forming the NiGe phase with a NiGe(111)//Ge(001) and NiGe[0$\bar{1}$1]//Ge[110] epitaxial relationship. Peter et al. demonstrated the NiGe films formation via catalytic solid-vapour reaction of Ni and GeH_4.[12] The reaction process temperature is relatively low (225-300 °C) and is comparable with anneal temperatures previously reported for germanide formation in a solid state reaction. Smooth and uniform films with thicknesses from 10-23 nm were achieved and were found to be stable up to 500 °C. In their study, Nemouchi et al. identified the formation of NiGe during Ni deposition at room temperature.[14] Low temperature annealing produced Ni_5Ge_3 phase with simultaneous growth of NiGe. Typically, a sequential formation of the germanides is observed; first the Ni rich

phase followed by the NiGe phase. The explanation provided to this abnormal simultaneous growth observed by Nemouchi et al. is the low critical thickness of Ni_5Ge_3 and the different control growths of the two phases.

Comrie et al. investigated the dominant diffusing species during Ni-germanide formation via real-time Rutherford backscattering spectroscopy.[20] It was determined that Ni was the sole diffusing species during Ni_5Ge_3 formation and it was the dominant diffusing species during NiGe formation with some Ge diffusion observed in the initial stages of NiGe formation. Nemouchi et al. identified the diffusion of Ni into Ge via GeO_x with the formation of a germanate ($Ni_xO_yGe_z$) intermediate.[21] This is observed up to a thickness of 8 nm for both grown and native oxides. This is important as the Ge native oxide is difficult to remove and clean Ge rapidly re-oxidises on exposure to air.

Due to the high surface area/volume ratio of nanostructures, it is likely that surface energy may affect the germanide formation. Tang et al. presented a study on the germanium/germanide heterostructure nanowire transistor but with a new segment of NiGe formed producing Ni_2Ge/NiGe/Ge/NiGe/Ni_2Ge heterostructure.[18] This was achieved due to confinement by Al_2O_3 during annealing at 450 °C (within the temperature range of the previous study by Tang et al.[22]). An improved on/off ratio was achieved (10^5) and this is attributed to the NiGe layer formed providing an Ohmic contact to the Ge NW. The epitaxial relationships were determined as Ge[011]//NiGe[010] and Ge(111)//NiGe(001) for the Ge/NiGe interface and Ni_2Ge[100]//NiGe[010] and Ni_2Ge(011)//NiGe(001) for the Ni_2Ge/NiGe.

The objective of this study is to investigate the formation of the NiGe phase and the size dependence on germanide formation within a nanostructure. The importance of the Ni seed is investigated with a limited, known, finite volume and allowing direct observation of the Ni seed during thermal annealing.

5.3. Experimental

5.3.1. Ni-capped Ge nanopillar preparation.

The process flow for the fabrication of Ni-capped Ge nanopillars is illustrated in Figure 5.1. A method to produce nanopillars of Ge with varied diameters has been developed with the use of EBL. Ni-capped germanium nanopillars were fabricated on Ge(001) substrates. A positive tone EBL resist was used to expose desired circular areas on the Ge substrate as shown in Figure 5.1.

Initially, a two layer (PMMA-copolymer) EBL resist was used to facilitate a facile metal lift process. However, an undesirable lip of Ni was observed for the pillars, which is attributed to the collapse of the upper resist during metal evaporation (Figure 5.2). As the metal is used as a mask for etching this results in larger diameter pillars than desired. Hence, for further sample preparation the Ge substrate was patterned by EBL using SML-50, a high resolution positive tone EBL resist.[23] Single pixel dot exposures, with 1 μm pitch, were defined in a line with large markers on either side.

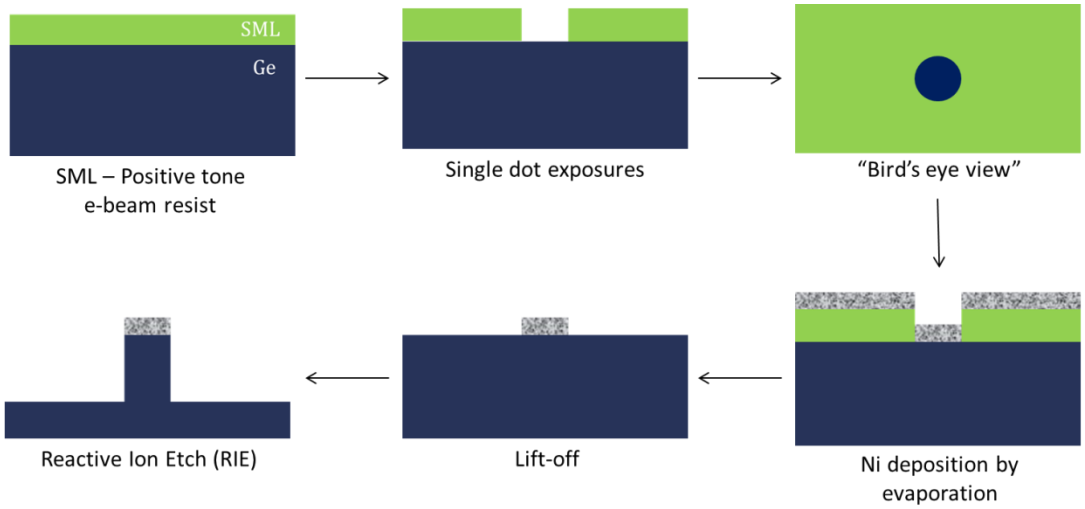

Figure 5.1. Process flow for Ni-capped Ge nanopillar preparation

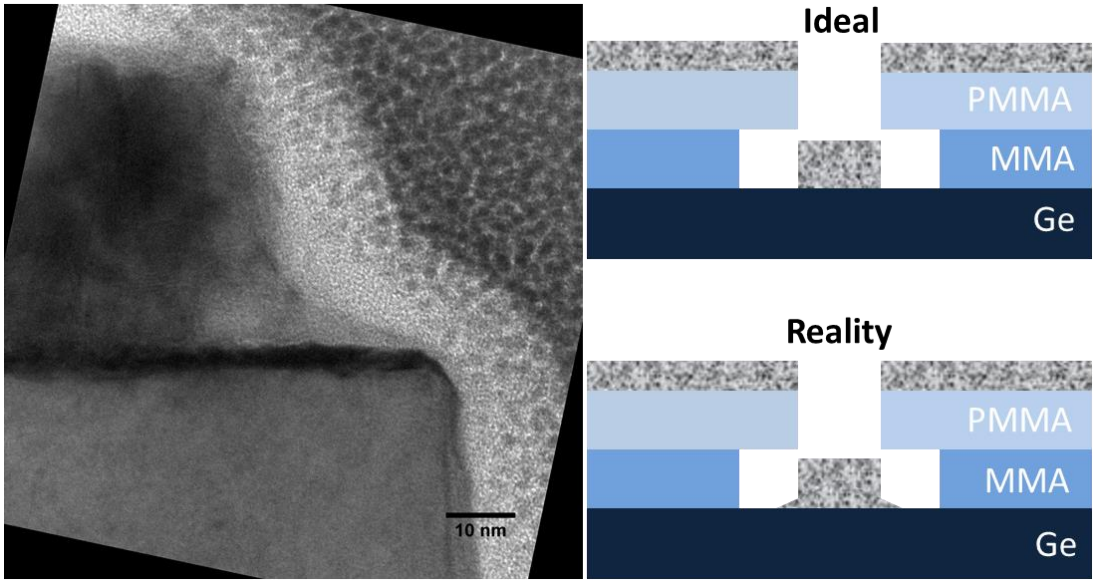

Figure 5.2. Issue arisen with PMMA-copolymer resist during metal deposition.

The diameters of the dots were varied with the dose (dwell time) at each spot; the diameter increases with increasing dose. The dose range used was 0.2 – 6.4 fC per single exposure and the electron beam was operated at 10kV accelerating voltage. After exposure, the resist was developed in 7:3 IPA/deionised water for 30 s

followed by IPA for 15 s and dried under a flow N_2 for 30 sec. A 50 nm thick Ni layer was evaporated, by electron beam evaporation, onto the patterned substrate followed by a metal lift-off in acetone to achieve Ni dots (and markers) on the Ge substrate. The Ge was etched, using the Ni as the hard mask, in a Cl reactive ion etch (RIE) at 20 °C, 30 sccm Cl_2, 10 mtorr and 80W RF.[24]

For annealing experiments, a line of pillars was extracted in a cross section and transferred to an omniprobe grid (an example is shown in Figure 5.3 c). An FEI Helios 600i Nanolab Dual Beam SEM/FIB system was used to prepare the cross sections. To help aid in polishing the cross section to the region of interest, a line of EBID carbon was deposited along the line of dots with a total nominal height of 1 μm, similar to the method described for inline nanowire cross sections described previously in chapter 2. This helps to ensure cut placement and aids in the final FIB polishing of the cross section because the EBID-C has good contrast against the platinum (Pt) protection. The EBID-C also acts as an insulation layer to encapsulate the Ni/Ge pillars. The next layer of protection with the dimensions 15 μm × 2 μm and a nominal height of 250 nm of EBID-Pt was deposited followed by 2 μm ion beam induced deposition (IBID) Pt. During thinning, the cross section was polished only from the front side, by turning the grid 180° with a stage rotation to polish the other side from the front for accurate final polishing.

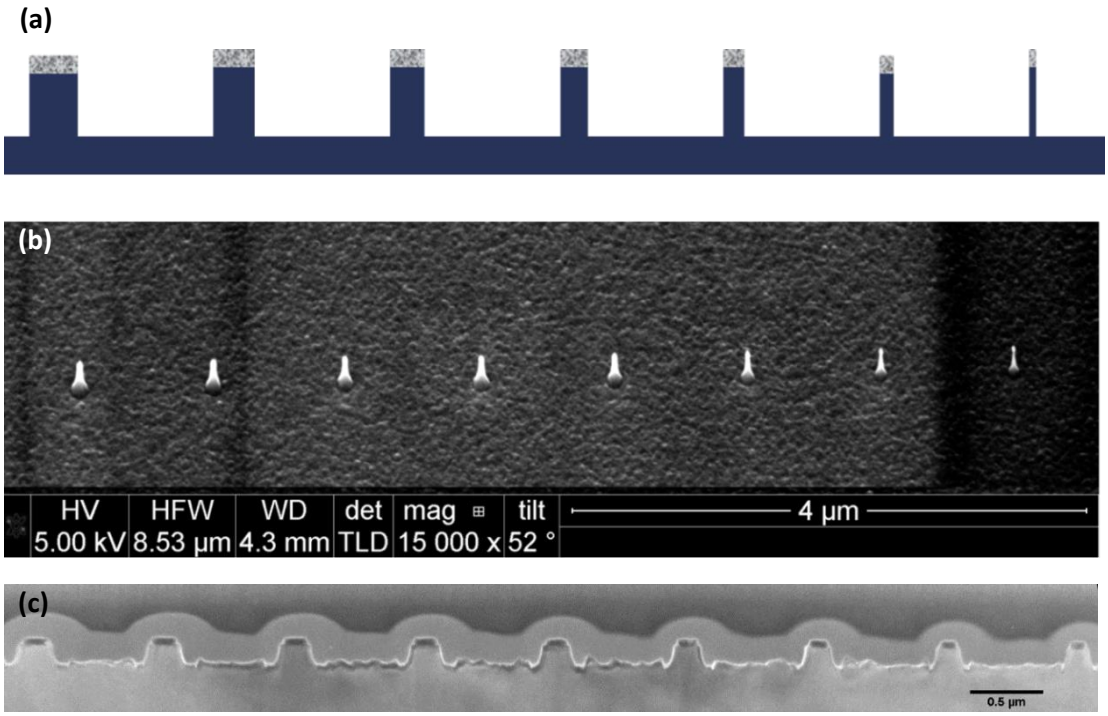

Figure 5.3. Overview of cross section of Ge rods with Ni caps **(a)** ideal schematic **(b)** tilted SEM and **(c)** extracted row of pillars in a FIB cross section for TEM.

Figure 5.3 presents an overview of an example of nanorods with increasing diameter produced in a cross section. A native GeO_x removal step is required before EBL resist deposition to optimise the surface to avoid dewetting and achieve a uniform resist. The water soluble oxide is removed in a 30 s dip in deionised water, followed by a re-oxidation of surface with a 30 s dip in 4.5 M nitric acid (HNO_3) and a final oxide removal and surface passivation step in 10% HCl for 10 min.[25] No oxide removal step was performed on the exposed surface before metal evaporation, which could be a major factor for the rough Ge/Ni interface. Ideally, the sample should be placed directly in the metal evaporator post resist development to avoid oxidation of Ge in ambient air.[26,27]

5.3.2. TEM Characterization.

Before annealing, the structures were imaged using a Gatan double tilt imaging holder in a JEOL 2100 HRTEM and tilted to a low index zone axis for HTREM imaging. The bulk substrate was used to orientate the sample into a zone axis. A Gatan 628 single tilt heating holder was used for in situ annealing. The sample was imaged in bright-field mode using the smallest objective aperture during the anneal to enhance the contrast between the Ni and Ge. After annealing, the sample was imaged in the double tilt holder again for HRTEM imaging in the same orientation as prior to annealing.

5.4 Results and Discussion

5.4.1 Sample 1

A row of pillars from the initial sample using the PMMA-copolymer resist was extracted in a TEM cross section (an overview of all pillars from sample 1 is displayed in Figure 5.4). The diameters at the Ni/Ge interfaces have been approximately measured; **A** 164 nm; **B** 154 nm; **C** 148 nm; **D** 146 nm; **E** 143 nm; **F** 138 nm; **G** 130 nm; **H** 122 nm; **I** 116 nm; **J** 99 nm; **K** 87 nm. Pillar **K** from sample 1 was annealed in situ (Figure 5.4 c) up to 270 °C for a total of 70 min to observe the formation of the germanide for the Ni-capped Ge pillar. The sample was heated to 100 °C and then the temperature was increased by 50 °C steps up to 200 °C, maintaining each temperature for 5 min and acquiring images at 1 minute intervals. Ni migration was first observed at 200 °C, i.e. the interface between the Ni and Ge changed in shape and contrast. The temperature was increased to 210 °C (and

maintained for 10 min) and then increased by 5 °C steps, while remaining at each temperature for 5 min until 240 °C. From here the temperature was increased by 10 °C steps until the hollow in the Ni region formed at 270 °C.

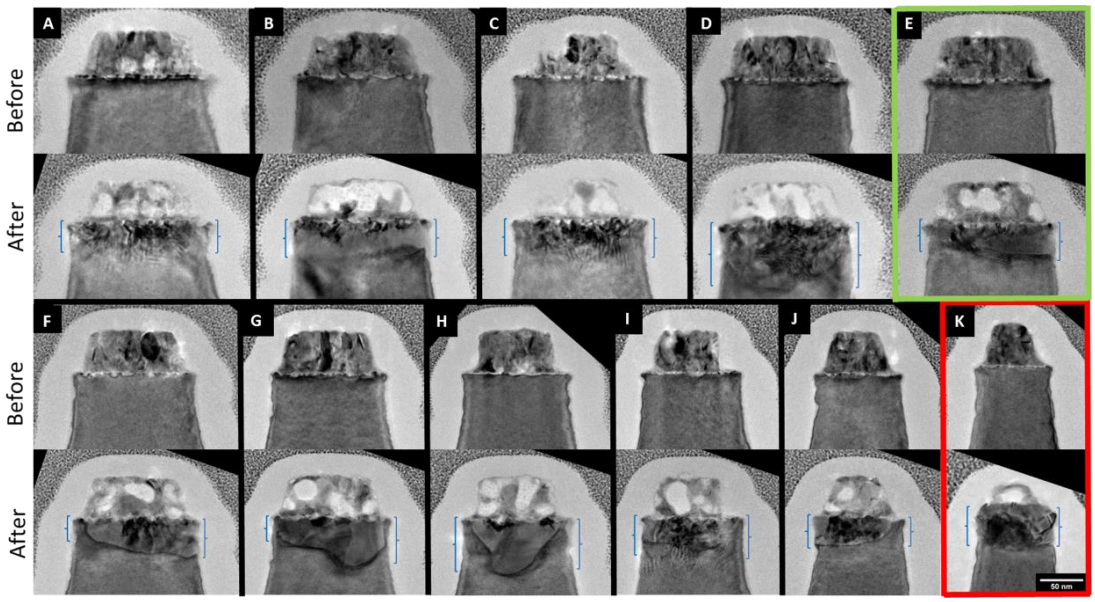

Figure 5.4. Overview of pillars before and after anneal. Pillar **K** highlighted in red box was observed in situ during the anneal. Pillar **E** contains a region with a near atomically flat interface post anneal. Germanide region formed is identified with blue brackets. In the low resolution images here we see voiding in the Ni seed (white patches in after images are hollow regions). The metal migrates into the Ge and forms the germanide which is denser than Ge and hence the germanide region (blue brackets) has a darker contrast than the Ge.

The presence of the oxide does not appear to impede on the germanide formation, as demonstrated by Deng et al.[28] The formation of holes or Kirkendall voids in the Ni during/after annealing has been observed in Ni/Ge core-shell nanostructures.[29] In the Ni-capped Ge pillars in sample 1 the void formation does not consistently occur directly at the Ge/Ni interface. The original Ni seed is polycrystalline and hence varies in the microstructure from pillar to pillar. Opsomer et al. have determined that the crystallinity of the Ge affects the germanide formation with Co (cobalt)[30] and so it is possible that the crystallinity of the Ni seed also affects the germanide

formation. Panciera et al. demonstrated that a silicide nanocrystal within a Au seed of a grown nanowire rotates to align to the lattice of the Si NW. This degree of freedom to allow rotation is facilitated by the eutectic Si-Au alloy. The Ni seed here in this study is solid and there is no freedom for the seed to rotate to align to the Ge nanostructure.

There seems to be no obvious trend in the mechanism of the formation of the germanide in low resolution images, i.e. the shape of the germanide region is completely different with a rough Ge/germanide interface for each pillar (Figure 5.4). The nanopillar diameters in this sample show no evidence of a diameter dependence on the mechanism of germanide formation and the results are comparable to germanide formation on bulk samples at this scale.[6,28] The shape of the grain and its interface with Ge is different for each pillar. For example pillars E, F, G and H in Figure 5.4 all contain large germanide regions (blue brackets) after the anneal but the position and shape of the Ge/germanide interface within the pillars differs. It could be expected that germanide formation may occur preferentially in the centre of the pillar away from the surface where, for example, contaminants adhering to the surface may vary the surface energy, but that does not appear to be the case here as there is no trend to suggest that. The Ge/germanide interface appears to always occur off-centre or asymmetrically, i.e. a flat interface across the whole diameter is not observed, which indicates the Ni migration and/or germanide formation does not occur preferentially in the Ge(001) direction. Another possible factor which affects the germanide formation is the state of the Ni seed, i.e. here it is polycrystalline. The Ni seed was not consumed uniformly and hence we observe the voids in the Ni seed post anneal.

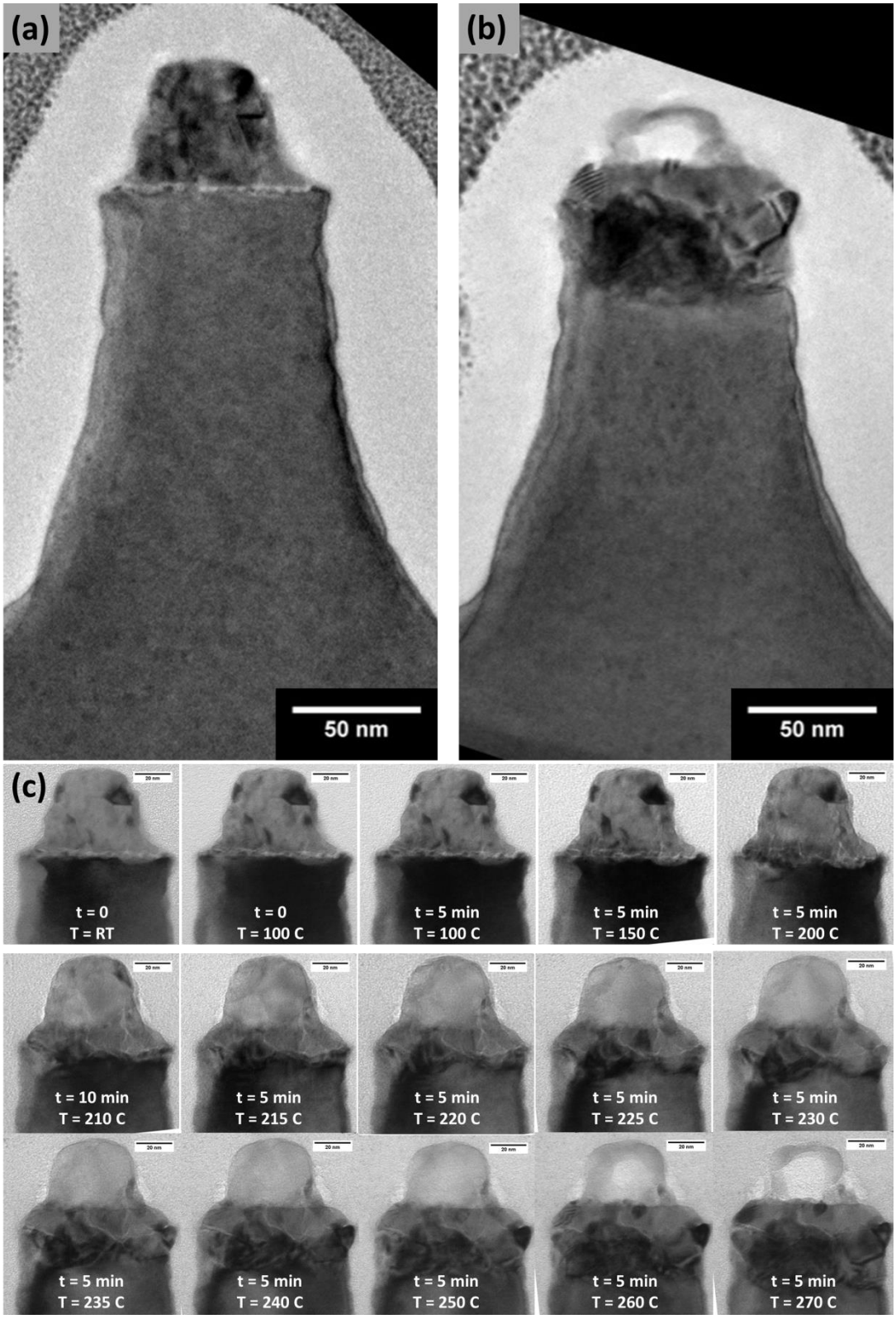

Figure 5.5. Ge pillar K with Ni cap (a) before and (b) after anneal. (c) Images from in situ anneal. The Ni cap brightens as it hollows out and the Ni migrates into the Ge pillar, forming the void in the Ni cap.

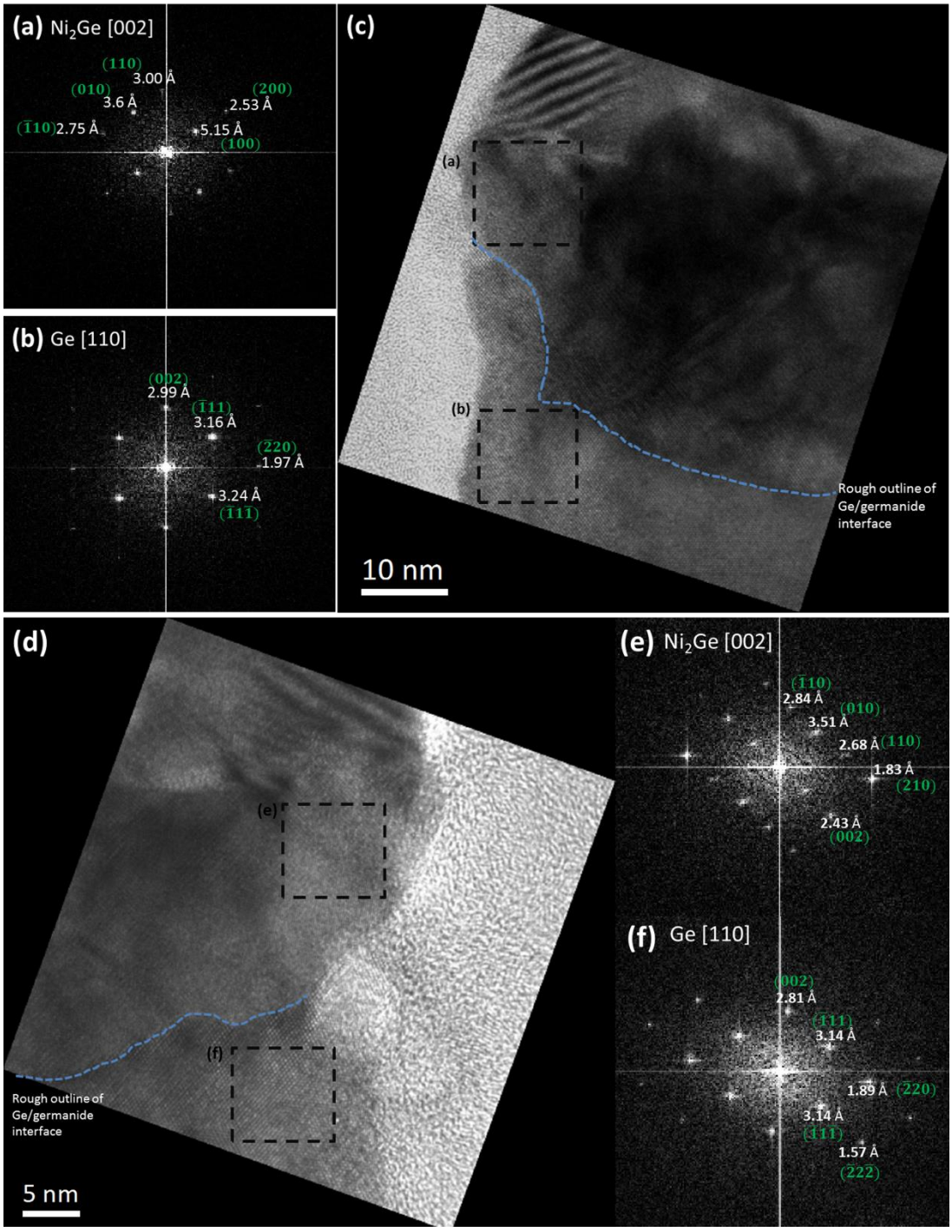

Figure 5.6. (c) Ge-germanide interface of pillar from Figure 5.5 (pillar K highlighted in red in Figure 5.4) post anneal with corresponding FFTs from (a) the germanide region and (b) Ge region. (d) Another region of the pillar at the Ge/germanide interface with extracted FFTs from regions (e) and (f).

HRTEM images of the nanopillars were acquired to identify the phase of germanides formed and to provide further understanding of an underlying mechanism. The d-spacing values were compared to the X-Ray Diffraction (XRD) database. The sample is tilted to the same orientation for HRTEM post-anneal as imaged pre-anneal. A HRTEM of the interface between the germanide and Ge in pillar **K** is shown in Figure 5.6. An initial observation is that the interface is not finite and easily distinguishable. The interface appears to be curved with the interface higher towards the edges and deeper into the Ge towards the centre of the nanopillar; i.e. a concave interface. The germanide is polycrystalline with overlapping crystals highlighted by the presence of moiré fringes. FFTs from the areas identified in Figure 5.6(c) are indexed and the Ni_2Ge phase has been identified.

Upon closer inspection of some of the pillars at lattice resolution, we find a near perfect Ge/germanide interface in Figure 5.4 pillar **E**. An FFT of the germanide region is shown in Figure 5.7 and was indexed and determined to be NiGe[100]. The region shows the formation of an atomically flat interface. Fringes can be observed due to the strain between the Ge and NiGe facets. The epitaxial relationship was found to be Ge[101]//NiGe[100] and Ge$(20\bar{2})$//NiGe$(00\bar{2})$. The lattice mismatch between Ge$(20\bar{2})$ and NiGe$(00\bar{2})$ is 14.3% and this mismatch explains the strain experienced at the interface. Although a substantial lattice mismatch, it is notably smaller than the mismatch calculated by Tang et al. of 77% for the Ge/ NiGe interface, with a crystallographic relationship determined to be Ge$[01\bar{1}]$//NiGe[010] and Ge$(1\bar{1}\bar{1})$//NiGe(001), where an angled growth (i.e. not along the pillar length in (001) direction) is observed.[31] The lattice mismatch is calculated from;

$$f_m = \frac{|a_s - a_l|}{a_s}$$ Equation 4.1

Where f_m = the lattice mismatch, a_s = the lattice constant of the substrate and a_l = the lattice constant of the layer.

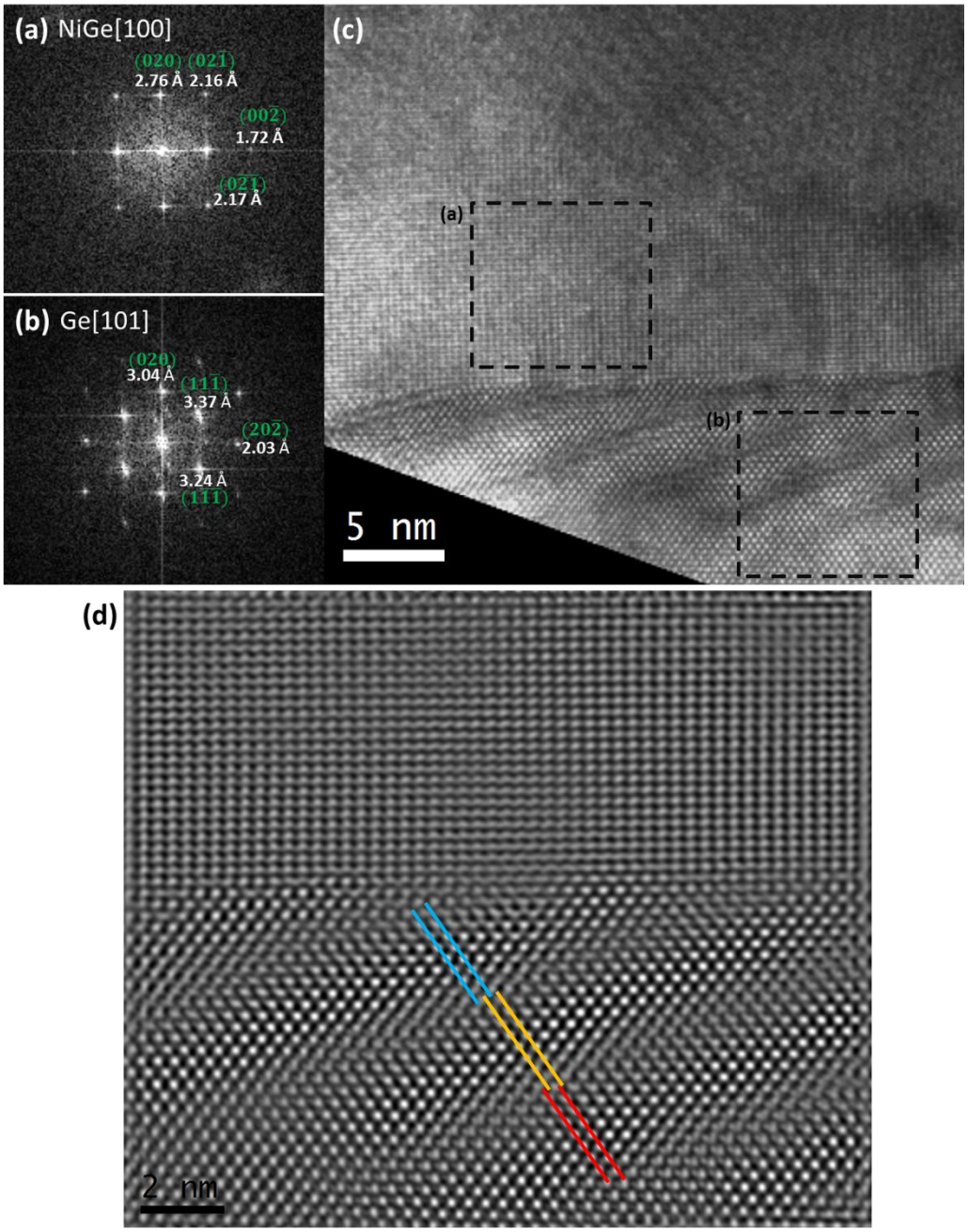

Figure 5.7. (c) Ge-germanide interface of pillar from sample 1 pillar **E** (highlighted in green box in Figure 5.4) with FFTs from **(a)** the germanide and **(b)** Ge regions. **(d)** Reconstructed FFT of Ge/NiGe interface from (c). The blue, yellow and red lines show the misalignment which is likely due to thickness variation at the interface.

We propose that not only is the temperature important when achieving a desired germanide but also the Ni seed. It is observed for the pillars in Figure 5.4 that the Ni seed is polycrystalline. The two variables for the pillars in Figure 5.4 are the diameter and crystal structure of the Ni seed. Another factor which could be interfering with the migration and hence germanide formation is the initial rough Ni/Ge interface. A HRTEM of the interface in Figure 5.8 shows the roughness before the anneal of pillar **K**. The distance required for the Ni to migrate across the GeO_x interface varies and hence the migration across the interface is not uniform. There was no oxide removal step done prior to Ni deposition and the samples had been exposed to ambient air for ~ 24 hours which is more than sufficient time for a native oxide to grow on the exposed Ge surface.

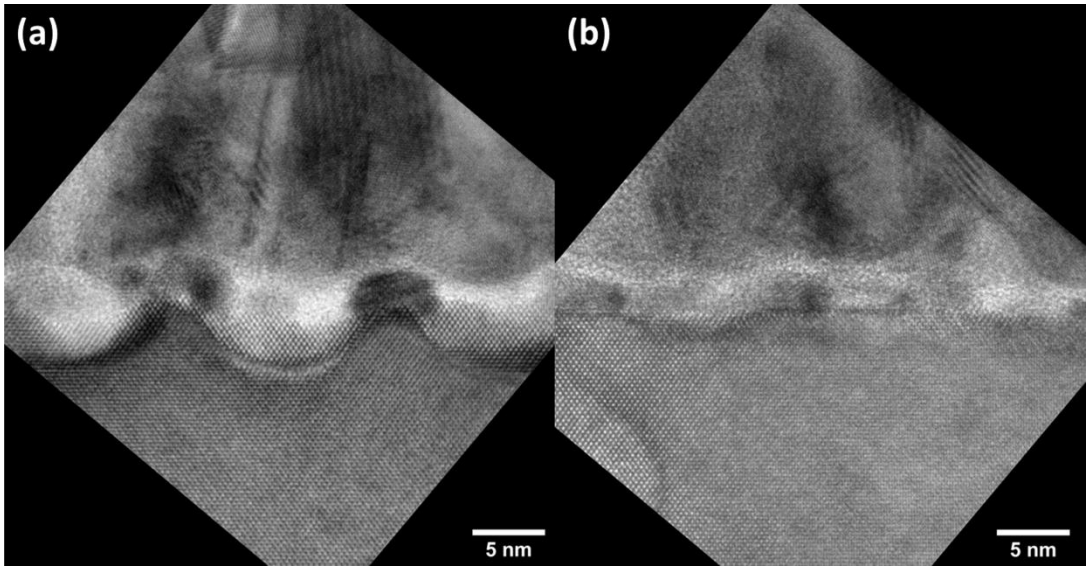

Figure 5.8. HRTEM of Ni/Ge interface pre-anneal in pillar **K**. There is a variation in the roughness of the Ge as well as the polycrystalline nature of the Ni seed.

5.4.2. Sample 2

Another sample, this time prepared using an SML resist, was annealed in situ in stages. The pillars fabricated do not possess the lip observed for the previous sample (prepared using PMMA-copolymer resist) and the diameters of the nanopillars are much smaller; **L** 50 nm; **M** 63 nm; **N** 45 nm. The in situ anneal of pillar **L** from sample 2 was performed in 3 steps; 200 °C for 60 min, 250 °C for 60 min and finally 300 °C for 60 min. Images from the in situ anneal are shown in Figure 5.9. For each anneal step the sample was heated directly to the selected temperature and maintained for 60 min. After each anneal, the sample was imaged in the double tilt stage holder to acquire HTREM images. Images of Pillar **L**, which was annealed in situ, are presented in Figure 5.10 after each anneal step.

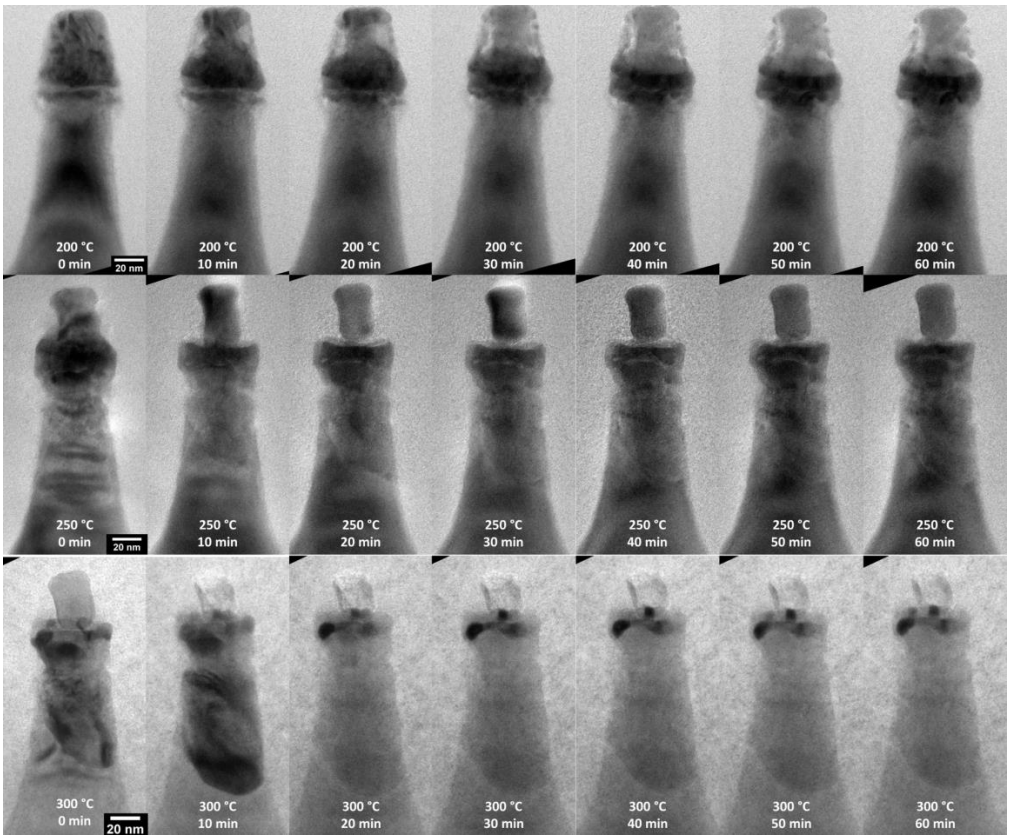

Figure 5.9. In situ anneal of pillar **L** from sample 2 at 200 °C for 60 min, 250 °C for 60 min and 300 °C for 60 min.

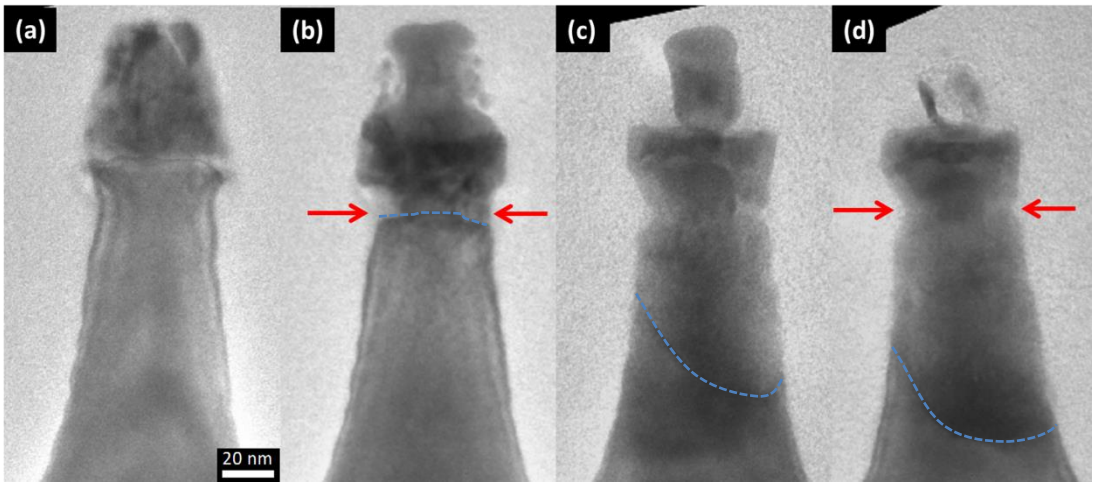

Figure 5.10. Pillar L (50nm diameter) from Sample 2 (a) before anneal, (b) after 200 °C anneal for 60 min, (c) after 250 °C anneal for 60 min and (d) after 300 °C anneal for 60 min. Red arrows show pinch due to Ge migration. Blue dashed line roughly shows Ge/germanide interface.

Migration of the Ge is observed in pillar **L** (Figure 5.9 and 5.10). A decrease in volume of the Ni seed is observed and progression of the germanide along the pillar. The germanide progression is difficult to distinguish from the in situ images alone so but a concave interfacial region can be identified particularly at the 300 °C anneal in Figure 5.9. The sample drifts in all directions (x, y and z) as it is heated and so it is challenging to maintain the same thickness contrast in the bright field imaging. There is a "pinch" (red arrows) after the 200 °C anneal as the Ge appears to have migrated and the germanide formation occurs in the centre of the nanopillar. HRTEM of the Ge/germanide interface of pillar **L** before and after the 200 °C anneal is presented in Figure 5.11. FFTs of the Ge and germanide regions are indexed in Figure 5.11 (d) and (e) taken from (c) and the germanide phase was found to be Ni_2Ge imaged along the $[0\bar{1}\bar{1}]$ zone axis. The epitaxial relationship is Ge[110]//Ni_2Ge$[0\bar{1}\bar{1}]$ and Ge$(1\bar{1}1)$//Ni_2Ge(100), assuming the strain observed in the Ge at the interface indicates the direction of germanide growth. The lattice mismatch between

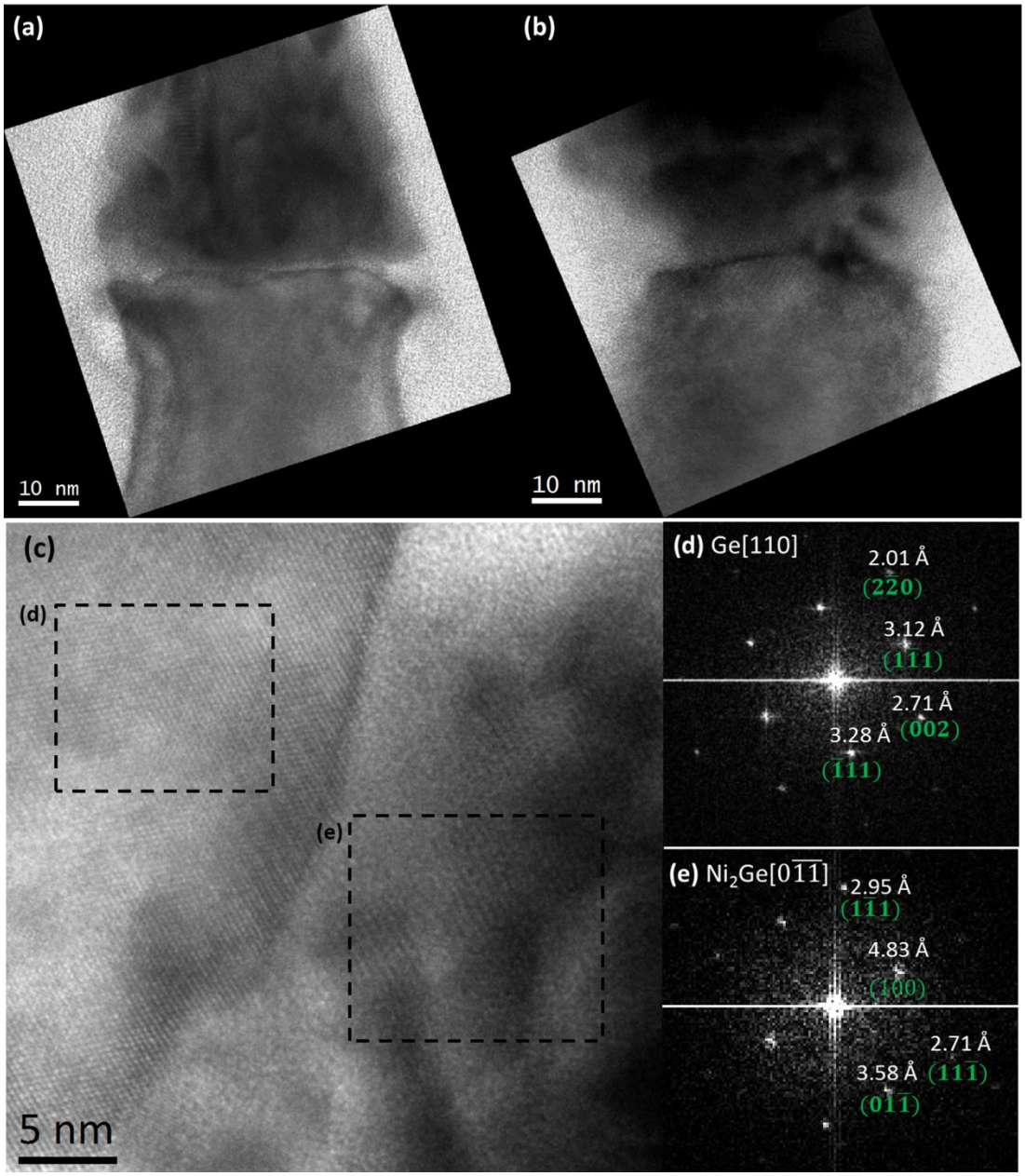

Figure 5.11. Sample 2 pillar **L** (a) before anneal and (b) after 60 min 200 °C anneal. (c) HRTEM of Ge/germanide interface after 60 min 200 °C anneal with FFTs (d) and (e) from the indication regions of (c).

Ge(1$\bar{1}$1) and Ni_2Ge(100) is 56.6%. The presence of defects shows the strain due to the lattice mismatch. An occurrence of the angled growth front is observed here for Pillar L (Figure 5.10 c and d), as observed previously by Tang et al.[31] Preferential germanide formation does not occur in the <001> direction. Instead the growth will

occur in a more favourable orientation which is at an angle to the long axis of the nanopillar, hence the observation of the angled growth fronts. These fronts are observed after the higher temperature anneals 250 °C and 300 °C.

Pillar **M** was not observed in situ but TEM images were acquired after each anneal step. Images acquired after each anneal step are presented in Figure 5.12. For the initial 200 °C anneal it appears that pillar M did not undergo any germanide formation or migration. However, comparing pillar M in Figure 5.12 before and after the 200 °C anneal, there are slight differences in the structure of the Ni seed and in the Ge at the edges near the Ni seed.

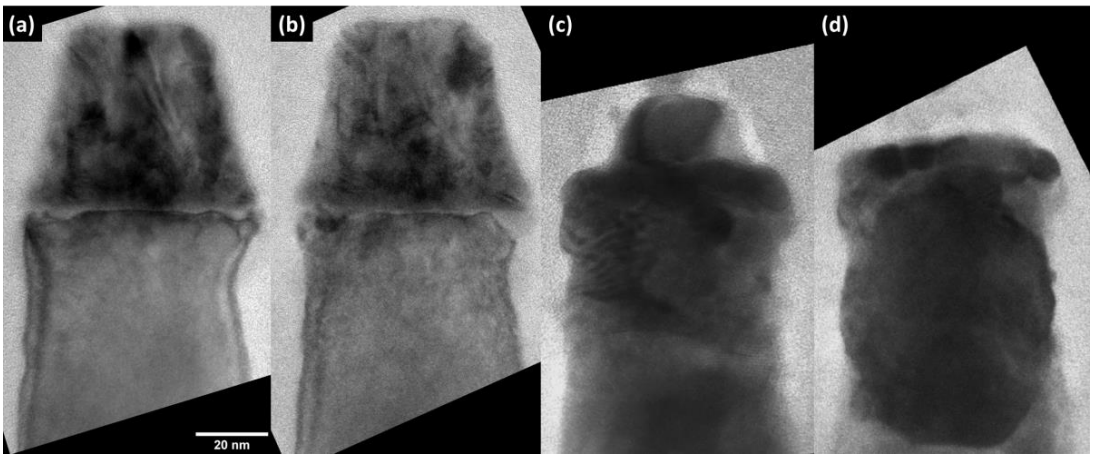

Figure 5.12. Pillar M (63nm diameter) from sample 2 (a) before anneal, (b) after 200 °C anneal for 60 min, (c) after 250 °C anneal for 60 min and (d) after 300 °C anneal for 60 min.

HRTEM of the affected Ge regions are shown in Figure 5.13 (a) and (c) before the anneal and (b) and (d) after the 200 °C anneal. Another observation from the post 200 °C anneal is the migration of Ge. There is a change in shape of the Ge as well as the presence of moiré/interference fringes in the post-anneal images for pillar M. There is a distinctive bump in the Ge at the Ni/Ge interface which helps as a

reference in Figure 5.13 (c). The same bump is present in (d) and the Ge region to the right of it is now amorphous.

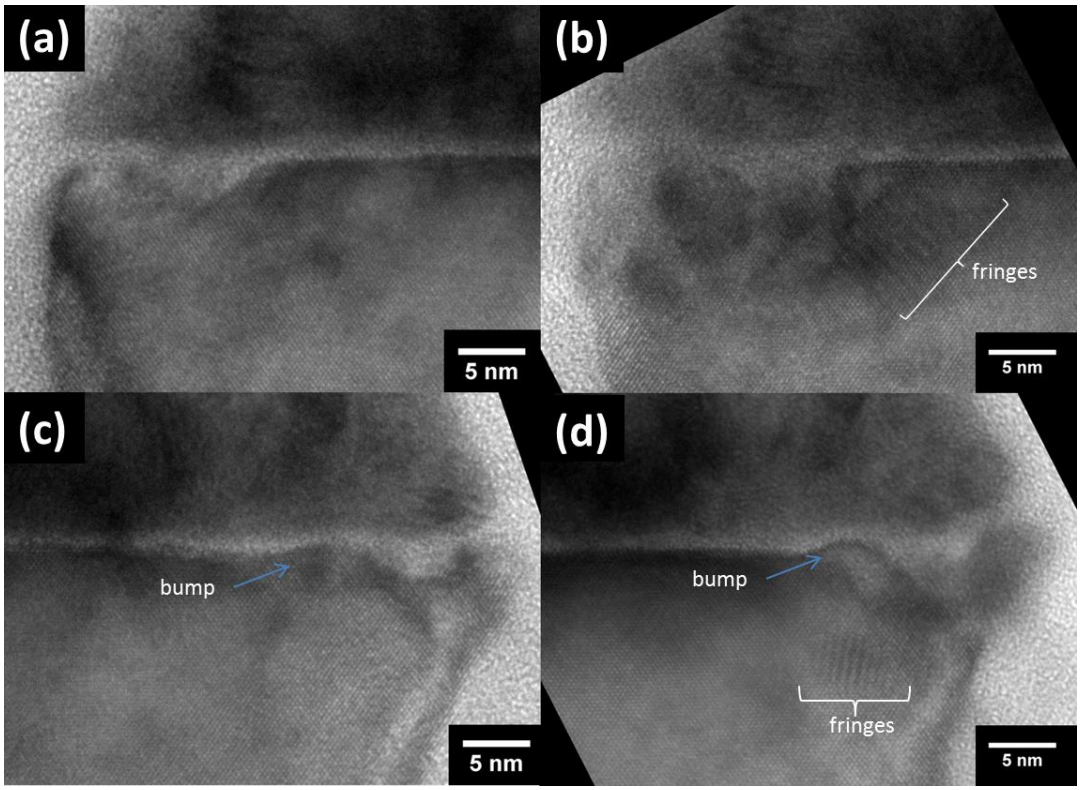

Figure 5.13. A closer look at the Ni/Ge interface of pillar M before (a and c) and after (b and d) the 60 min 200 °C anneal.

For the 250 and 300 °C anneals the migration of the Ni seed is notably observed in Figure 5.12 (c) and (d). After the final anneal the Ni seed has been consumed in the formation of the germanide. HRTEM and SAED of the germanide region in Figure 5.14 (b) and (d). The sample required tilting (approximately 4°) to orient the sample to image along the NiGe[101] zone axis relative to the Ge[110] zone axis. The epitaxial relationship is Ge[110]//NiGe[101] and Ge$(2\bar{2}0)$//NiGe$(11\bar{1})$. The lattice mismatch has been calculated to be 29.5%.

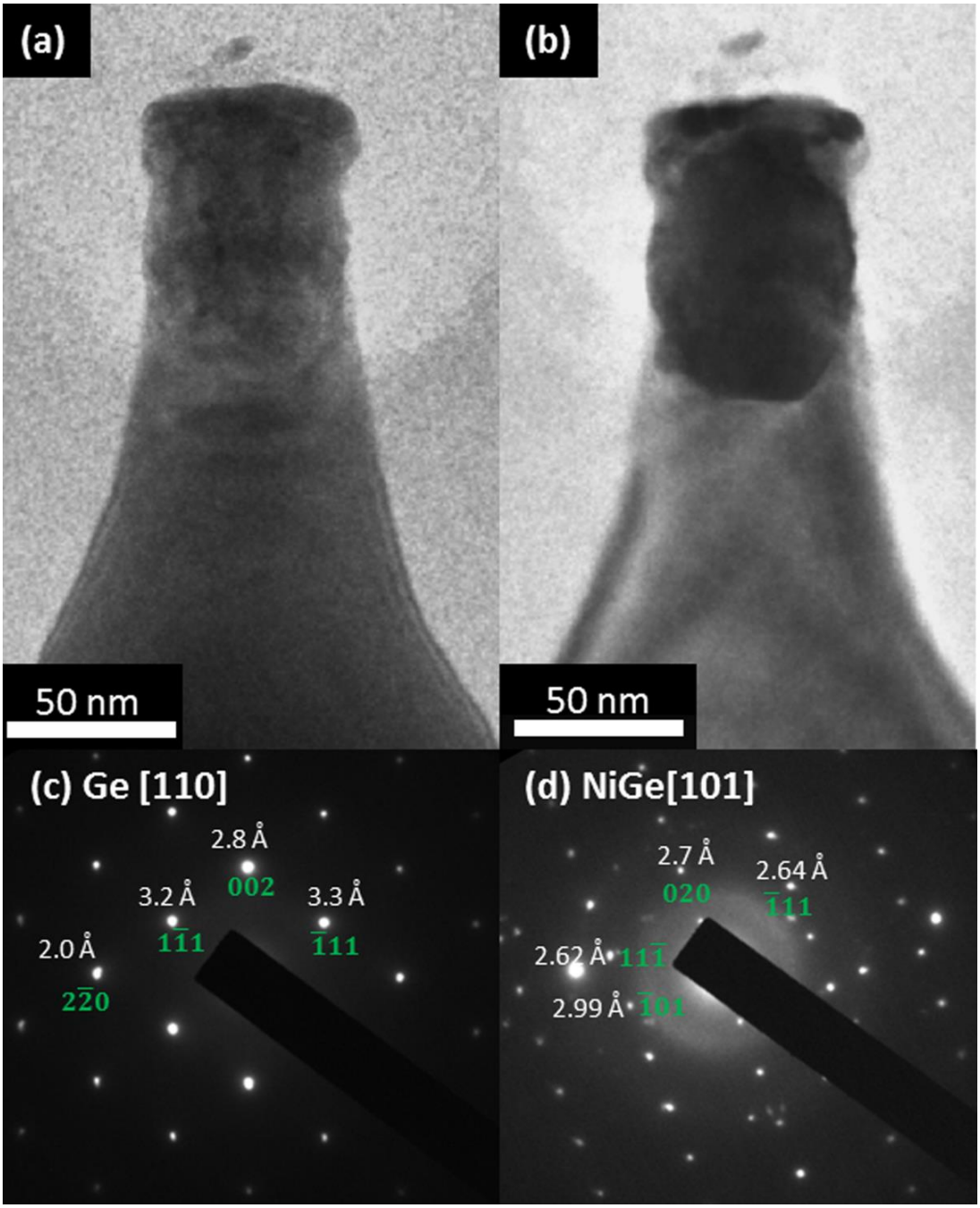

Figure 5.14. Pillar M from sample2 after final anneal at 300 °C for 60 min imaged at two orientations (a) along the Ge[110] zone axis and (b) along the NiGe[101] zone axis which is approximately 4° from the Ge[110] zone axis.

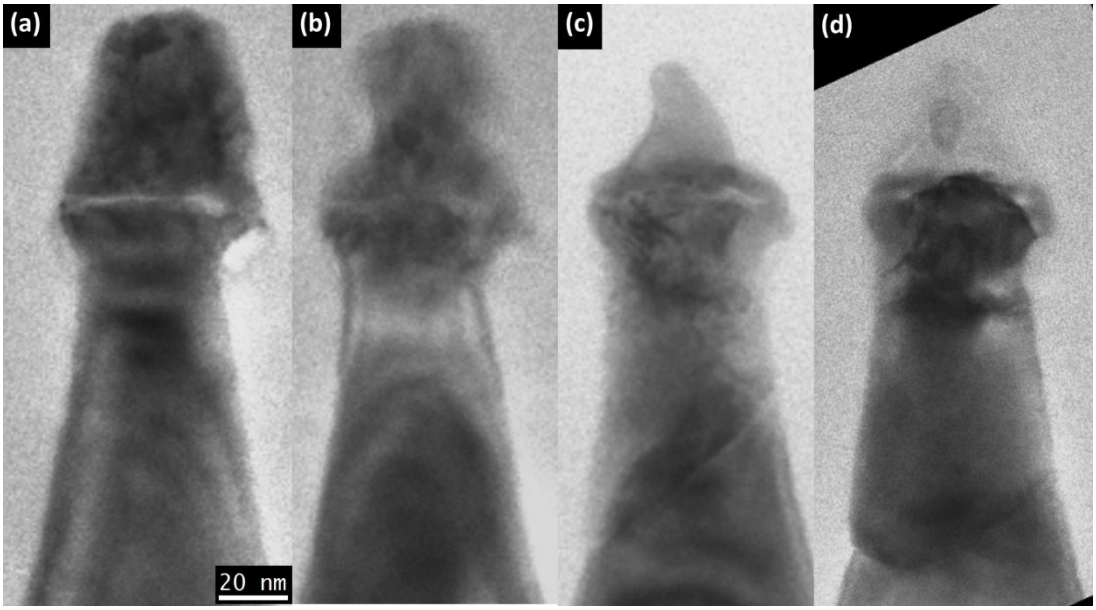

Figure 5.15. Pillar N (45nm diameter) from Sample 2 (a) before anneal, (b) after 200 °C anneal for 60 min, (c) after 250 °C anneal for 60 min and (d) after 300 °C anneal for 60 min.

A trend is observed after the 200 °C anneal whereby only the smaller diameter pillars, **L** (Figure 5.10) and **N** (Figure 5.15), appear to undergo Ni migration. Migration of Ge is observed for the smaller nanopillars where a "pinch" at the Ge/germanide interface is observed (Figure 5.10). The germanide formed in all three pillars (L, M and N) in this sample have an irregular shape with an angled interface.[31] This indicates that germanide formation in the Ge[001] direction is unfavourable.

An interesting observation in this sample is the apparent shrinking of the Ni seed as it migrates into the Ge pillar. There is no void formation as previously observed for all pillars in sample 1 (Figure 5.4). This is likely due to the microstructure of the Ni seeds in the pillars in sample 2 being closer to a single nanoparticle than a collection of nanoparticles as for the pillars in sample 1. The Ni seed in the pillars in sample 2 appears to essentially collapse.

5.4.3. HRTEM of Ni seeded Ge NW growth

As a comparison to help aid in the understanding of germanide formation, Ni-seeded grown Ge nanowires were studied. The nanowires were prepared by Dr Subhajit Biswas and the details of the growth are included in the appendix of this chapter. During the nanowires synthesis, the Ni seed reacted with Ge to form a Ni_3Ge seed, as was observed by Lu et al.[32] The formation of the desirable flat germanide/Ge interface is formed. The crystal relationship determined is Ge[101]//Ni_3Ge[110] and Ge$(24\bar{2})$//$Ni_3Ge(\bar{2}2\bar{4})$. There is a crystal mismatch between the Ge$(24\bar{2})$ and $Ni_3Ge(\bar{2}2\bar{4})$ (approx. 26%) and hence the formation of a $(11\bar{1})$ stacking fault (indicated in Figure 5.16 with red arrow).

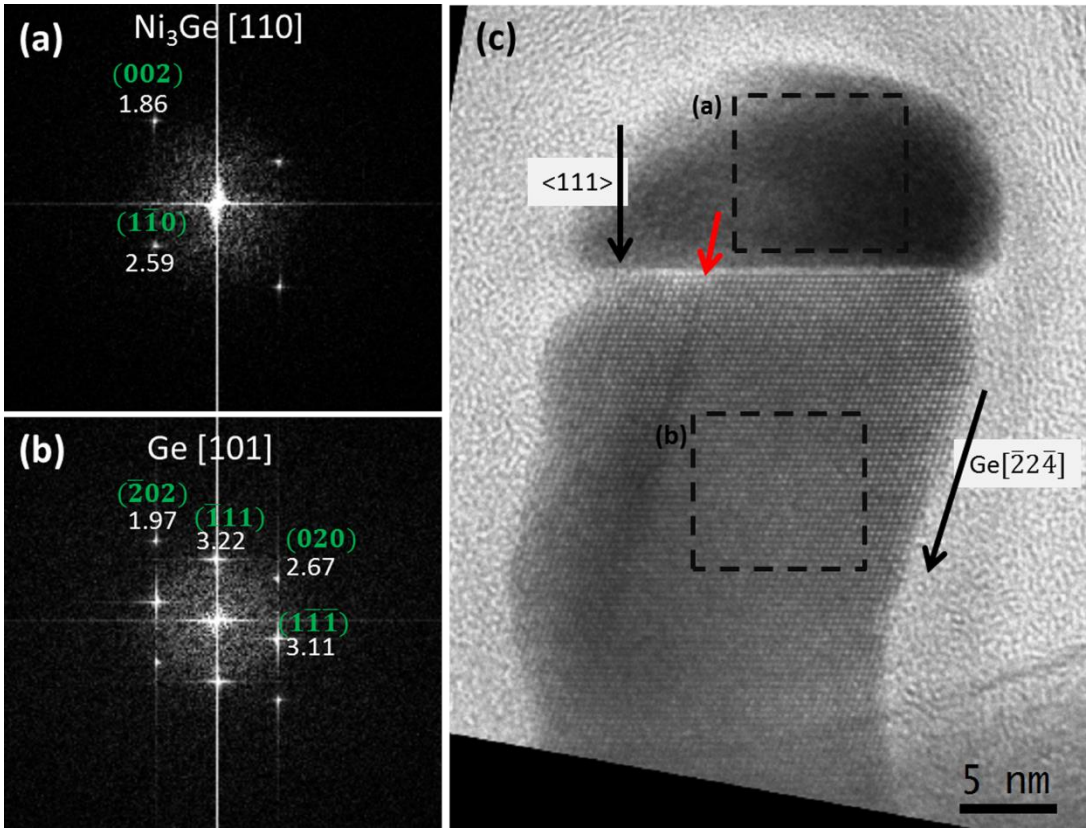

Figure 5.16. Ni-seeded grown Ge NW. (a) and (b) FFTs from regions indicated in (c). Red arrow identifies a $(11\bar{1})$ stacking fault. Black arrows show crystal directions.

Although the ideal atomically flat interface is achievable in grown Ge NWs using a Ni-seed, a less ideal germanide is formed and with the formation of even less desirable defects, rough surfaces and kinked nanowires.[32] Another kinked and defective nanowire from the same growth batch is presented in Figure 5.17.

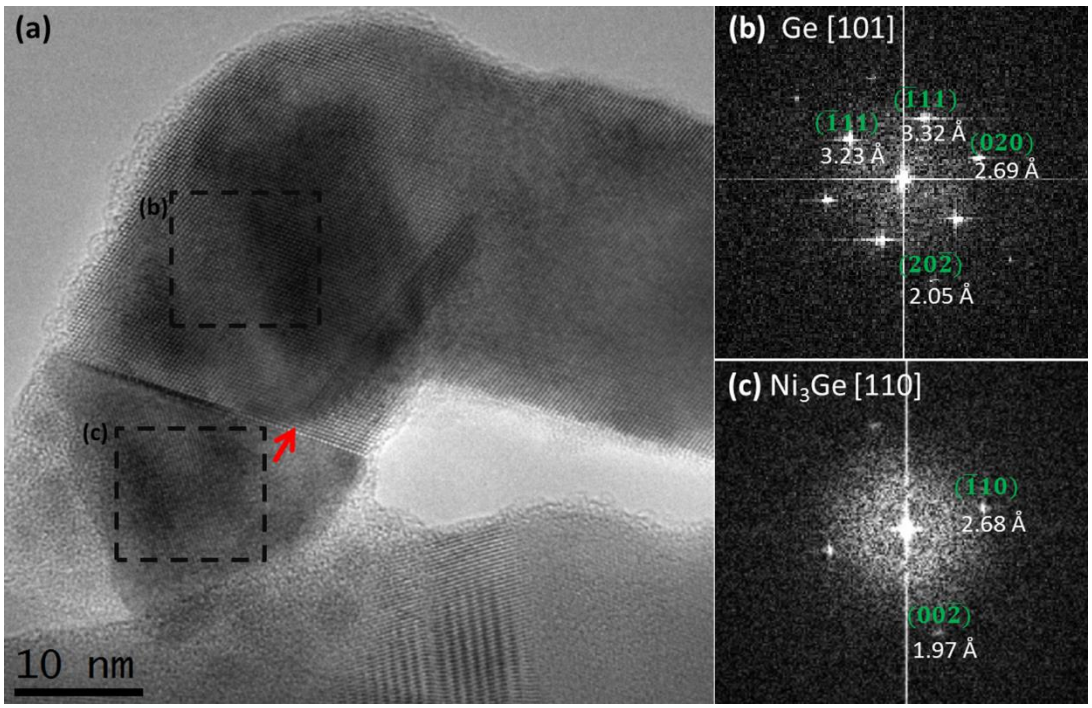

Figure 5.17. A second Ni-seed grown Ge NW. Red arrow indicates stacking fault.

For the nanowire in Figure 5.17, we again observe an atomically flat Ge/germanide interface. The formation of a Ni_3Ge seed is observed for this nanowire also. The occurrence of a stacking fault is again observed but at a site where the growth direction has changed dramatically (approx. 90°). The growth direction of the Ge NW at the interface with the seed is $[\bar{1}11]$ and after the kink the growth direction is $[24\bar{2}]$. Lu et al. observed [110] growth in their Ni-seeded Ge NW growth which varies from the [111] growth in our NWs.

5.5. Conclusions

In summary, a method to produce Ni-capped Ge nanopillars and examine germanide formation has been presented. These structures provide a route to accurately investigate the process and complex nature of germanide formation. A method to observe in situ heating has been presented but these structures could also be used to investigate the formation of germanide with the application of a current to the structure via the Ni seed/cap. This chapter has detailed experimental evidence to highlight the significant complexity for forming a NiGe phase with a near-atomically sharp interface over varying pillar diameters. There is variation in the Ni seed from pillar to pillar and it is this random polycrystalline Ni seed that results in a large variation in the germanide formed. As shown by Tang et al.,[31] a angled Ge/germanide interface is likely to form where the growth is directed in an unfavourable direction, as is observed here for Ge<001>. A dimensional dependence on reaction temperature is observed whereby the migration and germanide formation occurs for smaller diameter pillars at lower temperatures than larger pillars.

5.6. References

1 Liu, Y. Q., Ma, D. J. & Du, Y. Thermodynamic modeling of the germanium-nickel system. *J. Alloys Compd.* 491, 63-71, doi:10.1016/j.jallcom.2009.11.036 (2010).

2 Walser, R. M. & Bené, R. W. First phase nucleation in silicon–transition-metal planar interfaces. *Appl. Phys. Lett.* 28, 624-625, doi:10.1063/1.88590 (1976).

3 Wittmer, M., Nicolet, M. A. & Mayer, J. W. The first phase to nucleate in planar transition metal-germanium interfaces. *Thin Solid Films* 42, 51-59, doi:10.1016/0040-6090(77)90077-3 (1977).

4 Gaudet, S., Detavernier, C., Kellock, A. J., Desjardins, P. & Lavoie, C. Thin film reaction of transition metals with germanium. *J. Vac. Sci. Technol,. A* 24, 474-485, doi:10.1116/1.2191861 (2006).

5 Brunco, D. P., De Jaeger, B., Eneman, B., Mitard, J., Hellings, G., Satta, A., Terzieva, V., Souriau, L., Leys, F. E., Pourtois, G., Houssa, M., Winderickx, G., Vrancken, E., Sioncke, S., Opsomer, K., Nicholas, G., Caymax, M., Stesmans, A., Van Steenbergen, J., Mertens, P. W., Meuris, M., Heyns, M. M. Germanium MOSFET devices: Advances in materials understanding, process development, and electrical performance. *J. Electrochem. Soc.* 155, H552-H561, doi:10.1149/1.2919115 (2008).

6 Shayesteh, M., Huet, K., Toque-Tresonne, I., Negru, R., Daunt, C. L. M., Kelly, N., O'Connell, D., Yu, R., Djara, V., Carolan, P. B., Petkov, N., Duffy, R. Atomically Flat Low-Resistive Germanide Contacts Formed by Laser Thermal Anneal. *IEEE Trans. Electron Dev.* 60, 2178-2185, doi:10.1109/ted.2013.2263336 (2013).

7 Deng, Y., Nakatsuka, O., Suzuki, A., Sakashita, M. & Zaima, S. Epitaxial formation of Ni germanide on Ge(001) substrate by reactive deposition. *Solid-State Electron.*, doi:10.1016/j.sse.2015.01.009 (2015).

8 Liu, Q. B., Wang, G. L., Guo, Y. L., Ke, X. X., Radamson, H., Liu, H., Zhao, C., Luo, J. Effects of carbon pre-germanidation implant into Ge on the thermal stability of NiGe films. *Microelectron. Eng.* 133, 6-10, doi:10.1016/j.mee.2014.11.008 (2015).

9 Miyoshi, H., Ueno, T., Hirota, Y., Yamanaka, J., Arimoto, K., Nakagawa, K., Kaitsuka, T. Low nickel germanide contact resistances by carrier activation enhancement techniques for germanium CMOS application. *Jpn. J. Appl. Phys.* 53, 04EA05 doi:10.7567/JJAP.53.04EA05 (2014).

10 De Schutter, B., Devulder, W., Schrauwen, A., van Stiphout, K., Perkisas, T., Bals, S., Vantomme, A., Detavernier, C. Phase formation in intermixed Ni-Ge thin films: Influence of Ge content and low-temperature nucleation of hexagonal nickel germanides. *Microelectron. Eng.* 120, 168-173, doi:10.1016/j.mee.2013.09.004 (2014).

11 Chen, C. W., Tzeng, J. Y., Chung, C. T., Chien, H. P., Chien, C. H., Luo, G. L. High-Performance Germanium p- and n-MOSFETs With NiGe Source/Drain. *IEEE Trans. Electron Dev.* 61, 2656-2661, doi:10.1109/ted.2014.2327620 (2014).

12 Peter, A. P., Opsomer, K., Adelmann, C., Schaekers, M., Meersschaut, J., Richard, O., Vaesen, I., Moussa, A., Franquet, A., Zsolt, T., Van Elshocht, S. Ultrathin NiGe Films Prepared via Catalytic Solid-Vapor Reaction of Ni with GeH4. *ACS Appl. Mater. Interfaces* 5, 9605-9614, doi:10.1021/am4024719 (2013).

13 Lee, J.-W., Kwak, K.-H., Kim, H., Yang, C.-W., Lee, D., Ko, D.-H. In-situ annealing study on the thermal stability of nickel germanides. *J. Korean Phys. Soc.* 50, 677-680, doi: 10.3938/jkps.50.677 (2007).

14 Nemouchi, F., Mangelinck, D., Bergman, C., Clugnet, G., Gas, P., Labar, J. L. Simultaneous growth of Ni_5Ge_3 and NiGe by reaction of Ni film with Ge. *Appl. Phys. Lett.* 89, doi:10.1063/1.2358189 (2006).

15 Dellas, N. S., Minassian, S., Redwing, J. M. & Mohney, S. E. Formation of nickel germanide contacts to Ge nanowires. *Appl. Phys. Lett.* 97, doi:10.1063/1.3533808 (2010).

16 Tang, W., Nguyen, B. M., Chen, R. J. & Dayeh, S. A. Solid-state reaction of nickel silicide and germanide contacts to semiconductor nanochannels. *Semicond. Sci. Technol.* 29, doi:10.1088/0268-1242/29/5/054004 (2014).

17 Tsai, C. Y., Yu, S. Y., Hsin, C. L., Huang, C. W., Wang, C. W., Wu, W. W. Growth and properties of single-crystalline Ge nanowires and germanide/Ge nano-heterostructures. *CrystEngComm* 14, 53-58, doi:10.1039/c1ce06107k (2012).

18 Tang, J., Wang, C.-Y., Xiu, F., Lang, M., Chu, L.-W., Tsai, C.-J., Chueh, Y.-L., Chen, L.-J., Wang, K. L. Oxide-Confined Formation of Germanium Nanowire Heterostructures for High-Performance Transistors. *ACS Nano* 5, 6008-6015, doi:10.1021/nn2017777 (2011).

19 Nath, R., Soo, C. W., Boothroyd, C. B., Yeadon, M., Chi, D. Z., Sun, H. P., Chen, Y. B., Pan, X. Q., Foo, Y. L. NiGe on Ge(001) by reactive deposition epitaxy: An in situ ultrahigh-vacuum transmission-electron microscopy study. *Appl. Phys. Lett.* 86, doi:10.1063/1.1929100 (2005).

20 Comrie, C. M., Smeets, D., Pondo, K. J., van der Walt, C., Demeulemeester, J., Knaepen, W., Detavernier, C., Habanyama, A., Vantomme, A. Determination of the dominant diffusing species during nickel and palladium germanide formation. *Thin Solid Films* 526, 261-268, doi:10.1016/j.tsf.2012.10.113 (2012).

21 Nemouchi, F., Carron, V., Labar, J. L., Vandroux, L., Morand, Y., Morel, T., Barnes, J. P. Formation of NiGe through germanium oxide on Ge(001) substrate. *Microelectron. Eng.* 107, 178-183, doi:10.1016/j.mee.2012.12.010 (2013).

22 Tang, J., Wang, C.-Y., Xiu, F., Hong, A. J., Chen, S., Wang, M., Zeng, C., Yang, H.-J., Tuan, H.-Y., Tsai, C.-J., Chen, L. J., Wang, K. L. Single-crystalline $Ni_2Ge/Ge/Ni_2Ge$ nanowire heterostructure transistors. *Nanotechnology* 21, 505704, doi:10.1088/0957-4484/21/50/505704 (2010).

23 Gangnaik, A., Georgiev, Y. M., McCarthy, B., Petkov, N., Djara, V., Holmes, J. D. Characterisation of a novel electron beam lithography resist, SML and its comparison to PMMA and ZEP resists. *Microelectron. Eng.* 123, 126-130, doi:10.1016/j.mee.2014.06.013 (2014).

24 Ran, Y., Das, S., Hobbs, R., Georgiev, Y., Ferain, I., Razavi, P., Akhavan, N. D., Colinge, C. A., Colinge, J. Top-down process of Germanium nanowires using EBL exposure of Hydrogen Silsesquioxane resist. *J. Ultimate Integr. Silicon* 145-148, doi: 10.1109/ulis.2012.6193378 (2012).

25 Hobbs, R. G., Schmidt, M., Bolger, C. T., Georgiev, Y. M., Fleming, P., Morris, M. A., Petkov, N., Holmes, J. D., Xiu, F. X., Wang, K. L., Djara, V., Yu, R., Colinge, J. P. Resist-substrate interface tailoring for generating high-density arrays of Ge and Bi_2Se_3 nanowires by electron beam lithography. *J. Vac. Sci. Technol., B* 30, doi:10.1116/1.4724302 (2012).

26 Law, J. T., Meigs, P. S. Rates of oxidation of germanium. *J. Electrochem. Soc.* 104, 154-159, doi:10.1149/1.2428524 (1957).

27 Prabhakaran, K., Ogino, T. Oxidation of Ge(100) and Ge(111) surfaces: an UPS and XPS study. *Surf. Sci.* 325, 263-271, doi:10.1016/0039-6028(94)00746-2 (1995).

28 Deng, Y. S., Nakatsuka, O., Yokoi, J., Taoka, N. & Zaima, S. Epitaxial formation and electrical properties of Ni germanide/Ge(110) contacts. *Thin Solid Films* 557, 84-89, doi:10.1016/j.tsf.2013.10.017 (2014).

29 Lai, H.-Y., Huang, C.-W., Chiu, C.-H., Wang, C.-W., Chen, J.-Y., Huang, Y.-T., Lu, K.-C., Wu, W.-W. Real Time Observation of the Formation of Hollow Nanostructures through Solid State Reactions. *Anal. Chem.* 86, 4348-4353, doi:10.1021/ac500134u (2014).

30 Opsomer, K., Deduytsche, D., Detavernier, C., Van Meirhaeghe, R. L., Lauwers, A., Maex, K., Lavoie, C. Influence of Ge substrate crystallinity on Co germanide formation in solid-state reactions. *Appl. Phys. Lett.* 90, 031906-031906-031903, doi:10.1063/1.2431781 (2007).

31 Tang, J. S., Wang, C. Y., Xiu, F. X., Zhou, Y., Chen, L. J., Wang, K. L. Formation and Device Application of Ge Nanowire Heterostructures via Rapid Thermal Annealing. *Adv. Mater. Sci. Eng.*, doi:10.1155/2011/316513 (2011).

32 Lu, X. T., Harris, J. T., Villarreal, J. E., Chockla, A. M. & Korgel, B. A. Enhanced Nickel-Seeded Synthesis of Germanium Nanowires. *Chem. Mater.* 25, 2172-2177, doi:10.1021/cm401047w (2013).

5.7 Appendix

Ni seeded nanowire synthesis

The Ni seeded Ge NWs were grown by **Dr Subhajit Biswas**. Ge nanowires were grown in 5 cm^3 stainless steel cells (High Pressure Equipment Company) at temperature of 440 °C. The handling of dry toluene and diphenylgermane, as well as the filling of the reaction vessel and injection cell was carried out in a glove box under stringent precautions against water. In a typical experiment thin (20 Å) nickel film was sputtered on a Si(001) substrate and loaded in a stainless steel reaction cell. The reaction cell and injection equipment were dried under vacuum at 180 °C for 48 h and transferred in the glove box. 3 cm^3 toluene was filled in the 5 cm^3 reaction cell and the assembly was heated to desired temperature in a tube furnace for 2 h. After setting the pressure of the reaction cell to 21 MPa, the injection cell, filled with 20 ml of toluene/diphenylgermane solution (c = 4 μmol cm^{-3}), was set to the identical pressure by an ISCO HPLC pump. The precursor solution was injected at a rate of 0.025 ml min^{-1} over a time period of 120 min under constant pressure conditions in a flow through reaction. Finally, the reaction cell was cooled to room temperature, depressurized and disassembled to access the growth substrate. Nanowires were washed with dry toluene and dried under N_2 flow for further characterization.

Chapter 6

Conclusions and Outlook

A disturbance in the trend of Moore's law is becoming ever more inevitable as issues arise with Si processing.[1] The advantage of the stable SiO_2 is becoming obsolete due to gate leakage, opening the way for materials with better intrinsic electrical mobilities such as Ge, which had been previously overlooked due to issues with an unstable oxide.[2] If semiconductor NWs are to be incorporated into future electronic devices we need to fully understand, at the nanoscale, the implications of altering the structures to achieve the desired electrical properties.[3] The aim of this thesis was to explore some of the fundamental issues of Ge NW incorporation into future semiconductor devices. Typical fab processes have been applied, i.e. ion beam doping, crystal recovery post ion beam irradiation and germanide formation, to investigate the mechanism of the process and its effect on the NW.

Chapter 1 introduced the role of dynamic TEM for fundamental understanding of semiconductor nanostructures for future nanoelectronic devices. In situ TEM provides stepping stones to understand the fundamental properties of semiconductor nanowires. No stand-alone technique can provide all the answers but dynamic TEM can provide large pieces to the puzzle. With state of the art double aberration corrected TEMs with monochromators and equipped with analytical tools such as EELS and EDX coupled with in situ TEM holders, dynamic processes can be studied with potentially atomic resolution, particularly for 1-dimensional materials such as graphene.[4] This is a fascinating and broad area of research as shown by the diverse properties investigated in semiconductor nanowires discussed in the chapter.

Chapter 2 focused on the damage incurred in Ge NWs post ion irradiation. Nanowires suspended on FIB-labelled SiN membranes were irradiated in a stepwise

manner to monitor the damage build up with increasing ion flux. The results provided an understanding of the mechanism of the damage build up in NWs. A dependence on the shape and diameter of a NW and the ion energy used was established. It would be of interest to conduct these experiments under cryogenic and elevated temperature conditions. An increase in the damage is expected at the cryogenic temperatures as dynamic annealing would be eliminated at such low temperatures. The elevated temperatures would promote dynamic annealing however. As instruments are becoming more advanced and integrated, the potential to observe a single ion cascade event within a nanostructure at lattice or atomic resolution is becoming realistically achievable.[5] Operating conditions of the electron beam would need to considered as the beam could introduce energy which would promote dynamic annealing and produce false results. Nanostructures are ideal as they do not require any sample preparation techniques prior to TEM/irradiation and hence the samples are "pure" prior to irradiation.

Chapter 3 extended on methods and results described in chapter 2, with a focus on the thermal recovery of the crystal structure post ion irradiation. The main message to take from this chapter is that not only is a crystal seed required but also the external stresses on a NW determine the quality of the recovered crystallinity, i.e. polycrystalline or single crystalline and with the evolution of defects or not. Recrystallization within a NW is complex due to many competing factors including the competition between RNG and SPEG. SPEG is promoted when a crystal seed remains whereas RNG is promoted when the NW experiences strain. The high surface-area to volume ratio also increases the sensitivity of NWs to surface

roughness and stacking fault formation at the surface has been observed. To study structures produced via the top-down lithography approach; NWs could be defined on GeOI followed by a back etch through the bulk Si. The buried oxide would act as an etch stop and open a window for TEM imaging. This approach would provide NWs on a stable support which would facilitate ion irradiation followed by observation within the TEM without the need to extract the structures in a FIB cross section. The oxide would need to be thin enough to be electron transparent but thick enough to be a stable support for the Ge NWs, for example 100 nm.

Chapter 4 detailed an experimental set up for in situ observation of Ni-germanide formation in Ge nanopillars. The method facilitiates a range of Ge nanostructures with the same crystal orientation, here all substrates used were (001). An angled growth front was observed showing that germanide growth along the (001) orientation is not favourable.[6] Size dependence was observed for the temperature at which the Ni migration occurs at lower temperatures for smaller diameter structures. The variation in germanide formation from pillar to pillar and even within a pillar is attributed to the polycrystalline nature of the Ni seed. To investigate further the effect of the crystallinity of the Ni seed it is proposed that a single crystalline Ni seed should be used. One possible route would entail single crystalline (and ideally defect-free) Ni nanoparticles as the seed/etch mask for the nanopillar. One difficulty would be achieving a monolayer or sparsely dispersed Ni nanoparticles on a Ge substrate to achieve the individual nanopillars with clean etched sidewalls.[7,8]

Certain materials and/or mechanisms may be sensitive to the beam energy during in situ TEM experiments. These materials/mechanisms require ultrafast TEM techniques which allow fast acquisition and do not rely on a long exposure to achieve a high resolution image. Taking into account the effect the beam energy on a sample is vital as has been shown for Si nanostructures at high beam energies by Vanhellemont et al. (2MeV) and Fedina et al. (400keV).[8,9] To achieve high resolution images it should be a simple case of increasing the energy of the electron beam (in the MeV range) to decrease the wavelength of the electrons and in turn increase the special resolution. In the ideal world this should increase linearly, however, it was found that the wavelength of the electrons was not the only factor that limited the resolution of the TEM. In fact, aberrations in the lens, namely spherical (C_s) and chromatic (C_c) prevent ideal spatial resolution capabilities.[10] In modern commercial state-of-the-art (S)TEMs, the instrument operates within the low (<200 keV) and/or intermediate (200-400 keV) energy range and is equipped with double aberration correction and monochromators.[11] Single atom resolution has been demonstrated at beam energies as low as 60 keV.[12,13] With capabilities to achieve single atom resolution at such low energies opens the potential for dynamic TEM of beam sensitive materials/mechanisms.

The future of dynamic TEM is fast approaching with state-of-the-art TEMs capable of atomic resolution (for the one-dimensional materials such as graphene), ultrafast TEM capable of ns time resolution and stabilized in situ stage holders. The range of possible dynamic TEM experiments is phenomenal as more than one stimulus can be applied to a sample. A sample can be immersed in a condition similar to its actual

working conditions so as to observe a truer representation of processes and mechanisms. We have so far only observed the tip of the iceberg of the capabilities of dynamic TEM.

References

1 Kuhn, K. J. Moore's crystal ball: Device physics and technology past the 15 nm generation. *Microelectron. Eng.* 88, 1044-1049, doi:10.1016/j.mee.2011.03.163 (2011).

2 Brunco, D. P., De Jaeger, B., Eneman, G., Mitard, J., Hellings, G., Satta, A., Terzieva, V., Souriau, L., Leys, F. E., Pourtois, G., Houssa, M., Winderickx, G., Vrancken, E., Sioncke, S., Opsomer, K., Nicholas, G., Caymax, M., Stesmans, A., Van Steenbergen, J., Mertens, P. W., Meuris, M., Heyns, M. M. Germanium MOSFET devices: Advances in materials understanding, process development, and electrical performance. *J. Electrochem. Soc.* 155, H552-H561, doi:10.1149/1.2919115 (2008).

3 Lu, W., Xie, P. & Lieber, C. M. Nanowire Transistor Performance Limits and Applications. *IEEE Trans. Electron Dev.* 55, 2859-2876, doi:10.1109/ted.2008.2005158 (2008).

4 Pan, C. T., Hinks, J. A., Ramasse, Q. M., Greaves, G., Bangert, U., Donnelly, S. E., Haigh, S. J. In-situ observation and atomic resolution imaging of the ion irradiation induced amorphisation of graphene. *Sci. Rep.* 4, 6334, doi:10.1038/srep06334 (2014).

5 Hattar, K., Bufford, D. C. & Buller, D. L. Concurrent in situ ion irradiation transmission electron microscope. *Nucl. Instrum. Methods Phys Res., Sect. B* 338, 56-65, doi:10.1016/j.nimb.2014.08.002 (2014).

6 Tang, J. S., Wang, C. Y., Xiu, F. X., Zhou, Y., Chen, L. J., Wang, K. L. Formation and Device Application of Ge Nanowire Heterostructures via Rapid Thermal Annealing. *Adv. Mater. Sci. Eng*, doi:316513 10.1155/2011/316513 (2011).

7 Hogg, C. R., Picard, Y. N., Narasimhan, A., Bain, J. A. & Majetich, S. A. Pattern transfer with stabilized nanoparticle etch masks. *Nanotechnology* 24, doi:10.1088/0957-4484/24/8/085303 (2013).

8 Singh, J., Kaurav, N., Lalla, N. P. & Okram, G. S. Naturally self-assembled nickel nanolattice. *J. Mater. Chem. C* 2, 8918-8924, doi:10.1039/c4tc01360c (2014).

9. Vanhellemont, J., Anada, S., Nagase, T., Yasuda, H., Bender, H., Rooyackers, R., Vandooren, A. In situ UHVEM irradiation study of intrinsic point defect behavior in Si nanowire structures. *Phys. Stat. Solidi C,* doi:10.1002/pssc.201400100 (2015).
10. Fedina, L. I., Song, S. A., Chuvilin, A. L., Gutakovskii, A. K. & Latyshev, A. V. The mechanism of {113} defect formation in silicon: clustering of interstitial-vacancy pairs studied by in situ high-resolution electron microscope irradiation. *Microsc. Microanal.* 19, 38-42, doi:10.1017/s1431927613012294 (2013).
11. Mukai, M., Okunishi, E., Ashino, M., Omoto, K., Fukuda, T., Ikeda, A., Somehara, K., Kaneyama, T., Saitoh, T., Hirayama, T., Ikuhara, Y. Monochromator for aberration-corrected STEM. *Microscopy and Microanalysis* **20**, 606-607, doi: 10.1017/S1431927614004759 (2014).
12. Krivanek, O. L., Dellby, N., Murfitt, M. F., Chisholm, M. F., Pennycook, T. J., Suenaga, K., Nicolosi, V. Gentle STEM: ADF imaging and EELS at low primary energies. *Ultramicroscopy* **110**, 935-945, doi:10.1016/j.ultramic.2010.02.007 (2010).
13 Krivanek, O. L., Chisholm, M. F., Nicolosi, V., Pennycook, T. J., Corbin, G. J., Dellby, N., Murfitt, M. F., Own, C. S., Szilagyi, Z. S., Oxley, M., P., Pantelides, S. T., Pennycook, S. J. Atom-by-atom structural and chemical analysis by annular dark-field electron microscopy. *Nature* **464**, 571-574, doi:10.1038/nature08879 (2010).